Gravity Field Constraints on the Upper Mantle of Northwestern Europe

Root, Bart

Citation (APA)
Root, B. (2017). *Gravity Field Constraints on the Upper Mantle of Northwestern Europe*. [Dissertation (TU Delft), Delft University of Technology]. https://doi.org/10.4233/uuid:e4b25b64-544f-443e-80f3-a31f1f9e3964

Important note
To cite this publication, please use the final published version (if applicable).
Please check the document version above.

Gravity Field Constraints

on the Upper Mantle of Northwestern Europe

Ph.D. dissertation by: B.C. Root

TUDelft

Gravity Field Constraints

on the Upper Mantle of Northwestern Europe

Gravity Field Constraints
on the Upper Mantle of Northwestern Europe

Proefschrift

ter verkrijging van de graad van doctor
aan de Technische Universiteit Delft,
op gezag van de Rector Magnificus prof. ir. K.C.A.M. Luyben,
voorzitter van het College voor Promoties,
in het openbaar te verdedigen op

Maandag 25 september 2017 om 12:30 uur

door

Barend Cornelis ROOT

Ingenieur luchtvaart- en ruimtevaart,
Technische Universiteit Delft, Nederland,
geboren te Goes, Nederland

This dissertation has been approved by the:

promotor: prof. dr. L.L.A. Vermeersen

Composition of the doctoral committee:

Rector Magnificus,	voorzitter
prof. dr. L.L.A. Vermeersen,	promotor
dr. ir. W. van der Wal,	copromotor

Independent members:

Prof. dr. ing. habil. R. Klees,	Technische Universiteit Delft
Prof. dr. J. Ebbing,	Christian-Albrechts-Universität zu Kiel
Prof. dr. Z. Martinec,	Dublin Institute for Advanced Studies
Prof. dr. W. Spakman,	Universiteit Utrecht
dr. H. Steffen,	Lantmäteriet

Contents

Preface

When most people hear the word gravity they think about Newton and Einstein, 9.81 m/s^2 from their physics lessons in high school, Sandra Bullock in shorts, or even black holes. Gravity is a contant factor in our lives, for starters it makes objects fall down. Gravity has always captured my interrest. During my pre-graduate studies, I learned that when the basics of gravity were understood well enough, you are able to predict motions of objects, like a rock rolling down the mountain side, a cannon ball exiting the canon-nozzle, or even satellites orbiting the Earth.

A reporter once asked me; "But Bart, why do you study gravity? Newton and Einstein already explained everything?" This is a good question, Newton and Einstein, among others, basically set the scene for theoretical study in gravity. Here, there are certainly some questions to be solved, think of dark matter for example. So, what do I mean when I tell people I study gravity? This dissertation will not contain fundamental research on gravity, but instead I am using gravity observations to study our Earth, in particular the solid Earth. During the period of my PhD research I began to understand that gravity is a potential field, which varies significantly when measured at different locations. Studying these differences in the gravity field can reveal important information about the interior of our planet. These differences are so small that only dedicated instruments can observe them. I have given lectures about the gravity work of Vening Meinesz during his expeditions at sea, in which I always showed the following content on a slide:

- 9.8(1) - Mass of the Earth

- 9.80(1) - Shape of the Earth

- 9.80000(1) - Local mass variations

- 9.800000000(1) - Mass change in time

The slide is titled "The accuracy of the gravity measurement determines the amount of information about the Earth". Measuring gravity at different positions on the globe

provides information about certain physical characteristics of the Earth. Studying the gravity field with more accuracy will result in more detailed knowledge about those characteristics. More and more secrets of the solid Earth will be revealed, secrets that were not yet envisioned by Newton.

This famous Englishman once said: "I am standing on the shoulders of giants", which is of course true for every scientist. Nevertheless, in my case I was not only standing on the shoulders of giants during the period of my PhD research, but I was also carried by them: my advisors, fellow peers, colleagues, friends and family. We shared many moments where I learned from you.

First and foremost, I would like to thank Wouter. As my daily supervisor he has guided me through the whole process and showed me what a successful independent scientist should do. I am very grateful for this and I think I could not have wished a better supervisor than him. He has taught me to be critical and to acquire a broad perspective in my scientific subject. I still remember the trips back from conferences or workshops, where we would discuss the presented topics, general science, and other aspects until the flight or car trip had taken us to our destination. Not only was he my supervisor, but became a good friend and colleague.

It was a pleasure to see the process of creating a research group from very close (opposite my office). Bert, my promotor, became a professor of the chair of Planetary Exploration and due to the retirement of Prof. Ambrosius mid-way in my PhD, became my promotor. During this busy and interesting period for him, Bert still managed to have time for me and his door was always open for me to ask questions. I still have the geology books with beautiful drawings of George Escher that he let me borrow in my first year, which helped me understand the powerful attraction of the geo-science.

I was surrounded with incredible nice and interesting co-workers during my PhD, from whom I have learned so much. The group Astrodynamics and Space Missions in the faculty of Aerospace Engineering has become a second home to me because of them. Therefore, I would like to thank everybody in helping me during the period of my PhD research and all the time after that. Thank you Boudewijn, Relly (for the many talks we had), Ejo, Erwin, Ron, Marc, Pieter, José, Eelco, Joao, Wim, Daphne, Kevin, Bernhard, Imke, Leonid and all the new staff that came in the group during my PhD: Jeanette, Vidya, Francesco, Loic, Stephanie, and Elisabetta.

One co-worker in particular, I need to thank considerably: my 'office-mate' Dominic. I would like to thank him for maintaining the "political-incorrect free-zone" after his promotion to dr. Dirkx. It kept certain discussions very interesting. Dominic thank you for helping me keeping perspective in sometimes complicated issues. Our PhD periods were good times, where I have learned a lot from you, and hope to learn more in the years to come.

I could not have constructed the DopTrack ground station without the help of Joao. The station is now part of the curriculum of the faculty of Aerospace Engineering in the Bsc. and Msc. His knowledge on operational servers and equipment and his constant lectures and positive feedback rants on my programming skills are much appreciated. Currently, on the other side of the world, but still I can ask for help whenever is needed. Thank you.

I won't forget all the PhD candidates in our group with whom I had great discussions

and laughs, regularly at the "Space Bar". Thank you Hermes, Jinglang, Asrul, Kartik, Tatiana, Mao, Black, Bas, Haiyang, Teresa, Günther, Jacco, Svenja, Sowmini, Tim, Gourav, Yuxin and Sergei for hearing my sometimes strange theories on life, the universe, and everything else. Furthermore, I would like to thank my students for sticking around with me during their "tweedejaars project" or the Design Synthesis Exercise. And especially, my individual students, Bas (now also a PhD candidate), Robin, Martin, David, Anne, Oscar, Leon, and Marc, thank you for letting me be part of your project.

Even outside the comforts of the TUDelft I have met many interesting people. I met Jörg during my first ESA workshop in Enschede, who became a mentor and a good friend. Jörg worked at the time at NGU in beautiful Trondheim, Norway. Here, I also encountered Sofie with whom I had a great time discussing geophysics in a place were the Sun did not set. Later, Jörg moved to Kiel, were I was introduced to Nils and Wolfgang, a post-doc and PhD of the group with whom I still have interesting times. Both, Melanie and Jörg always made me feel well at home in their little mansion in "Revensdorf-Lindau", for which I am very grateful. The long conversations by the fireplace about Africa, Nirvana, and cooking will always be remembered by me. Furthermore, thank you for visiting me on my wedding all the way from Kiel.

In Enschede I also met Pavel and Josef, two incredible kind geodesists, who have always assisted me with my geodetical ventures and ideas. Furthermore, I would like to thank Zdenek for all his great talks and warm welcomes over the period of my PhD. And I won't forget all the other fascinating people I met during international conferences meetings, workshops, the ELITE PhD summer school, and other scientific gatherings. Coming from an engineering and space background, I knew nothing of basic geo-sciences. Two scientists in particular greatly helped me entering this world: Sierd Cloetingh and Rob Govers. With their course "Tectonophysics" at the University of Utrecht, they have quickly made me aware of this wonderful field of research.

A special acknowledgement goes out to the Vening Meinesz project team, Michiel, Joop, Simeon, Roos, Rene, Sander, and all others I met during this memorable period of research into the works of Vening Meinesz. It has brought me to places, like the inside of an submarine, the Dutch Archive in Delfzijl (which kind of looks like the archive in the ending of Indiana Jones: Raiders of the Lost Ark), the basement of the current headquarters of the FIOD (even meeting the director), the Depot and Treasury of TU Delft with all its wonders and many other archives, depots, and basements full of extraordinary equipment smelling of history. It allowed me to give presentations to many wonderful audiences, ranging from VMBO high-school students with incredible questions on satellite gravimetry to the members of the Hollandse Cirkel, who mentioned it was their first time not to fall a sleep during a one-hour lecture. I even got my 8 minutes of fame on a TV show called "Koffietijd", in which I talked about gravity followed by the perfect recipe for nice scones and the morning rituals of a Dutch soap-star. It has given me great pleasure to see that one of the results of the Vening Meinesz project is that a chapter dedicated to Vening Meinesz is placed in the "175 jarig Lustrum" booklet handed to the board of the university in 2017.

To all my friends that kept interested in my endeavours, I am grateful that you are in my life. Thank you, Arnout, Alex, Steef, Anne, Bobby, Renate and many more for being there and support me. Two of whom have helped me a great deal in writing this

dissertation, therefore Taco and Maurits I am very grateful for your assistance in getting my chaotic mind on paper. The many discussions we had on my research topic were insightful and kindly appreciated. I will always remember those coffee session (about research mixed with a jazz flavour) and hope to have more of them in the future.

I'd like to thank my family for having patience with me in this period and I hope I have made them proud. Thank you mom and dad, Tonca and Kjartan, but also my family-in-law Riek, Rozemarijn, Annemieke, Sjoerd and Saskia, and Marjan for listening to all my stories. On a sad note, during my PhD period I lost three members of my family. Three heroes who I am thankful for being in my life: Opa Root for his inspiration in the field of engineering, tante Liesbeth for her kindness to me and my wife, and my father-in-law Job for all the support and inspiration he was able to give me. I will miss you and remember all the fond memories I have of you.

Ultimately, the person that has been there the most is my beloved wife Karlijn. She has kept faith in me during the complete period of the PhD. She laughed with me in good times and talked me through the many "five-weekly PhD-blues". During all this, she even gave me the biggest gift I could receive: my beautiful son Beer. Thank you my love, for being there, it made this period that much more colourful.

<div align="right">

Delft, the Netherlands, June 2017
Bart Root

</div>

Summary

In the last decade, the gravity field of the Earth has been observed with increased coverage due to dedicated satellite missions, which resulted in higher resolution and more accurate global gravity field models than were previously available. These models make it possible to study large scale processes such as solid Earth deformation after large loading events such as retreat of ice sheets or to study lateral density variation in the lithospheric part of the upper mantle. However, to use the gravity data successfully, unwanted signal needs to be removed in order to extract the information of interest. For example, with lithosphere studies the gravity signal coming from the crust and the deep mantle needs to be removed. This is commonly done by filtering out long-wavelength signals from the solution to remove deep mantle effects, and by removing the crustal signal by forward modelling seismic-derived crustal models. With improved models of crustal structure and more accurate gravity data, new information about the upper mantle and lithosphere can be obtained. Adopting the increased resolution and accuracy of the global gravity field models, I have developed new approaches that focus on spectral analysis of the gravity field, which result in new insights of the upper mantle.

The forward gravity field modelling method that I improve upon in this dissertation is mostly used for topographic/isostatic mass reduction of gravity data (*Rapp*, 1982; *Rummel et al.*, 1988; *Pavlis and Rapp*, 1990). The methodology is able to transform density-models into gravitational potential fields using a spherical harmonic representation. I show that this methodology in the existing form is not suited to be used for density layers in lower crustal and upper mantle regions. The binomial series inherent to this methodology do not converge when applied to deep mass structures, and therefore it is not possible to truncate the series at a low degree to approximate the mass. This approximation is crucial for the computational efficiency of the methodology. I propose a correction that mitigates this erroneous behaviour, which enables this methodology to efficiently compute the potential field of deep situated masses. I benchmark the improved methodology with a tesseroid-based gravity-field modelling software, and I show that my software is accurate within ± 4 mGal, when modelling the Moho density inter-

face (with a range in signal of ± 500 mGal). The improved methodology is used in the studies described in this thesis.

With an efficient and accurate forward modelling methodology, I am able to use global gravity field data in studies of the solid Earth. In the central part of Fennoscandia the crust is currently uplifting, because of the delayed response of the viscous mantle to melting of the regional Late Pleistocene ice sheet. This process, called glacial isostatic adjustment (GIA), causes a negative anomaly in the present-day static gravity field as isostatic equilibrium has not been reached yet. Several studies have used this anomaly as a constraint on models of GIA (*Heiskanen and Vening Meinesz*, 1958; *Balling*, 1980; *Anderson*, 1984; *Marquart*, 1989; *Sjöberg et al.*, 1994), but the uncertainty in crustal and upper mantle structures had not been properly taken into account. In revisiting this problem, I show that the GIA gravity signal overlaps with mantle convection signals, such that a simple spherical harmonic truncation is not sufficient to separate these two phenomena. Furthermore, I find that, in contrast to the other studies, the effect of crustal anomalies on the gravity field cannot be effectively removed, because of the relative large uncertainties in the crustal density models. Therefore, I propose to correct the observed gravity field for GIA with numerical modelling results when constructing geophysical models that assume isostatic equilibrium. I show that correcting for GIA results in a significant vertical readjustment of the geometry of structural layers in the modelled crust of 5-10 percent. Correcting the gravity field for GIA prior to assuming isostatic equilibrium might be relevant in other areas with ongoing post-glacial rebound such as North America and the polar regions.

Uncertainty in lithospheric density models is still the limiting factors in solid Earth studies and needs to be improved. Lithospheric density anomalies can, among other methods, be estimated from seismic tomography, gravity studies, or joint studies using both datasets. I compare different gravity-based density models of the lithosphere to a tomographic-derived solution and characterise the sources that introduce large uncertainties in the density models of the lithosphere. To study the uncertainty between global and regional crustal models, I select a region where the crust is explored in great measure with seismic profiles, namely the British Isles and surrounding areas, where I use three crustal models to quantify the crustal uncertainty: CRUST1.0, EUCrust-07, and a high-resolution regional P-wave velocity model of the region. The crustal models contribute to the uncertainty of the density of the lithosphere with ± 110 kg/m^3. Furthermore, I study various P-wave velocity-to-density conversions to quantify the uncertainty introduced by these conversion methods (± 10 kg/m^3). All different crustal density models are forward modelled into gravity anomalies using the improved methodology of Chapter 2 and these gravity anomalies are subsequently removed from the gravity observations. The unmodelled long-wavelength signal in the gravity field representing mass anomalies in the deep mantle are removed from the observation by spherical harmonic truncation, introducing an uncertainty of ± 5 kg/m^3. Also, the choice of density background model (± 20 kg/m^3) and lithosphere-asthenosphere boundary uncertainty (± 30 kg/m^3) have a small but significant effect on the estimated lithosphere densities. However, the inhomogeneous spatial distribution of profiles of controlled-source seismic exploration of the crustal thickness and density distribution proves to be the largest source of uncertainty (± 110 kg/m^3). The gravity-based lithospheric density solutions with a variation of ± 100

kg/m^3 are completely different in magnitude and spatial signature to the densities (± 35 kg/m^3) derived from a shear wave velocity model (*Schaeffer and Lebedev*, 2013). This demonstrates that the tomographic model has a limited resolution, which can be related to regularisation that is used in the construction of global tomographic models. To account for this spectral imbalance, I spatially filter the gravity-based density models, resulting in similarities in spatial correlation and magnitude between that of the gravity-based and the tomographic-derived density. With the filtered gravity-based density I am able to estimate lateral varying conversion values between shear wave velocity and density for the lithosphere, which shows a correlation with major tectonic regions. This correlation shows that the independent gravity-based solutions, despite being filtered, can help in identifying different compositional domains in the lithosphere.

Satellite observations also provide global data on the temporal variations of the gravity field. In the last study, I show that global gravity-change observations from the GRACE satellite mission can be used to study GIA in the Barents Sea Region. The Barents Sea is subject to ongoing postglacial uplift since the melting of the Weichselian ice sheet that covered this region. The deglaciation history is not well known because there is only data from locations close to the boundary of the former ice sheet, in Franz Joseph Land, Svalbard, and Novaya Zemlya. At these locations the magnitude of the GIA uplift is limited, reducing the signal-to-noise of the data. The GRACE mission measures the gravity-change due to GIA at the center of the Barents Sea, where the maximum uplift and ongoing gravity-change is situated. I show that the linear trend in the gravity-change derived from a decade of observations from the GRACE satellite mission can constrain the volume of the ice sheet after correcting for current ice-melt, hydrology and far-field gravitational effects. Regional ice loading models based on new geologically-inferred ice margin chronologies (*Tarasov et al.*, 2012) show a significantly better fit to the GRACE data than the global ice models ICE-5G (*Peltier*, 2004) and ICE-6G_C (*Peltier et al.*, 2015; *Argus et al.*, 2014). The regional ice models in this study contain less ice mass during LGM in the Barents Sea than ICE-5G (5-6.3 m equivalent sea level vs. 8.5 m). Also, I show that the GRACE gravity-change is sensitive to the upper mantle viscosity underneath the Barents sea, for which I found a minimum value of 4×10^{20} Pas, regardless of the ice loading history. The GRACE gravity-change should be used as a constraint in any future GIA modelling of the Barents Sea, because it is the only measurement that captures the signal of maximum GIA.

The high resolution and accurate global gravity field models do give new insights in the structure and density distribution of the upper mantle. The presented studies in this dissertation demonstrate that analysing the spectral signature of gravity data is very useful. Medium-to-short-scale features, like lateral density variation in the lithosphere and GIA gravity-change in the Barents Sea can be separate from other gravity-change sources by applying spectral filters. For longer wavelength signals, such as the GIA static gravity signal in Fennoscandia, this proves to be more difficult due to the overlap in the long-wavelength region by mantle convection signals and other deep mantle signals. On the whole, the global gravity field models and their spectral signature play an important part in building a global density model of the Earth, in which lithosphere, GIA, but also mantle convection and core-mantle boundary effects need to be combined to explain the gravity field.

Samenvatting

Het zwaartekrachtsveld van de Aarde is door toegewijde satellite missies in het laatste decennium geobserveerd met een groeiende ruimtelijke dekking, wat resulteerde in hogere resolutie en nauwkeurigheid van de globale zwaartekrachtsmodellen dan voorheen aanwezig waren. Deze modellen maken het mogelijk om processen op grote schaal te bestuderen, processen zoals vaste Aarde deformatie na grote belastingevenementen door het terugtrekken van ijskappen, of om laterale dichtheidsverschillen in de lithosphere gedeelte van de bovenste mantel te bestuderen. Echter om de zwaartekracht data succesvol te gebruiken, moet ongewenst signal worden verwijderd zodat de gewenste informatie verkregen kan worden. Bijvoorbeeld, in studies over de lithosfeer moet het zwaartekrachtsignaal van de korst en diepere mantel worden verwijderd. Dit wordt meestal gedaan door de langgolvige signalen weg te filteren, zodat signalen van de diepe mantel worden verwijderd. Het korst signal wordt verwijderd door het voorwaarts modelleren van korst modellen uit seismische data. Met verbeterde korst modellen en hogere nauwkeurigheid in de zwaartekracht data is het mogelijk om nieuwe informatie over de lithosfeer en bovenste mantel te krijgen. Gebruikmakend van de verbeterde nauwkeurigheid en resolution in globale zwaartekracht modellen heb ik nieuwe benaderingen ontwikkeld die zich vooral richten op een spectrale analyse van het zwaartekrachtveld, wat resulteerde in nieuwe inzichten over de bovenste mantel.

De voorwaartse zwaartekracht modellering methode, welk ik in deze dissertatie heb verbeterd, is meestal gebruikt voor topografische en isostatische massa reducties van zwaartekracht data (*Rapp*, 1982; *Rummel et al.*, 1988; *Pavlis and Rapp*, 1990). De methode kan een dichtheidmodel transformeren in een zwaartekracht potentiaalveld gebruikmakend van een sferisch harmonisch representatie. Ik laat zien dat deze methode in zijn bestaande vorm niet geschikt was voor dichtheid lagen in de diepe korst een bovenste mantel. De binomiale reeks, inherent aan deze methode, convergeert niet naar een oplossing als deze wordt toegepast op diep-gelegen massa structuren en daarom kan de reeks niet worden afgekapt bij een lage graad voor de benadering van de massa. Deze benadering is beslissend voor de reken-efficiëntie van de methode. Ik stel een correctie

voor die het foutieve gedrag verlicht, hierdoor wordt de methode wel geschikt om de potentiaal van diep-gelegen massa's efficiënt te berekenen. Ik benchmark de verbeterde methode met een op tesseroids gebaseerde zwaartekracht modelleer software en ik laat zien dat mijn software tot op ± 4 mGal nauwkeurig is, wanneer een Moho dichtheid interface wordt gemodelleerd (dit signaal heeft een variatie van ± 500 mGal). De verbeterde methode wordt gebruikt in alle studies beschreven in deze dissertatie.

Met een efficiënt en nauwkeurige voorwaartse modelleer methode is het mogelijk om globale zwaartekracht data te gebruiken in vaste Aarde onderzoeken. Momenteel is de korst in het centrale gedeelte van Fennoscandia zich aan het verheffen, dit komt door de vertraagde reactie van de viskeuze mantel op het smelten van de regionale ijskap tijdens de late Pleistoceen. Dit process, genaamd glaciale isostatische aanpassing (GIA), is de oorzaak van een negatieve afwijking in het hedendaagse statische zwaartekracht veld, en is aanwezig omdat er nog geen isostatisch evenwicht is bereikt. Verschillende onderzoeken hebben deze afwijking gebruikt als voorwaarde in GIA modellering (*Heiskanen and Vening Meinesz*, 1958; *Balling*, 1980; *Anderson*, 1984; *Marquart*, 1989; *Sjöberg et al.*, 1994), maar met de onzekerheid in de kennis van korst en bovenste mantel structuren is niet naar behoren rekening mee gehouden. Bij het herzien van dit probleem laat ik zien dat het GIA zwaartekracht signaal overlapt met mantle convectie signalen, zodat een simpele afkapping van de sferische harmonisch reeks niet voldoende is om de twee effecten te scheiden. Bovendien merk ik op, in tegenstelling tot andere onderzoeken, dat het niet mogelijk is om effect van de korst afwijkingen op het zwaartekracht veld volledig the verwijderen, omdat de korst modellen nog relatief grote onzekerheden bevatten. Daarom stel ik voor om het waargenomen zwaartekracht veld te corrigeren voor GIA met numerieke modelleer resultaten wanneer geofysische modellen worden gemaakt met de aanname van isostatisch evenwicht. Ik laat zien dat het corrigeren voor GIA resulteert in een significante verticale aanpassing aan de geometrie van lagen in de korst van 5-10 procent. Het corrigeren van het zwaartekrachtveld voor GIA, wanneer isostatisch evenwicht wordt aangenomen, zou ook relevant kunnen zijn in andere gebieden met voortdurende post glaciale opheffing, gebieden zoals noord Amerika en de poolgebieden.

Onzekerheden in de dichtheid modellen van de lithosfeer is nog steeds de limiterende factor in vaste Aarde studies en moet dus verbeterd worden. Afwijkingen in de dichtheid van de lithosfeer kunnen onder andere worden bepaald door seismische tomografie, zwaartekracht onderzoek of een verenigd onderzoek gebruikmakend van beide methodes. Ik vergelijk verschillende zwaartekracht gebaseerde dichtheid modellen van de lithosfeer met een tomografisch afgeleid resultaat en kenmerk waar grote onzekerheden in de dichtheid oplossing worden geïntroduceerd. Om de verschillen tussen globale en regionale korst modellen te bestuderen selecteer ik een gebied waar de korst goed is onderzocht met seismische profielen, namelijk de Britse eilanden en omliggende gebieden, waar ik drie verschillende korst modellen gebruik om de korst onzekerheid te kwantificeren: CRUST1.0, EUCrust-07 en een regionaal P-golf snelheidsmodel met hoge resolutie. De verschillen in korst modellen dragen het meest bij aan de onzekerheid van dichtheden in de lithosfeer met ongeveer ± 110 kg/m^3. Verder heb ik de verschillende P-golf snelheid-tot-dichtheid omzetting bestudeerd om de onzekerheid door deze omzettingen te kwantificeren (± 10 kg/m^3). De verschillende dichtheid modellen van de korst zijn voorwaartse

gemodelleerd tot zwaartekracht afwijkingen met de verbeterde methode uit Hoofdstuk 2 en deze zwaartekracht afwijkingen zijn verwijderd van de zwaartekracht metingen. De ongemodelleerde lange golflengte signalen in het zwaartekracht veld welke de diepe mantel vertegenwoordigen zijn verwijderd door sferische harmonische serie afkapping, wat een onzekerheid van ± 5 kg/m^3 introduceert. Tevens hebben de keuze van achtergrond model voor de dichtheid (± 20 kg/m^3) en onzekerheid in de lithosfeer-asthenosfeer grens (± 30 kg/m^3) een klein maar significant effect op de geschatte lithosfeer dichtheid. Hiermee bewijst de niet-homogene ruimtelijke distributie van profielen in seismische exploratie van de korstdikte en de dichtheid distributie toch de grootste bron van onzekerheid (± 110 kg/m^3).

De lithosfeer dichtheid gebaseerd op zwaartekracht onderzoek hebben een variatie van ± 100 kg/m^3 en zijn totaal verschillend in grote en ruimtelijk uiterlijk als de dichtheid (± 35 kg/m^3) afgeleid van een S-golf snelheidsmodel (*Schaeffer and Lebedev*, 2013). Dit laat zien dat het het tomografisch model een beperkte resolutie heeft, wat kan toegeschreven worden aan de gebruikte regularisatie in het samenstellen van het globaal seismisch model. Om rekening te houden met deze spectrale onbalans heb ik de dichtheid modellen gebaseerd op zwaartekracht onderzoek gefilterd, zodat de grote en ruimtelijke uiterlijk van de geschatte dichtheden soortgelijk zijn met de tomografische resultaten. Met de gefilterde resultaten kan ik lateraal varirende conversie factoren schatten tussen het seismisch model en de dichtheid van de lithosfeer, deze factoren laten een correlatie zien met grote tectonische gebieden. Deze correlatie laat de mogelijkheid zien dat onafhankelijke zwaartekracht oplossingen van de lithosfeer dichtheid, ondanks dat ze gefilterd zijn, kunnen helpen in het identificeren van compositie in the lithosfeer.

Satelliet observaties bezorgen ook globale data van tijdsafhankelijke variaties in het zwaartekracht veld. In het laatste onderzoek (Hoofdstuk 5) laat ik zien dat globale zwaartekracht veranderingen, gemeten met de GRACE satelliet missie, kunnen worden gebruikt in het bestuderen van GIA in de Barents Zee. De Barents Zee ondervindt voortdurende post-glaciale opheffing sinds het smelten van de ijskappen die het gebied bedekte tijdens de Weichselian tijdperiod. De geschiedenis van smelt patroon is niet goed bekend, omdat er alleen data beschikbaar is op locaties dicht bij de grens van de voormalig ijskap, namelijk op Franz Joseph Land, Svalbard en Nova Zembla. De grote van het GIA signaal is beperkt op deze locaties, wat het signaal-tot-ruis verhouding verslechterd. De GRACE missie meet de zwaartekracht veranderingen door GIA in het midden van de Barents Zee, daar waar maximale opheffing en voortdurende massaverandering plaats vindt. Ik laat zien dat de lineaire trend in de zwaartekracht verandering, afgeleid van een decennium aan metingen door de GRACE satellieten, kan gebruikt worden om de onzekerheid in ijs volume te beperken nadat het signaal is gecorrigeerd voor het actueel smelten van ijs, hydrologisch signaal en far-field zwaartekracht effecten. Regionale ijs-belasting modellen die gebaseerd zijn op nieuwe geologische ijsmarge chronologien (*Tarasov et al.*, 2012) laten zien dat deze modellen de GRACE data significant beter kunnen beschrijven dan de globale modellen, zoals ICE-5G (*Peltier*, 2004) en ICE-6G_C (*Peltier et al.*, 2015; *Argus et al.*, 2014). The regionale ijs modellen in dit onderzoek bevatten minder ijs massa tijdens de periode met maximale ijshoogte in de Barents Zee dan ICE-5G (5-6.3 m "equivalent" zee niveau vs. 8.5 m). Ik laat ook zien dat de GRACE zwaartekracht veranderingen gevoelig zijn voor de viscositeit van

de bovenste mantel onder de Barents Zee, waar ik een minimale waarde van 4×10^{20} Pas voor vind, ongeacht het gekozen ijsbelasting model. De GRACE zwaartekracht verandering zou in elk toekomstig GIA onderzoek moeten worden gebruikt, omdat dit data is dat wel GIA observeert waar het maximaal is.

De globale zwaartekracht modellen met hoge resolutie en nauwkeurigheid hebben nieuwe inzichten gegeven in de structuur en dichtheid van de bovenste mantel. De onderzoeken die ik in deze dissertatie heb gepresenteerd laten zien dat het analyseren van de spectrale patroon van de zwaartekracht data zeer nuttig is. Middelgrote tot korte schaal structuren, zoals laterale variatie in lithosfeer dichtheid en GIA zwaartekracht verandering in de Barents Zee, kunnen worden gescheiden van andere zwaartekracht structuren door het toepassen van spectrale filters. Het scheiden van lange golflengte structuren, zoals het effect van GIA in het statisch zwaartekracht veld van Fennoscandia, blijkt moeilijker te zijn doordat er overlap is met mantel convectie en andere diepe mantel signalen. In het geheel spelen de globale zwaartekracht modellen en hun spectrale patronen een belangrijke rol in het opbouwen van een globaal model van de dichtheid van de Aarde, waarin lithosfeer, GIA, maar ook mantel convectie en kern-mantel grens effecten moeten worden gecombineerd, zodat het gehele zwaartekrachtveld kan worden beschreven.

Introduction

"I am not good at expressing these things, but I do wish to tell you that I am deeply grateful to you for giving me an insight into a field which is promising to be extremely interesting."

– Harry Hess, *In a letter to Vening Meinesz, (May 15, 1932)*

Before 1920, the Earth's gravity field was only measured in continental regions. This changed, because professor Vening Meinesz and his pendulum apparatus, made it possible to measure the gravity field with significant enough accuracy on the oceans (*Vening Meinesz*, 1932-1948). He and many others (*Worzel and Ewing*, 1950; *Shurbet and Worzei*, 1956; *Talwani*, 1962; *Vening Meinesz*, 1948-1958) complemented the observations done on the continents with offshore data. This made it possible to construct global gravity field models of the Earth. Unfortunately, due to areas which are difficult to access (Africa, Amazon Basin, Antarctica) and the vastness of the oceans, large regions were not measured. As a result solely the long-wavelengths of the gravity field could sufficiently be determined. Satellite data provide new gravity observations in areas where there is limited or no surface-based gravity observations such as South America, central Africa, the Himalaya region, and Antarctica (*Pail et al.*, 2011).

Since irregularities in the gravity field influence the orbit of a satellite, the global gravity field could be estimated by accurately observing the motion of the satellite (*Lundquist and Veis*, 1966). In the 1980s, only long-wavelength gravity fields could be estimated from satellite tracking data, but later satellite altimetry and improved surface gravimetry data were added to increase the resolution of global gravity field models (*Rapp et al.*, 1991). Over time the resolution and accuracy of the models improved and the data became attractive for different geophysical studies, like global dynamic to-

pography (*Forte et al.*, 1993), oceanography (Nerem et al., 1994), lithosphere modelling (*Turcotte and Schubert*, 1982) and geodesy (*Heiskanen and Moritz*, 1984).

The latest dedicated satellite gravity missions are the joint National Aeronautics and Space Administration (NASA) and the German Aerospace center's (DLR) GRACE twin-satellite mission (*Tapley et al.*, 2004) and European Space Agency's (ESA) GOCE gradiometer mission (*Drinkwater et al.*, 2003). One of the objectives of the GRACE mission was to obtain a map of Earth's global gravity field with a spatial resolution of 400 km. After only two years of data, the global error of an equipotential field, also called the geoid and commonly used to represent the variations in the gravity field, was already smaller than 2 cm (*Tapley et al.*, 2004), which is quite accurate compared to the variation of ± 100 m common for the geoid. The GOCE gravity mission obtained a similar accuracy of 1 cm geoid with a signal resolution of 100 km wavelengths. However, due to the design of the gradiometer onboard the GOCE satellite, the accuracy of the long wavelength signals is lower than the GRACE results (*Pail et al.*, 2011). Nevertheless, by combining both results it is possible to determine almost the entire gravity field of the Earth with similar accuracy at any location (*Pail et al.*, 2010).

Unfortunately, two particular regions of the Earth are not observed by satellite gravimetry. Satellite gravity observations experience a polar gap with a radius of 400 km, because the geometry of the orbit of the satellite is not perfectly situated over the poles (*Eshagh*, 2009; *Rudolph et al.*, 2002). The polar gap in Antarctica can be filled by aerial gravimetry (*Forsberg et al.*, 2011), whereas the Arctic region can be filled by airborne and submarine gravity data (*Tscherning et al.*, 2000; *Forsberg and Kenyon*, 2004). With these extra observations a complete model of the gravity field of the Earth can be constructed without the polar gabs innate to satellite-only observations.

With the introduction of satellite gravity data, more emphasis than before has been put on global gravity field models and their use in geophysical solid Earth studies. Currently, some of the common applied global gravity field models used in lithospheric studies are the following, starting with the EGM2008 model, which is complete up to a spatial resolution of 10 km (*Pavlis et al.*, 2012). The model contains mostly terrestrial data and altimetry data over the oceans, but also uses a GRACE-based gravity model (*Mayer-Gürr et al.*, 2010). Areas where no or limited data acquisition was available are complemented by a fill-in procedure. A high-resolution Digital Terrain Model (DTM) is used to forward model topographic masses into gravity anomalies. This procedure is common to bridge the gap between high and low spectral resolution of global gravity field models (*Fecher et al.*, 2015). This model is used frequently, for example in a lithospheric study on the lateral thickness and density variations under Norway and Sweden (*Gradmann et al.*, 2013). Furthermore, the EIGEN-6C model is one of the latest global gravity models, with a spatial resolution of 15 km, compiled from a combination of satellite (GOCE, GRACE, Lageos, and satellite altimetry missions) and terrestrial observations (*Shako et al.*, 2014). The model also contains gravity change measurements of seasonal variation and linear-trend in the gravity field with a spatial resolution of 400 km. This model, for example, was used in a study on the density structure of the crust and upper mantle of the North American lithosphere (*Kaban et al.*, 2014). Also, the GOCO05s model is used in this thesis, which is purely based on satellite gravity data and contains all the data from the GOCE mission with a spatial resolution of 70 km.

This particular model has a global accuracy of 1 mGal (1 Gal $= 10^{-2}$ m/s^2), in terms of gravity anomalies. The gravity model GOCO03s that is used in Chapter 3 is an earlier version of GOCO05s, but the differences between the models in my study area are negligible. Furthermore, GOCO05s was not yet available at the time that study was performed.
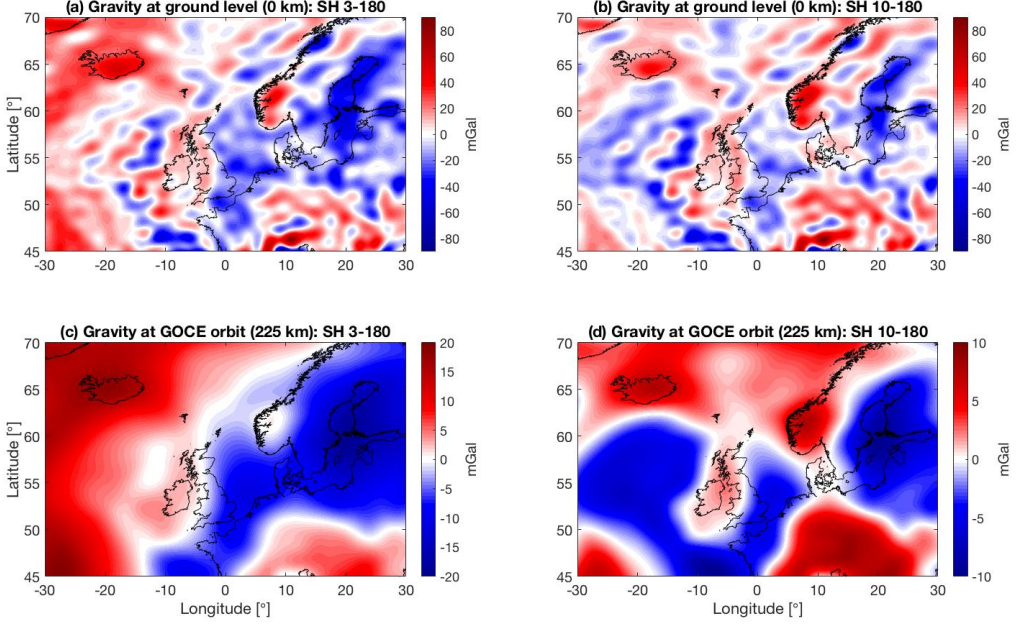
Figure 1.1: The gravity disturbances of a global gravity field model EIGEN-6C at different altitudes and different spherical harmonic truncations (SH): (a) SH 3-180 at ground level (0 km), (b) SH 10-180 at ground level (0 km), (c) SH3-180 at GOCE altitude (225 km), (d) SH 10-180 and at GOCE altitude (225 km).

The accuracy of a global gravity field model can be described for a certain resolution or spectral domain, linked to a maximum spherical harmonic degree and order. The gravitational potential field (V) of the Earth at a certain location (r, θ, λ) represented in spherical harmonics description is shown by the following expression (*Heiskanen and Moritz*, 1984):

$$V(r, \theta, \lambda) = \frac{GM}{R} \sum_{n=0}^{\infty} \sum_{m=0}^{n} \left(\frac{R}{r}\right)^{n+1} P_{nm}(\sin \theta) \Big(C_{nm} \cos(m\lambda) + S_{nm} \sin(m\lambda) \Big) \quad (1.1)$$

Here, the gravitational potential is expressed as a spherical harmonics expansion, where P_{nm} is the associated Legendre polynomial of degree n and order m. Furthermore, C_{nm} and S_{nm} are the spherical harmonics coefficients that describe the gravity field, influenced by the mass distribution of the Earth. The complete field is scaled with the parameters GM (standard gravitational parameter of the Earth) and R (the reference

radius). The spherical harmonic representation is an efficient way to describe the global gravitational field of Earth. Only the values for GM, R, C_{nm}, and S_{nm} need to be known to reproduce the gravitational potential at any point outside the encompassing sphere of the responsible masses. In theory, the summation in Eq. (1.1) goes to infinity, however in practice every global gravity field model has a maximum degree and order n_{max}. This truncation will limit the resolution of the computed gravity field due to the Nyquist criteria (*Sneeuw*, 1994). The spatial equiangular arc-deg resolution ($\Delta\lambda_{max}$) of the gravitational field is related to the maximum spherical harmonics coefficients (n_{max}) as follows (*Sneeuw*, 1994):

$$n_{max} = \frac{180°}{\Delta\lambda_{max}} - 1 \tag{1.2}$$

This means that a grid of 1x1 arc-deg is fully represented by spherical harmonic coefficients up to degree 179. The gravity field vector and gravity gradients can be computed by taking the first and second spatial derivative of the potential field, respectively. The term $\left(\frac{R}{r}\right)^{n+1}$ in Eq. (1.1) has a damping effect on the high degree spherical harmonic coefficients for increasing altitude, $r = R + h$. Even at low satellite altitude ($h = 250 - 800$ km), the high-degree gravitational signals are attenuated compared to the long-wavelength signals. This effect can be seen comparing Figure 1.1a and c. The natural filter limits the resolution of the observed gravity field by satellites. The spherical harmonics representation facilitates spectral analyses of the potential field. Figure 1.1a and c show the effect of removing the long-wavelength signal (spherical harmonics coefficients 3-9) from the observations. At ground level, this does not have a significant effect, because here it can be noticed that the high-wavelength signals dominate the observations. However, at satellite height the field changes considerably and structures that correlate with lithosphere structures appear in the observations. The ease to perform spectral analyses and bandpass filtering is a large benefit of global gravity field models, compared to small-scale datasets.

Both the static and time-varying global gravity field models are used in this dissertation to study the subsurface of the Earth, such as the upper mantle. The dissertation reports on new approaches of using global gravity field models to study the lithosphere and upper mantle. The global nature of the data set enables it to study global processes like lithosphere isostasy or Glacial Isostatic Adjustment (GIA). Static gravity observations are especially useful for estimating the lateral variation in density of the crust and upper mantle. However, proper handling of the observations to extract the signal that results from GIA or lithospheric density anomalies proves to be difficult. The new approaches that use global gravity fields are used to answer several research questions.

The following subsections discuss the background and motivation for the individual studies that make up the main material of this dissertation. The first section will discuss an improvement of a forward gravity modelling method that is capable of calculating gravitational potential fields of global mass structures like the crust and upper mantle. This is followed by two studies that use this methodology together with global gravity field models to study the effect of GIA and lateral density variations in the lithosphere on the static gravity field. The last study discusses the application of GRACE gravity change observations in a GIA study in an area where this data was not yet been used: the Barents Sea region. All studies contribute to new approaches in using global gravity

field models for geophysical research on the upper mantle.

I have focussed mainly on the northwestern part of Europe, because in that region the crust and lithosphere have been studied extensively by seismic observations (*Grad et al.*, 2009; *Tesauro et al.*, 2008). Therefore, this area can be used as a best-case-scenario of our knowledge of the subsurface. Also, Fennoscandia and the Barents Sea region experience ongoing uplift due to post-glacial rebound (*Lambeck*, 1995) and are therefore excellent regions for GIA-related studies. Nevertheless, due to the global nature of the presented models and methodologies, the modelling approaches can be applied to other areas as well.

1.1   Forward modelling of the gravity field

The large differences in the density structure of subsurface structures derived from seismic observations result in a large uncertainty of the modelled gravity field therefore many different model solutions need to be computed to capture this large parameter domain. Both in forward and inverse gravity-field studies, fast computations of high-resolution gravity fields are necessary. To connect global gravity field models to density models of the Earth, a reliable forward-gravity modelling methodology is needed.

Currently, there are two types of forward gravity-field modelling techniques commonly used (*Hirt and Kuhn*, 2014): spatial-domain forward modelling and spectral-domain forward modelling. The spatial-domain forward modelling method evaluates Newton's integral ((2.1)) directly, where an arbitrary mass object is approximated by elementary bodies, like prisms, tesseroid, or polyhedra (*Forsberg*, 1984; *Werner and Scheeres*, 1996; *Nagy et al.*, 2000; *Heck and Seitz*, 2007; *Kuhn et al.*, 2009; *Grombein et al.*, 2014; *D'Urso*, 2014). The summation of individual volume elements times their density is used to calculate a gravitational potential field. Any mass shape that can be approximated by the elementary bodies can be forward modelled into a gravitational potential. This technique is widely used, especially to model regional areas (*Forsberg*, 1984; *Kaban et al.*, 2010; *Holzrichter and Ebbing*, 2016). For global models, the computational time can become a complication, because higher resolution will increase the amount of numerical integrations rapidly (*Hirt and Kuhn*, 2014).

The spectral domain forward modelling evaluates the Newton mass integral much faster by transforming the masses into the spherical harmonic domain (*Lachapelle*, 1976; *Rapp*, 1982; *Rummel et al.*, 1988; *Pavlis and Rapp*, 1990; *Novák and Grafarend*, 2006). Two kinds of spectral forward modelling methodologies exist: the Rigorous Spectral Method (RSM) (*Lachapelle*, 1976) and the Fast Spectral Method (FSM) (*Rummel et al.*, 1988). The RSM is not practical for the resolution of current density and global gravity field models, so the FSM methodology was preferred for this study (see Chapter 2). This methodology has mostly been used for topographic/isostatic mass reductions of the Earth to compute isostatic anomalies (*Lachapelle*, 1976; *Rapp*, 1982; *Rummel et al.*, 1988; *Pavlis and Rapp*, 1990; *Novák and Grafarend*, 2006). With improving global density and gravity field models, the FSM would be a useful tool if it could model not only topography, but crustal and deeper situated mass layers as well. The question then arises whether the FSM is able to forward model deeper situated density structures, like crustal layers or lithospheric mass anomalies. The research question: *"Can spectral*

forward modelling be used to model upper mantle structure?" is studied in Chapter 2.

Another benefit of the spectral forward modelling is that it computes the spherical harmonic coefficients of the potential field, which enables spectral studies and simplifies bandpass filtering. With a spectral global forward-modelling methodology it is possible to compare the resulting gravity fields from multiple density distribution models in different spectral regimes. The FSM proves to be especially suitable for global gravity field modelling, because of its computational efficiency. However, concerns have been raised about the computational efficiency of extremely high-resolution density fields (*Hirt and Kuhn*, 2014), which is not an issue in this dissertation.

1.2   Gravity field expressions of Glacial Isostatic Adjustment

One interesting application of global gravity field models is the study of Glacial Isostatic Adjustment of the Earth. During glacial cycles enormous ice sheets with a thickness of up to 3-4 km partially covered the surface of the Earth (*Lambeck et al.*, 2000). The time of maximum ice extent in the last glacial cycle is called the Last Glacial Maximum (LGM), which was around 26.000 years ago (*Peltier and Fairbanks*, 2006). Areas that were partially covered with thick ice sheets, were northern America (Laurentia), Eurasia, Antarctica, and other smaller regions. During the LGM, these large ice masses caused the average sea level to be 120-130 meter lower than currently (*Peltier and Fairbanks*, 2006). Not only the sea surface changed, but also the surface of the solid Earth was affected by the redistribution of mass. The huge ice masses forced the Earth's crust downwards, pushing away the more viscous mantle material. The mantle rock flowed towards regions of lower pressure, resulting in a flow away from the centre of the ice sheet. Today, the reverse process is observed. The ongoing redistribution of mantle rock and ice mass is changing the gravity field of the Earth by several $\mu Gal/yr$ (*Tamisiea et al.*, 2007). This complex interaction of ice loading, the solid Earth, and the sea level is called Glacial Isostatic Adjustment (GIA) (*Farrell and Clark*, 1976). Because of the effect of GIA on the gravity field, global gravity field models can be useful in studying this process. In Chapter 3, I try to answer the following research question: "*Is it possible to observe and separate the GIA gravity effect from the static gravity field using improved crustal structures and isostatic models of the lithosphere?*" This would create an extra constraint for GIA models that could give insight in the viscosity structure of the mantle.

The process of relaxation of the solid Earth due to the redistribution of ice masses and sea level change is a large-scale process and therefore needs global modelling and global observations (*Lambeck*, 1990). To simulate the visco-elastic response of the Earth to the loading and unloading, many studies used the normal-mode method (*Amelung and Wolf*, 1994; *Vermeersen and Sabadini*, 1997; *Tromp and Mitrovica*, 1999; *Wu and Peltier*, 1982; *Sabadini et al.*, 1982; *Wolf*, 1984; *Peltier*, 1974; *Wu*, 1978; *Clark et al.*, 1978). The normal-mode method was developed by *Peltier* (1974) and *Wu* (1978) and simulates the physical response of the Earth for GIA studies. The method needs a radially-layered viscosity distribution of the Earth. Some of the models used many viscosity layers, like VM2 by *Peltier* (2004). Other Earth models model the viscosity

structure in the mantle with two layers, combined with an elastic lithosphere (*Paulson et al.*, 2007; *Peltier and Drummond*, 2008; *van der Wal et al.*, 2009; *Steffen and Wu*, 2011). I will be using a viscosity structure similar to the latter.

By constraining GIA models with observations the viscoelastic properties of the Earth can be studied (*Cathles*, 1975). The conventional observations in GIA studies are Relative Sea Level (RSL) curves, which indicate sea level at a certain time relative to the current sea level at that location (*Tushingham and Peltier*, 1992). So, RSL curves can look back in time, constraining the deglaciation evolution of historical ice sheets (*Lambeck*, 1990). These observations are for example stratigraphical records (e.g. lake cores), raised shorelines, brackish mud lines in lakes, but also archeological sites (*Steffen and Wu*, 2011). These geological observations are converted to RSL curves, which can then be compared against model predictions (e.g. *Tushingham and Peltier* (1992)). Figure 1.2 shows three distinct modelled RSL curves (red lines) and geologic observations
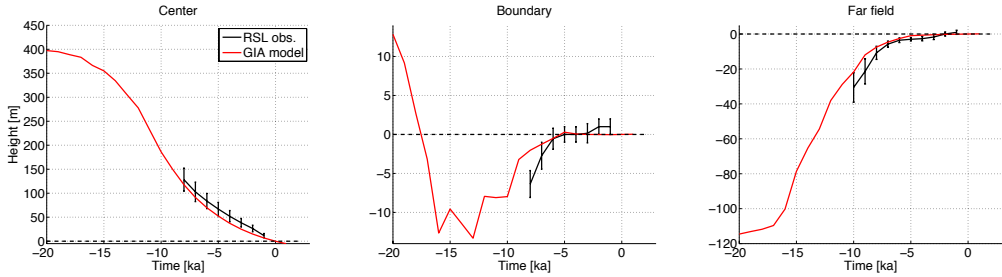
Figure 1.2: Three distinct Relative Sea Level (RSL) curves at three locations with respect to the Fennoscandian ice sheet (*Tushingham and Peltier*, 1992). At the maximum thickness of the ice sheet the largest change in sea level is observed. At the boundary of the ice sheet a complex variation of the RSL can be observed. Far away from the ice sheet, the crustal motions and self-gravitational effects on the sea level are small, which causes the change in sea level to approximate the average sea level change. The red lines are GIA model predictions (model 008-016 used in Chapter 3) and the black lines with error bars are geological observations of the relative sea level change.

(black lines with uncertainty bars). They characterise the change in sea level at three positions relative to the maximum depression of the surface at the center of the former ice dome. The modelled RSL curve shows a complex interaction between uplift and subsidence, which is seen at the boundary of the LGM ice-sheet extent. Between -20 and -15 ka, the uplift of the ground relative to the sea level is caused by melting of the ice sheet, which causes the Earth's surface to rebound. Later, the surface is subsiding relative to the sea level, because the solid Earth is almost in its equilibrium state, but the sea level is still rising due to ice melt at other locations. The observations at this location only capture the subsidence (black lines). At the far field, a rise of the sea level is detected, while the motion of the crust is negligibly small. Note especially the scale of the change in relative sea level height, ranging from 400 meter uplift in the centre to only a few meters of uplift/subsidence at the edge of the LGM ice sheet extent. The far-field experiences 120-130 meter of sea level rise. Far-field observations, at Barbados for example, can constrain the GIA modelling up to the time of LGM (*Peltier and Fairbanks*,

2006), because they are not affected by ice sheets, yet these geological records observe the effect of the summation of all ice sheets on Earth.

Geodetic observations of the current GIA change can also be used to constrain GIA (*Whitehouse*, 2009). These observations provide information about the ongoing surface uplift (GPS stations (*Lidberg et al.*, 2007)) or the corresponding mantle-mass displacement (GRACE gravimetry (*Steffen and Wu*, 2011)). Observations of the GPS uplift and gravity change in Fennoscandia are shown in Figure 3.2. The mantle mass transport towards former ice covered regions due to change in loading is clearly visible in the GRACE gravity observations (see Fig 1.3) as a positive secular gravity change. The use of GRACE gravity-rate observations has been successfully demonstrated in North America (*Tamisiea et al.*, 2007), where gravity observations are evidence of a double-domed ice-sheet. Also, the GRACE data is used to study GIA in Fennoscandia (*Steffen et al.*, 2008; *Steffen and Wu*, 2011) to better constrain the viscosity profile of the mantle.

The static gravity field shows remarkable correlation with areas of observed uplift linked to GIA in North America (*Mitrovica and Peltier*, 1989; *Wu and Peltier*, 1983; *Cathles*, 1975). However, the long-wavelength part of the gravity field, containing the GIA signal, is also affected by deep mantle mass anomalies (see Chapter 3). Underneath the North American lithosphere seismic velocity anomalies are observed, which could be related to convective downwelling that can explain a part of the negative gravity anomaly (*Simons and Hager*, 1997). *Tamisiea et al.* (2007) estimated the GIA signal of North America to be 25-45 percent of the observed -50 m geoid anomaly. Similar considerations need to be taken in Scandinavia. Early studies on the GIA in Fennoscandia have used the static gravity field to study the effect (*Haskell*, 1937; *Vening Meinesz*, 1937). Some contributed the negative gravity anomaly mainly to the mantle flow caused by the GIA uplift (*Heiskanen and Vening Meinesz*, 1958; *Sjöberg et al.*, 1994). Others attributed it mostly to crustal features or deeper density anomalies (*Anderson*, 1984; *Marquart*, 1989). However, those studies do not use sophisticated 3D models of the subsurface and thus fail to capture a more realistic effect to the observed gravity field. In Chapter 3, I examine the possibilities of using the static global gravity field models in a GIA study in Fennoscandia, by using more sophisticated 3D density models of the subsurface.

1.3   Exploring the lithosphere with global gravity field models

From Chapter 3, the biggest uncertainty in studying the upper mantle with global gravity field models will be shown to be modelling the crustal structures. In Chapter 4, I study the following research question: "*What are the different modelling uncertainties in estimating lithospheric density anomalies using global gravity field models?*" Global gravity field observations can be used to study the density distribution of the lithosphere. They are independent from seismic observations and have high accuracy compared to other exploration methods. However, the gravity field anomalies are a summation of all the mass anomaly sources in the subsurface and therefore other signals should be filtered out to observe the lithosphere signal.

It is to some extent possible to observe different depth domains of the subsurface by

appropriate spectral filtering of the gravity field. *Bowin* (1991) found that the spherical harmonic coefficients 4-10 were mainly responsible for mass anomalies below the lithosphere. *Kaban et al.* (2004) also found that the low-degree spherical harmonic coefficients have a high correlation to sub-lithosphere sources. Higher degree spherical harmonic coefficients correlate with topography and other shallow geological features (*Hirt and Kuhn*, 2014). So, by observing only a limited bandwidth of the gravity field spectrum, geological signals could be separated, which is why the spherical harmonic representation of the gravity field is helpful.

Global gravity field models played a major role in the formulation of the hypothesis of isopycnic state of the lithosphere. This hypothesis states that thermal effects are compensated by compositional effects resulting in similar density values underneath different tectonic regions (*Jordan*, 1978). Cratonic roots in the lithosphere contained similar density values as mantle material beneath other tectonic regions, which confirmed the isopycnic theory (*Jordan*, 1975). This meant that tomographic models that correlate with geology should not always correlate with the density structure in the upper mantle (*Doin et al.*, 1996). *Shapiro et al.* (1999) came to the same conclusions after studying the spherical harmonics coefficients 3-36: mainly that compositional buoyancy is needed to explain the observed thickness of the continental lithosphere. However, with improving global gravity field observations and models of the crust *Kaban et al.* (2003) questioned the isopycnic theorem and found that only 40 percent of the thermal effect was compensated by composition.

In their study, *Kaban et al.* (2003) used crustal stripping instead of spherical harmonic truncation to find the mantle gravity signal. The idea behind this method is to remove the gravitational signal of mass structures in the crust that are assumed to be known, such as topography, water bodies, sediments, and crystalline crust. The residual signal will then give information about the remaining un-modelled structures (*Kaban et al.*, 2004). With the introduction of global crustal models like 3SMAC (*Nataf and Ricard*, 1996) , CRUST5.0 (*Mooney et al.*, 1998), and its successors CRUST2.0 (*Bassin et al.*, 2000) and CRUST1.0 (*Laske et al.*, 2013), it became possible to compute a global crustal-gravity signal. These models are based on seismic observations and tectonic classification. They usually consist of an ice and water layer, a three-layered sedimentary structure, and a three-layered crystalline crust. The mis-modelling of sedimentary structures in gravity field studies has been shown to be a large source of uncertainty, because of the close proximity of these layers to the location of the observation (*Kaban and Mooney*, 2001). The classification of the upper, middle, and lower crust in the CRUST models is based on the selection of seismic velocity domains. The bottom of these models is usually defined by the Moho. *Bassin et al.* (2000) and *Tesauro et al.* (2014) provide values for the upper mantle density, just below the Moho boundary. Unfortunately, these global models still contain large uncertainties in their internal density structures to be able to determine a useful upper mantle density distribution (*Herceg et al.*, 2016).

Another strategy to study the crust and upper mantle is to combine gravity and seismic observations, such as done in the following regional studies for Europe (*Yegorova and Starostenko*, 1999; *Tesauro et al.*, 2008), southwestern Scandinavia (*Maupin et al.*, 2013), Finland (*Kozlovskaya et al.*, 2004), Eurasia (*Kaban*, 2001) and Siberian craton

(*Herceg et al.*, 2016). *Yegorova and Starostenko* (1999) used a seismic P-wave velocity (V_P) model of sedimentary and crustal structures and converted them into densities using empirically defined scaling relations. They found upper-mantle gravity-anomalies between -150 and 50 mGal, which were smaller than the residual mantle anomalies of $\pm$ 300 mGal in Eurasia found by *Kaban* (2001). EuCrust07 (*Tesauro et al.*, 2008) is a model for the crustal structure of Europe that combines seismic, thermal and gravitational data. The model produces residual mantle anomalies of $\pm$180 mGal in the mid-wavelengths of the gravity field. *Herceg et al.* (2016) studied the uncertainty introduced by the seismic-derived crustal models in gravity field modelling of the Siberian craton, where upper mantle anomalies of $\pm$300 mGal were found that corresponded to densities of up to $\pm$ 70 kg/m^3. Others concentrated more on improving the crustal structures, such as *Kozlovskaya et al.* (2004) who showed that a joint interpretation of a V_P model with gravity observations improves the density distribution estimates of the crust in southern and central Finland. By combining seismic models and gravity data, *Maupin et al.* (2013) showed a sudden change in crustal thickness between southern Norway and Sweden, that was previously not well understood. These regional examples illustrate that combining the gravity and seismic datasets have resulted in new insights about the crust and upper mantle, but that there are large variations in the gravity anomalies coming from the mantle. More subsurface studies are needed to construct accurate 3D density models of the crustal structure that combine gravity and seismic data to see if this is due to crustal errors or real mantle variations.

A useful theory to study the lithosphere is isostasy (*Lachenbruch and Morgan*, 1990). Isostasy was first theorised by J. H. Pratt (1809-1871), who envisioned that the Himalaya mountain range was supported in the crust by a lower density compared to the surrounding crustal structures (*Watts*, 2001). Other isostasy theories have been proposed, in which high topography is compensated by crustal roots (*Airy*, 1855) or mechanical forces (*Vening Meinesz*, 1932). Isostasy is seen as a successful theory to explain the observed gravity field of the Earth (*Kaban et al.*, 1999). However, seismic observations of crustal structure have shown that these simple isostatic models of the crust do not correspond to interpretations of seismic observations (*e.g.*, *Ebbing* (2007a)). For example, the Scandes Mountains in Sweden and Norway cannot be explained with a simple isostasy model. A more complex model of the subsurface was needed to explain the observed gravity field, introducing a low-density material between the Moho and Lithosphere Asthenosphere Boundary. This example suggests that not only the topography should be compensated, but that the complete crust is to be compensated. So, instead of using the classic isostasy models, more sophisticated isostatic models like lithosphere isostasy (*Lachenbruch and Morgan*, 1990) are to be used. These models introduce density anomalies in the lithosphere part of the mantle, responsible for the compensation of the crust (*Turcotte and Schubert*, 2014). This introduces lateral density variations in the lithosphere, which are corroborated by heat flow model results (*Sclater and Francheteau*, 1970; *Artemieva*, 2001), seismic observations, (*Foulger et al.*, 2013; *Afonso et al.*, 2016a), and geochemical theories (*Jordan*, 1975; *Cammarano et al.*, 2003). Topographic isostasy is not sufficient anymore to explain the subsurface of the Earth, which results in the need for more complex theories such as lithospheric isostasy.

In Chapter 4, I will explore the use of global gravity field data and lithosphere

isostasy to study the lithosphere of northwestern Europe. The study will be focused on the uncertainties introduced by filtering of the long-wavelength gravity signals, usage of seismic-derived crustal models, and different implementations of isostasy. The gravity model results will be compared with seismic tomography models of the lithosphere, to understand how to improve the combination of those results in finding a more robust model of the subsurface.

1.4 Glacial Isostatic Adjustment in the Barents Sea region observed by time-varying gravity

In the last presented paper (Chapter 5), I study new possibilities of using global measurements of the time-varying gravity from the GRACE mission to study the lithosphere and upper mantle. Previous studies had already shown the possibilities of using the GRACE gravity change data to constrain Earth rheology and historic ice loading models of Laurentia (*Tamisiea et al.*, 2007; *van der Wal et al.*, 2008), Fennoscandia (*Steffen et al.*, 2010), and Antarctica (*Riva et al.*, 2009). The research question of this chapter is: "*Is it possible to use the GRACE time-variable gravity data to constrain models of the past ice sheet in the Barents Sea region?*" The relatively small GIA time-varying gravity signal in the Barents Sea is close to the signal-to-noise of the data and is masked by the negative gravity change signal from local ice melt on Svalbard, Novaya Zemlya, and Frans Joseph Land.

An important benefit of satellite gravimetry is the ability to measure the complete gravity field of the Earth periodically (*Tapley et al.*, 2004). The GRACE mission has been making monthly observations of the gravity field for fourteen years. This makes it possible to observe mass change on and under the surface of our planet. The linear trend in the temporal gravity field is measured with increasing accuracy, because the GRACE satellite mission continues to observe Earth's gravity field. This extended observation-period improves the signal-to-noise ratio of the observations, which results in the possibility to observe smaller scale signals than before. Figure 1.3 shows the linear trend to the GRACE gravity change between 2003 and 2015. The linear trend in the GRACE data shows mass transport due to glacial melting, mantle flow due to readjustment of surface loading, and other mass transport sources. Areas in Alaska, Greenland, and Antarctica show a gravity decrease, which is linked to glacial melting (*Jacob et al.*, 2012; *Schrama et al.*, 2014). Moreover, we see a positive gravity change in Laurentia (Canada) and Fennoscandia (Norway, Sweden, and Finland), illustrating the mantle mass transport due to Glacial Isostatic Adjustment (GIA). GRACE gravity change observations have been successfully used for studying GIA in Laurentia (e.g. *Tamisiea et al.* (2007); *van der Wal et al.* (2008)) and Fennoscandia (*Steffen et al.*, 2010). For example, the GRACE gravity-rate maps settled a century-long debate on the geometry of the Laurentian ice sheets, showing that it consisted of two ice domes (*Tamisiea et al.*, 2007).

Grosswald (1980) and *Grosswald and Hughes* (2002) provided evidence for a glaciated Barents and Kara Sea, with even the Putorana Plateau south of the Taymir Peninsula heavily glaciated during the Late-Weichselian. This ice history model fits geological and
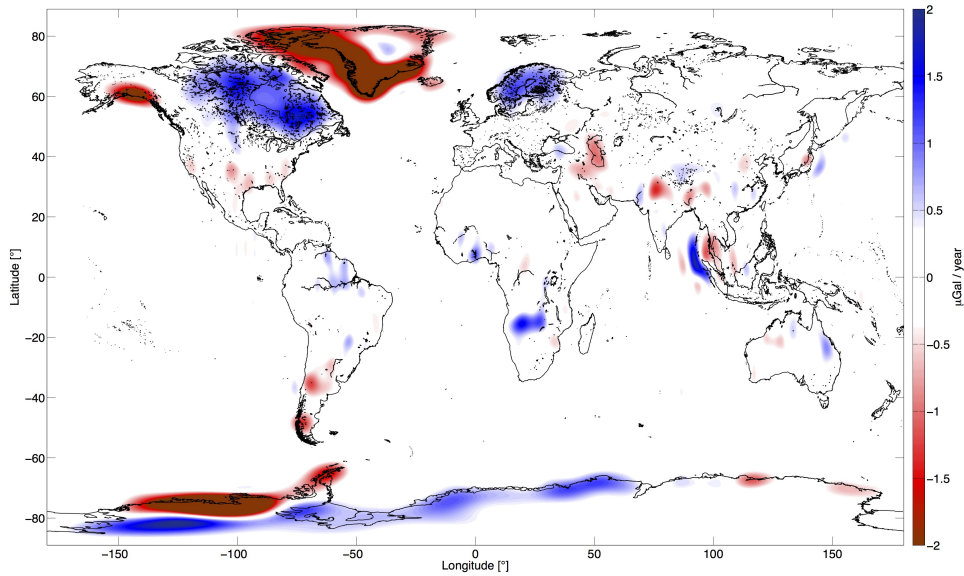
Figure 1.3: The linear gravity change observed by the GRACE satellite mission in the period between 2003 and 2015 using the CSR Release 5 monthly gravity fields (*Bettadpur*, 2003) using a Gaussian filter of 400 km halfwidth. The color scale is saturated at -2 μGal/yr to better illustrate the smaller signals.

paleo-hydrological evidence, paleo-climatological modelling, and global sea level changes (*Yokoyama et al.*, 2000). However, it is inconsistent with C-14 dating of bones and tree trunks on the Arctic continental shelf and coastal lowlands of Eurasia (*Astakhov*, 1998; *Larsen et al.*, 1999) which suggest a more limited ice history model in the Russian Arctic during the Late Weichselian (*Larsen et al.*, 1999; *Svendsen*, 1999) with no grounded ice on the northern shores of Russia. *Svendsen et al.* (2004a) based their historic ice sheet model on extensive stratigraphical and other geologic evidence. According to their model, the ice limit in the Kara Sea during the Last Glacial Maximum did not reach the shores of northern Russia, except a small part of the Taimyr Peninsula. Onshore moraines in the coastal areas of northern Russia were re-interpreted to belong to earlier glaciations, which implies that the Late Weichselian Kara Sea ice sheet had its border offshore of mainland Russia (*Mangerud et al.*, 1999). The ice sheet model of *Svendsen et al.* (2004a), which has less ice mass at LGM than that of *Grosswald and Hughes* (2002), is preferred by most field geologists and palaeontologists, but ice sheet thickness and timing and pattern of deglaciation are still uncertain. Furthermore, the location of the ice dome is unclear. The global ice loading model ICE-6G (*Peltier et al.*, 2015) places a single ice dome in the centre of the Barents Sea region. However, beach line studies around the northern coast of Novaya Zemlya could suggest a separate ice dome over the Russian island during later stages of the Late-Weichselian (*Zeeberg et al.*, 2000). Observations of GIA in this area could help resolve these issues. Unfortunately, GIA

in this region is poorly constrained by conventional observations such as RSL-curves and GPS uplift (*Svendsen et al.*, 2004b). The observations that try to capture the GIA effect are situated at the boundaries of the GIA signal (Svalbard, Novaya Zemlya, and Frans J. Land), where the magnitude of the signal is small. The maximum GIA effect in the Barents Sea is expected in the middle of the region, where no geologic or GPS observations are available (see Figure 1.4).
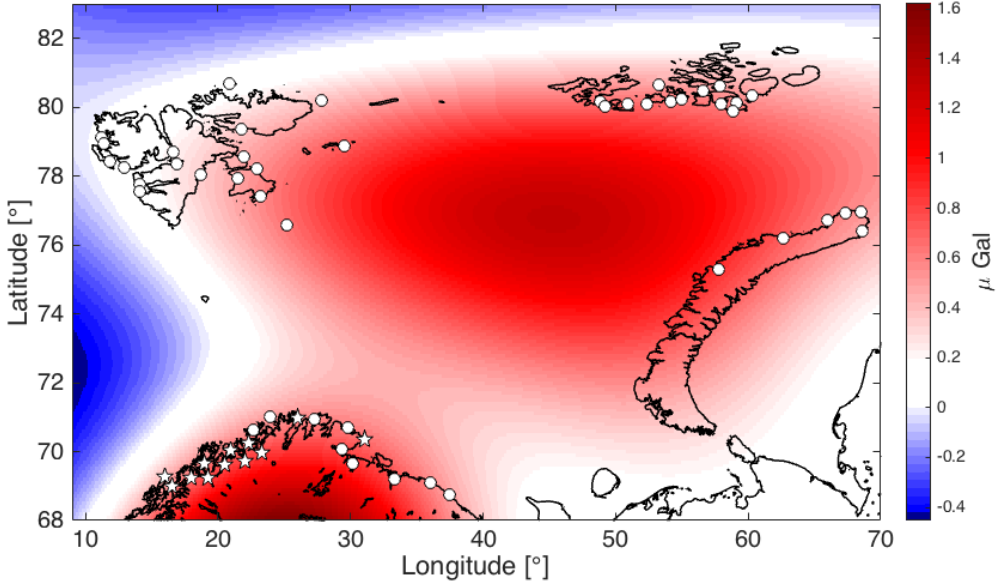
Figure 1.4: The Barents Sea region with the expected current gravity change due to GIA according to ICE-6G_C. The locations of RSL observations (white circles) and GPS stations (white stars) are situated at the boundaries of the expected uplift. Location of observations is a selection obtained from *Auriac et al.* (2016).

GRACE-derived gravity-rate data has the potential to resolve the large uncertainty in GIA models of the Barents Sea. However, this capability of the GRACE data was not yet been studied. In Chapter 5, I examine the possibility of using GRACE gravity-change observations in a GIA study of the Barents Sea. Furthermore, I study the sensitivity of the upper mantle viscosity and lithosphere thickness of the Barents Sea region.

Paper I - On a spectral forward modelling method

"In the sixties, both an American and a Russian scientist developed the spectral forward modelling methodology for modelling the gravity field of Phobos. Both did this independently from each other, because the Iron Curtain prohibited communication between them"

– Zdeněk Martinec during *ESA's first international GOCE Solid Earth Workshop in Enschede, (2012)*

On a spectral forward modelling method

B.C. Root[a], P. Novák[b], D. Dirkx[a], M.K. Kaban[c,e], W. van der Wal[a], L.L.A. Vermeersen[a,d]

Abstract This article reviews a spectral forward gravity field modelling method that was initially designed for topographic/isostatic mass reduction of gravity data. The method transforms 3D spherical density models into gravitational potential fields using a spherical harmonic representation. The binomial series approximation in the approach, which is crucial for its computational efficiency, is examined and an error analysis is performed. It is shown that, this method cannot be used for density layers in crustal and upper mantle regions, because it results in large errors in the modelled potential field. Here, a correction is proposed to mitigate this erroneous behaviour. The improved method is benchmarked with a tesseroid gravity field modelling method and is shown to be accurate within ±4 mGal for a layer representing the Moho density interface, which is below other errors in gravity field studies. After the proposed adjustment the method can be used for the global gravity modelling of the complete Earth's density structure.

keyword forward gravitational field modelling, spherical harmonic representation, global density models

1 Introduction

Interpreting gravitational data in terms of internal mass density distributions requires gravitational reduction that can be computed by forward modelling techniques. The gravitational field of any 3-D object can be computed by integrating the gravitational effects of its mass density distribution. One technique for evaluating this integral is based on spherical harmonic expansion of the Newtonian kernel. This technique was applied to forward modelling of the topographic potential and its gradients (*Lachapelle*, 1976; *Rapp*, 1982; *Rummel et al.*, 1988; *Pavlis and Rapp*, 1990) and modified for computing gravitational gradients generated by topography and atmosphere at satellite altitudes (*Novák and Grafarend*, 2006). The advantage of this technique is that it takes into account the curvature of the Earth.

There are two approaches to solve the spherical harmonic-based volume integral (*Pavlis and Rapp*, 1990): the rigorous formulation and the binomial series expansion method. The rigorous spectral method (RSM) introduced by *Lachapelle* (1976) is computational expensive (*Pavlis and Rapp*, 1990). The second approach, by *Rummel et al.* (1988), uses a binomial series expansion to approximate the volume. We call it the Fast

---

(a): Delft University of Technology, The Netherlands
(b): University of West Bohemia in Pilsen, Czech Republic
(c): GFZ in Potsdam, Germany
(d): NIOZ, Yerseke, the Netherlands
(e): Schmidt Institute of Physics of the Earth in Moscow, Russia

Spectral Method (FSM) in this study, because it is computationally more efficient than the rigorous spectral method. The number of computationally expensive global spherical harmonic analyses (GSHA) (*Sneeuw*, 1994) is drastically reduced by introducing the binomial series approximation. The FSM approach provides a means to use higher resolution density models than the RSM.

The FSM forward modelling is used in several previous studies (*Rummel et al.*, 1988; *Novák and Grafarend*, 2006; *Martinec*, 1991; *Root et al.*, 2015). Despite its computational speed, the FSM has limitations that should be known to users. The FSM forward modelling is used to compute the potential field of a topographic/isostatic mass layer in most studies, but for density layers in the lower crust and upper mantle the FSM gives erroneous results as will be shown in Section 4. This erroneous signal results in incorrect mantle density heterogeneities, when the FSM is used in a gravity inversion study. The improvement which is introduced here extends the applicability of the FSM to the general case of forward gravitational modelling of mass density distributions for an entire planet.

Section 2 provides a review of the analytical representation of the FSM. This is followed by a characterisation of the error introduced by the binomial series approximation. In Section 4, a mitigation strategy is introduced. Finally, a benchmark of the FSM with tesseroid software is shown in Section 5.

2   Review of the fast spectral forward modelling method

The analytical representation of the RSM and FSM starts similarly (*Pavlis and Rapp*, 1990). In the following, we derive a formula for the gravitational potential which is the conventional representation of a (conservative and irrotational) gravitational field. From Newton's law of universal gravitation and the superposition principle, the gravitational potential V outside the body Σ at location, P, can be computed (e.g.*Rummel et al.* (1988)):

$$V(P) = G \iiint_{\Sigma} \frac{\rho(Q)}{\ell(P,Q)} \, \mathrm{d}\Sigma(Q) \; . \tag{2.1}$$

where G is the universal gravitational constant, ρ is the mass density distribution within the body Σ and $\ell(P,Q)$ is the Euclidian distance between the computation point $P(r,\Omega)$ and the infinitesimal volume element $\mathrm{d}\Sigma(Q)$ at location $Q(r',\Omega')$. Eq. (2.1) can be rewritten by using (geocentric) spherical coordinates:

$$\mathrm{d}\Sigma = r^2 \mathrm{d}r \mathrm{d}\Omega. \tag{2.2}$$

Here, r is the radial coordinate and $\mathrm{d}\Omega = \sin(\theta)\mathrm{d}\theta\mathrm{d}\lambda$ is a surface element at a unit sphere, where ϕ and λ stand for a pair of geocentric angular coordinates and represents a geocentric direction. Eq. (2.1) then becomes

$$V(r,\Omega) = G \int_{\Xi} \int_{r'=r_{lower}(\Omega')}^{r_{upper}(\Omega')} \rho(r',\Omega') \, \mathcal{L}^{-1}(r,\Omega,r',\Omega') \, r'^2 \, \mathrm{d}r' \, \mathrm{d}\Omega' \; . \tag{2.3}$$

The kernel function $\mathcal{L}^{-1}(r, \Omega, r', \Omega') = \frac{1}{\ell(P,Q)}$ and the radial coordinate is given by r'. The radial limits of this integral represent the upper and lower boundaries of the mass density layer. The spherical harmonic representation for the inverse distance kernel is (*Heiskanen and Moritz*, 1984, p. 33):

$$\mathcal{L}^{-1}(r, \Omega, r', \Omega') = \frac{1}{r} \sum_{n,m}^{\infty} \left(\frac{r'}{r}\right)^n \frac{1}{2n+1} \; Y_{nm}(\Omega) \; Y_{nm}^*(\Omega') \; . \tag{2.4}$$

In this equation the abbreviated notation $\sum_{n,m}^{\infty} = \sum_{n=0}^{\infty} \sum_{m=-n}^{n}$ is used. Eq. (2.4) can be substituted in Eq. (2.3):

$$V(r, \Omega) = G \sum_{n,m}^{\infty} \left(\frac{1}{r}\right)^{n+1} \frac{1}{2n+1} \; Y_{nm}(\Omega) \int_{\Xi} \rho(\Omega') \, Y_{nm}^*(\Omega') \, \mathrm{d}\Omega' \int_{r_{lower}(\Omega')}^{r_{upper}(\Omega')} r'^{n+2} \mathrm{d}r' \; . \tag{2.5}$$

where it is assumed that the density distribution within the layer does not depend on the radial position. In the Appendix an approach for a radially varying density distribution in the mass layer is discussed. For both cases, the radial integral in Eq. (2.5) must be evaluated. The radial limits of this integral can be defined as follows:

$$r_{upper}(\Omega') = R + U(\Omega') \; , \tag{2.6a}$$

$$r_{lower}(\Omega') = R + L(\Omega') \; . \tag{2.6b}$$

$U(\Omega')$ and $L(\Omega')$ are upper and lower deviations from the circumscribing sphere (R) of the volumetric mass layer that is forward modelled (see Figure 2.1). This means that $R \geq R + U \geq R + L$, or in other words $0 \geq U \geq L$. Integrating the radial integral of Eq. (2.5) then yields

$$\int_{r_{lower}(\Omega')}^{r_{upper}(\Omega')} r'^{n+2} \, \mathrm{d}r' = \frac{1}{n+3} \left\{ \underbrace{[R + U(\Omega')]^{n+3}}_{1^{st} \text{ part}} - \underbrace{[R + L(\Omega')]^{n+3}}_{2^{nd} \text{ part}} \right\} \; . \tag{2.7}$$

From this point the RSM and the FSM differ. In the RSM a global spherical harmonic analysis (GSHA) is performed on Eq. (2.7) to determine the spherical harmonic coefficients of the potential field (*Lachapelle*, 1976). However, this is computationally expensive, because for every degree (n) an individual GSHA must be performed. Especially, when the spherical harmonic degree is large the time to compute the potential field is unpractical. The FSM was developed to tackle this problem.

In the FSM, the first and second part in Eq. (2.7) can be evaluated by a binomial series expansion (*Abramowitz and Stegun*, 1972). Writing $n + 3 = \nu$ and replacing U and L by their normalised values $\tilde{U} = \frac{U}{R}$ and $\tilde{L} = \frac{L}{R}$, we get

$$(R + U)^{\nu} - (R + L)^{\nu} = R^{\nu} \sum_{k=0}^{\nu} \binom{\nu}{k} \left[\tilde{U}^k - \tilde{L}^k \right] \; . \tag{2.8}$$
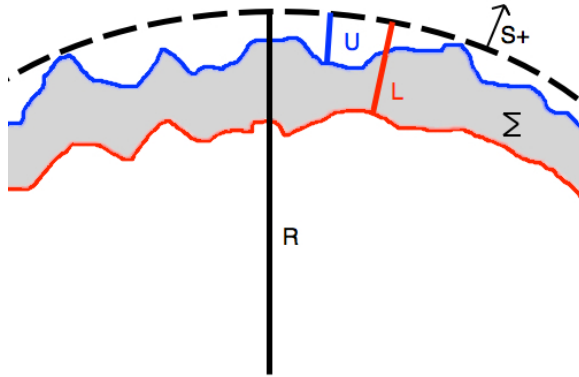
Figure 2.1: Sketch of of an arbitrary mass body. The distance (S) from the reference sphere R is defined positive upwards, resulting in $0 \geq U \geq L$.

The series summation contains a finite number of terms, as ν is a positive integer (*Abramowitz and Stegun*, 1972). To reduce the computational load, in practical applications (*Rummel et al.*, 1988) this series is truncated at a value α, where $\alpha < \nu$, resulting in

$$(R + U)^{\nu} - (R + L)^{\nu} = R^{\nu} \sum_{k=0}^{\alpha} \binom{\nu}{k} \left[\tilde{U}^k - \tilde{L}^k \right] + \epsilon_{\alpha} . \tag{2.9}$$

Here, ϵ_{α} is the error made by the truncation of the binomial series. An error analysis of this assumption follows in Section 3.1, but for now we will choose $\alpha = 3$ (*Rummel et al.*, 1988). By neglecting the higher-order terms, the radial integral from Eq. (2.7) becomes

$$\int_{r_{lower}(\Omega')}^{r_{upper}(\Omega')} r'^{n+2} \, \mathrm{d}r' \approx R^{n+3} \left[\frac{U(\Omega') - L(\Omega')}{R} + (n+2)\frac{U^2(\Omega') - L^2(\Omega')}{2R^2} \right.$$

$$\left. + (n+2)(n+1) \frac{U^3(\Omega') - L^3(\Omega')}{6R^3} \right] . \tag{2.10}$$

Following *Novák and Grafarend* (2006), we will use a short-hand notation, $F(\Omega')$, to denote everything between the square brackets of Eq. (2.10):

$$\int_{r_{lower}(\Omega')}^{r_{upper}(\Omega')} r'^{n+2} \, \mathrm{d}r' \approx R^{n+3} F(\Omega') . \tag{2.11}$$

Substituting Eq. (2.11) in Eq. (2.5) gives:

$$V(r,\Omega) = GR^2 \sum_{n,m}^{\infty} \left(\frac{R}{r}\right)^{n+1} \frac{1}{2n+1} Y_{nm}(\Omega) \int_{\Xi} \rho(\Omega') \, F(\Omega') \, Y_{nm}^*(\Omega') \, \mathrm{d}\Omega' . \tag{2.12}$$

Novák and Grafarend (2006) continue by performing GSHA of the density distribution function $\rho(\Omega')$ and the function $F(\Omega')$ separately. The spherical harmonic coefficients retrieved from the two separate GSHA procedures are combined in the spherical harmonics domain using complex Glebsch-Gordan series. However, the same result can be obtained by multiplying the mass density distribution $\rho(\Omega')$ with the function $F(\Omega')$ in the spatial domain and by subsequent GSHA of the combined function, i.e.,

$$\rho(\Omega') \, F(\Omega') \; \overset{GSHA}{=} \; \sum_{n,m}^{\infty} C_{nm} \, Y_{nm}(\Omega') \; . \tag{2.13}$$

Coefficients C_{nm} are derived from the density and geometry of the modelled layer. This approach requires one less GSHA which is favourable, because a GSHA is computationally expensive. Substituting Eq. (2.13) into Eq. (2.12) and reordering the integral and summation yields:

$$V(r,\Omega) = GR^2 \sum_{n,m}^{\infty} \left(\frac{R}{r}\right)^{n+1} \frac{1}{2n+1} \, Y_{nm}(\Omega) \; \times \sum_{n',m'}^{\infty} C_{n'm'} \int_{\Xi} Y_{n'm'}(\Omega') \, Y_{nm}^*(\Omega') \mathrm{d}\Omega' \; . \tag{2.14}$$

Using the orthogonality of fully-normalized spherical harmonic functions (*Heiskanen and Moritz*, 1984, p. 29) results in

$$V(r,\Omega) = GR^2 \sum_{n,m}^{\infty} \left(\frac{R}{r}\right)^{n+1} \frac{4\pi}{2n+1} \, C_{nm} \, Y_{nm}(\Omega) \; . \tag{2.15}$$

To compare the gravitational potential of the layer with global gravitational models referenced to a particular gravitational constant GM, the potential should be scaled accordingly using the following relation:

$$(GM)^{model} = \frac{4}{3} \, \pi \, \rho_E \, G \, R^3 \; . \tag{2.16}$$

in which, ρ_E is the average mass density of the reference Earth computed with GM and R from the global gravitational model. Substituting Eq. (2.16) into (2.15), yields:

$$V(r,\Omega) = \frac{GM}{R} \; \sum_{n,m}^{\infty} \left(\frac{R}{r}\right)^{n+1} V_{nm} \, Y_{nm}(\Omega) \tag{2.17}$$

with

$$V_{nm} = \frac{3}{2n+1} \, \frac{1}{\rho_E} \, C_{nm} \; . \tag{2.18}$$

The coefficients, V_{nm}, are referred to as the Stokes coefficients. The constructed gravitational potential is derived for a particular mass density layer in an Earth model. A more complex model can be built by adding the potential of several layers.

3   Error characterisation of the fast spectral method

In the derivations of the FSM, higher-order terms of the binomial series expansion were neglected to arrive to Eq. (2.10). Previous studies suggested that an expansion up to the third-order binomial term is enough to accurately model the gravitational potential of a topographic layer (*Rummel et al.*, 1988; *Vaníček et al.*, 1995). However, with the increasing accuracy of gravitational, digital elevation (DEM), and crustal models, the question arises if this finding is still valid. This section describes the effect of the binomial order truncation in Eq. (2.9) on the accuracy of the forward modelled gravitational potential. Moreover, we examine if this assumption is still valid for deeper layers.

It will be shown that the truncation of the binomial series introduces errors for layers that deviate substantially from the radius of the reference sphere, R, which cannot be reduced by truncating at a higher order. This is the case for crustal and upper mantle mass layers. To extend the capabilities of the FSM to deeper layers, an improved forward model is presented. First the error due to the truncation of the binomial series is discussed.

3.1   Characterisation of the truncation error

From Eq. (2.9) the error ϵ_α follows as:

$$\epsilon_\alpha = R^\nu \sum_{k=\alpha+1}^{\nu} \binom{\nu}{k} \left[\tilde{U}^k - \tilde{L}^k \right] = R^\nu \sum_{k=\alpha+1}^{\nu} \epsilon^{(k)}, \qquad (2.19)$$

where $\epsilon^{(k)}$ is a shorthand notation for the kth term in the summation. Our goal here is to find the smallest order at which the series can be truncated without introducing a substantial error in the results. To do so, we will derive a criterion that allows us to quantify the relative contribution of the leading order term $\epsilon^k (= \epsilon^{\alpha+1})$ in Eq. (26), compared to the entire error ϵ_α. In doing so, we quantify the reduction in the error that results from increasing α by 1.

To show how $\epsilon^{(k)}$ changes with increasing k, and thereby how ϵ_α changes with increasing α, we construct a variable $C^{(k)}$

$$C^{(k)} = \left| \frac{\epsilon^{(k+1)}}{\epsilon^{(k)}} \right| = \left| \frac{\nu - k}{k+1} \frac{\left[\tilde{U}^{k+1} - \tilde{L}^{k+1} \right]}{\left[\tilde{U}^k - \tilde{L}^k \right]} \right| . \qquad (2.20)$$

For $k = \alpha$, this variable is the relative change in the magnitude of the first term in Eq. (2.19), $\epsilon^{(\alpha+1)}$, when α is increased by one, so when Eq. (2.9) is truncated one order higher. Thus, it is a measure of the change in the first error term when adding an extra term to the binomial series. Since $\frac{\nu-k}{k+1}$ is continuously decreasing with k, and it can be numerically checked that this is also the case for $\left| \frac{\tilde{U}^{k+1}-\tilde{L}^{k+1}}{\tilde{U}^k-\tilde{L}^k} \right|$ for any practical values of $\tilde{U}$ and $\tilde{L}$, it follows that

$$C^{(k+1)} < C^{(k)}. \qquad (2.21)$$

However, in theory there could be cases where $C^{(k)} \geq 1$ and $C^{(k)} \approx C^{(k+1)}$. The error made when truncating Eq. (2.9) will not decrease substantially when adding a single additional term (*i.e.* when increasing α by 1). In fact, when $C^{(k)} > 1$, $\epsilon^{(k)}$ increases with k and increasing α by 1 will not even remove the largest error term.

Therefore, a stringent requirement is needed on $C^{(k)}$ to study the region where all remaining error terms are relatively small compared to the current leading order term, and increasing α by 1 will cause a substantial reduction of the total error. Such a requirement can be derived from Eq. (2.21) and from the fact that:

$$\sum_{k=2}^{l_{max}} \frac{1}{2^k} < \frac{1}{2},$$

(2.22)

for any finite l_{max}. The following criterion has to be met:

$$C^{(k)} \leq \frac{1}{2}.$$

(2.23)

This ensures that adding a single term to the binomial expansion will decrease the total error by *at least* a factor of 2 and that all remaining error terms will not be dominant compared to the current leading order error term:

$$\epsilon^{(k)} > \sum_{l=k+1}^{\nu} \epsilon^{(l)}.$$

(2.24)

Although this criterion (Eq. (2.23)) provides no guarantee that the total error is acceptable, it does follow that if Eq. (2.23) is not met, the error properties of higher order terms will be relatively influential and as a result α will likely need to be increased considerably to attain an acceptable error level. The criterion (2.23) will be called the convergence criterion.

Now that we have established a convergence criterion, we can compute the appropriate truncation limit for a potential field with a certain spherical harmonic resolution. For a given geometry (defined by $\tilde{U}$ and $\tilde{L}$) and truncation level α, using the convergence criterion in Eq. (2.23) yields the following condition for ν

$$\nu < \left| \frac{1}{2} \frac{\tilde{U}^\alpha - \tilde{L}^\alpha}{\tilde{U}^{\alpha+1} - \tilde{L}^{\alpha+1}} (\alpha + 1) + \alpha \right|,$$

(2.25)

where we have set $k = \alpha$ in Eq. (2.23). We reiterate that $\nu = n + 3$ and therefore ν indicates the maximum degree of the spherical harmonic expansion. From this relation it is clear that for thicker layers, for which $|\tilde{U} - \tilde{L}|$ is larger, ν has to be smaller than the limit in order for (2.23) to hold, as the influence of higher order terms in Eq. (2.9) increases. Similarly, for deeper layers, in which the magnitude of both $\tilde{U}$ and $\tilde{L}$ are increased by the same amount, the influence of the higher order terms is also stronger.

When we use a simplified geometry of an arbitrary mass layer in which we set the upper limit U equal to the circumscribing sphere, so that $\tilde{U}$ becomes 0, we obtain the following:

$$\nu < \left| \frac{\alpha + 1}{2\tilde{L}} + \alpha \right| \approx \frac{\alpha + 1}{2\tilde{L}},$$
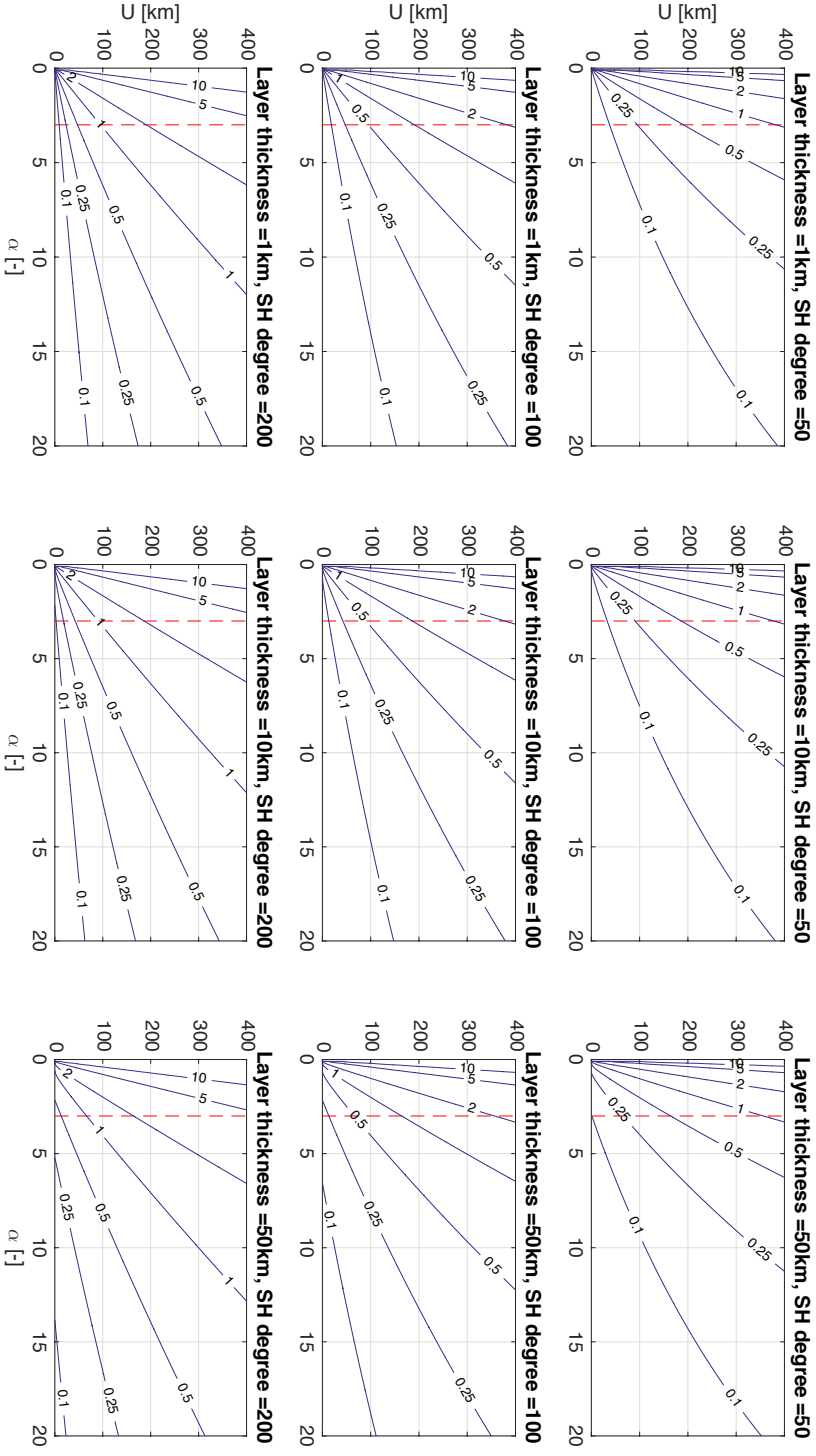
(2.26)

Figure 2.2: Contour plot of the values of $C^{(k)}$ as a function of U and α, for a number of values of the spherical harmonic degree $n = \nu - 3$ and layer thickness $|L - U|$. Dashed red lines indicate the currently typical $\alpha = 3$ truncation level.

where the approximation follows from the fact that typically $\tilde{L} \ll 1$. The above equation will still approximately hold true in cases where $|L| \gg |U|$, in which the upper limit of the entire boundary is close to, but not exactly on, the circumscribing sphere (relative to the thickness of the layer). The convergence criterion of equations (2.25) and (2.26) shows the following relation $\epsilon^{(k)} > \sum_{l=k+1}^{\nu} \epsilon^{(l)}$.

To illustrate the behaviour of $C^{(k)}$ with varying geometry and truncation level, we show its behaviour as a function of k and U in Figure 2.2, for a number of spherical harmonic degrees and layer thicknesses. Note that larger absolute values of U mean that the layer starts at a distance further away from the circumscribing sphere with radius R. It can be seen from Figure 2.2 that the value of $C^{(k)}$ is lower for a given value of k when (i) the layer is thinner, (ii) the layer starts closer to the reference sphere, and (iii) the spherical harmonic degree is smaller. Furthermore, Figure 2.2 shows that as k increases, the rate at which $C^{(k)}$ decreases levels off. In certain cases, this property can be advantageous for the practical application of Eq. (2.19), as it means that the majority of the error can be located in the low values of k. However, this no longer holds when $C^{(k)} > 1$, for which $\epsilon^{(k)}$ is increasing with k. In Figure 2.2, the $\alpha = 3$ truncation level that is typically used (*Rummel et al.*, 1988) is shown by a dashed vertical line. The intersection of this line with the $C^{(k)} = 0.5$ contour represents the point above which the binomial series expansion fails to comply with Eq. (2.23). From this level on, it cannot be assumed that the remaining error due to the truncation of the binomial series is small.

Figure 2.3 plots the spherical harmonic degree ν with respect to the value of the upper boundary U of the layer for the binomial order truncation, $\alpha = 3$. The value for U is an approximate representation for the deviation from the reference radius R. The characteristic degree that fulfils the convergence criterion quickly drops to low values when the depth of the layer increases. For layers with a depth of 100 km, spherical harmonic coefficients from around degree 80 and above contain large errors due to the truncation. At a depth of 200 km coefficients from degree and order 50 are affected, at 300 km coefficients from degree and order 30 are affected and at 400 km coefficients from degree and order 25 are affected.

For this study we use the spherical approximation, but for high-accuracy applications the ellipsoidal approximation is used. *Claessens and Hirt* (2013) use the same approach concerning the binomial series approximation, which is characteristic of the FSM, and truncate it after a few order of the binomial series. This is correct for topographic reduction, but we would expect similar errors occur in the ellipsoidal approximation when deeper density layers are forward modelled. The magnitude of these effects needs to be further investigated, but is outside the scope of this study.

3.2 Numerical error characterisation for topographic masses

If the convergence criterion is fulfilled the remaining error of the FSM for an arbitrary mass layer can be determined numerically, because the extra signal from an added binomial term is larger than the remaining error. Thus, it is an estimate of the maximum error at a certain binomial order truncation.

We use a topographic mass layer to numerically estimate the error. The topographic
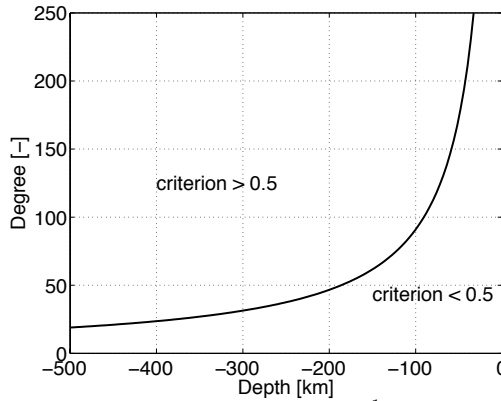
Figure 2.3: The boundary for an error criterion of $\frac{1}{2}$, as a function of the depth of the mass layer and the truncation limit. The depth represents the value of U and a truncation limit of $\alpha = 3$ is chosen.

mass reduction is derived from the global digital elevation model GTOPO30 reduced to a 0.1 x 0.1 arc-deg equiangular grid. Over the continental areas, the upper boundary is defined by topography and the lower boundary is the zero-elevation surface to which GTOPO30 is referenced. Over the oceanic areas the upper boundary is defined by the zero-elevation surface and the lower boundary by the bathymetry. The mass density of the topographic layer is set to the constant value of $\rho_{topo} = 2670$ kg/m^3 in the continental areas and for the oceanic areas the mass density of $\rho_{ocean} = -1750$ kg/m^3 is used. The goal of this test is not to represent the Earth's topography as accurately as possible, but to determine the effect of the number of binomial terms used for spectral forward modelling of the gravitational potential of such a layer. The gravitational field will be calculated on the geocentric sphere with the radius of $R = 6378.136$ km. This model fulfils the convergence criterion when a truncation limit of $\alpha = 3$ is used.

   The first gravitational solution is constructed by using only the Stokes coefficients of the first binomial term. The second gravitational solution is constructed by including the Stokes coefficients of the first and second terms in the binomial series. This is repeated up to the truncation value $\alpha = 10$. The cut-off value of the spherical harmonic representation, l_{max}, is varied as 90, 180, 360, 720, 1200 and 1800, which corresponds to the approximated grid resolutions of 2, 1, 0.5, 0.25 and 0.1 arc-deg, respectively. The results are presented in Figure 2.4, which shows the maximum difference in the radial component of the gravitational acceleration vector. It can be seen that only the first two binomial series terms are needed to represent the gravitational field up to 180 degree and order accurately enough (± 1 mGal), as concluded by *Martinec et al.* (1989), *Rummel et al.* (1988), and *Balmino* (1994). More terms are needed when the resolution of the topographic model is increased. For example, a 0.1x0.1 arc-deg resolution model needs spherical harmonic coefficients up to degree and order 1800 to be represented correctly. This will result in 6 more binomial terms when an accuracy of ± 1 mGal is required, similar results were obtained by *Hirt and Kuhn* (2012).
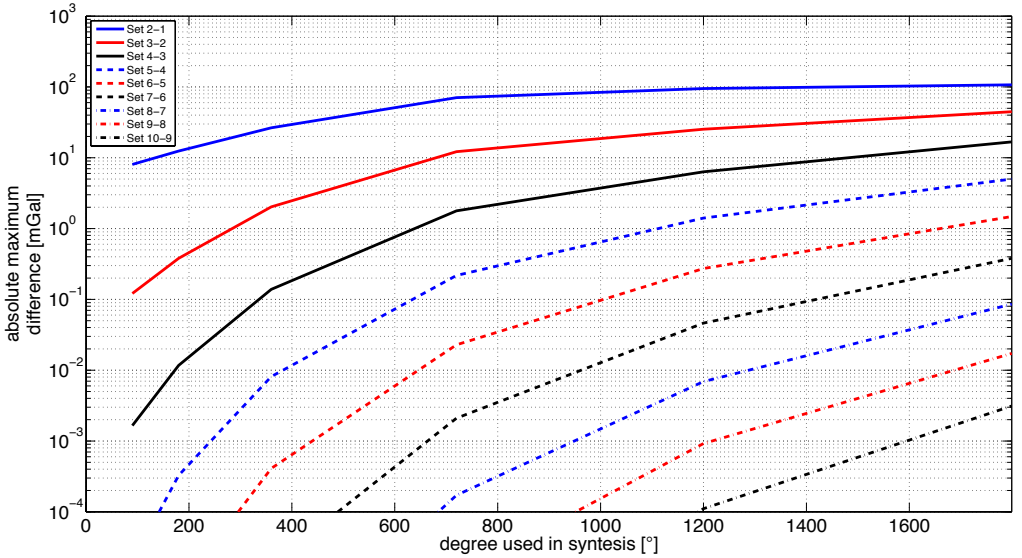
Figure 2.4: Difference between two gravitational solutions using a different number of binomial series term approximations as depicted in the legend.

4 Reducing the truncation error for deeper layers

To get insight into the numerical behaviour of the FSM for deeper mass layers that do not fulfil the convergence criterion, another modelling exercise is performed. The mass model consists of the same mass layer as in previous section, but now the zero-elevation reference is at 0, 50, 100, 200, 300 and 400 km depth. The computed gravitational fields should look similar, except for the damping effect of high degrees resulting from $\left(\frac{R}{r}\right)^{n+1}$ in Eq. (2.17). Figure 2.5a illustrates the degree variance of the spherical harmonic coefficients. At 0 km depth the degree variance follows approximately the Kaula rule as found by *e.g. Rummel et al.* (1988) and *Balmino et al.* (1973). The model at 50 km depth performs as expected with higher degree coefficients being damped more, as illustrated by an increasing difference between the blue and red line for higher degrees. However, a different behaviour is seen for the layer at 100 km depth. From degree and order 100 onward, the degree variance stays flat. For deeper layers, the degree variance increases with degree, because the model does not fulfil the convergence criteria. This behaviour is also seen in the degree variances of the models at 200, 300 and 400 km depth, but with a different location of the 'bending' point. In the spatial domain these errors are seen to generate random-looking patterns with a slight correlation to the geometry of the modelled layer, as we will see in the benchmark (Section 5).

When fitting a forward gravity model to gravity field observations, these errors can lead to mis-modelled densities. The errors arise because the density model does not fulfil the convergence criterion of Figure 2.3. In the following, we present a solution that
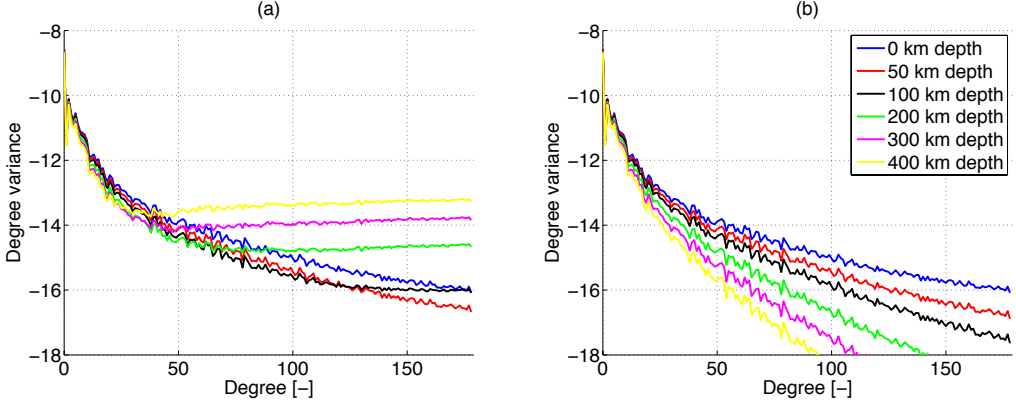
Figure 2.5: The degree variance of the spherical harmonic coefficients of the gravitational potential derived from the topographic mass density layer for different depths: 0, 50, 100, 200, 300 and 400 km: (a) without correction, and (b) with correction.

reduces this error significantly and makes it possible to use the FSM forward modelling for global 3-D mass density models at any depth.

Because the error appears for deeper layers we introduce a new reference sphere R^*, such that the upper bound is reduced to approximately 0. Then, Eq. (2.6a) should be modified to

$$r_{upper} = R^* + U^*(\Omega') \tag{2.27a}$$

$$r_{lower} = R^* + L^*(\Omega') . \tag{2.27b}$$

The new spherical radius is defined as $R^* = R - \check{U}$, with $\check{U}$ being the maximum value of $U(\Omega')$. The new upper bound is defined with respect to the new spherical radius, $U^* = U - \check{U}$ and the new lower bound is defined as, $L^* = L - \check{U}$. From here, the method proceeds as before until Eq. (2.13). This relation now produces spherical harmonic coefficients with respect to the new reference sphere

$$\rho(\Omega')F^*(\Omega') \stackrel{GSHA}{=} \sum_{n,m}^{\infty} C_{nm}^* \ Y_{nm}(\Omega') . \tag{2.28}$$

Here F^* is defined based on the new U^*, L^*, and R^* values and C_{nm}^* are the coefficients referenced to the sphere with radius R^*. To transform these coefficients to the original reference sphere, R, the following relation is used:

$$C_{nm} = \left(\frac{R^*}{R}\right)^n C_{nm}^* . \tag{2.29}$$

These C_{nm} coefficients are now compatible with those in Eq. (2.13), or in other words, they are referenced to the original reference sphere with radius R.

To show the effect of the approach, we show the degree variance of the coefficients C_{nm} computed using the correction in Figure 2.5b. The expected damping of higher
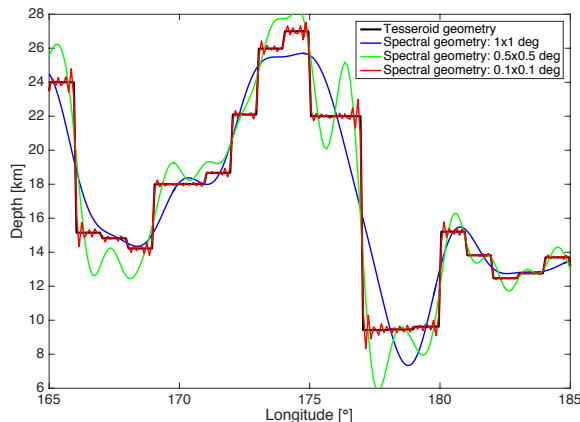
Figure 2.6: A cross section of the different Moho geometries used in the benchmark. The black line represents the tesseroid geometry approximation, the blue line represents the spherical harmonic geometry approximation with the 1x1 arc-deg resolution, the green line represents the spherical harmonic geometry approximation with the 0.5x0.5 arc-deg resolution, and the red line represents the spherical harmonic geometry approximation with the 0.1x0.1 arc-deg resolution.

degree spherical harmonic coefficients is visible in contrast to Figure 2.5a. The method now seems to produce correct gravitational potential fields for density layers at any depth, because it fulfils the convergence criterion, as can be confirmed in Figure 2.3. To test this a benchmark is performed in the next section.

5 Benchmark

To benchmark the improved FSM forward modelling software, a comparison is performed to the tesseroid software used by *Kaban et al.* (2010). This software uses an algorithm which computes the combined gravitational effect of elementary volumes that make up a spherical Earth (*Artemjev and Kaban*, 1994). The algorithm is based on the equations of *Strakhov et al.* (1989), improved by *Kaban and Mooney* (2001) and *Kaban et al.* (2002). The benchmark will compare the vertical component of the gravitational accelerations, as computed from a density model on an equiangular 1x1 arc-deg grid, which corresponds to a maximum degree and order of 179 in spherical harmonics coefficients. The model takes the global Moho depth from CRUST1.0 global crustal model (*Laske et al.*, 2013) with the density contrast of 450 kg/m^3. The geometry is referenced to a sphere with a radius of 6371 km. Also, the gravitational field results are calculated on this reference sphere. To obtain an accuracy of <1 mGal, 8 binomial terms are included in the calculations for the spectral method, as deduced from inspection of Figure 2.4.

The benchmark is challenging, because of a difference in both forward modelling techniques. The tesseroid method uses a block representation, whereas the FSM approximates the geometry of the mass layer with spherical harmonic functions. To reduce

this difference, we increased the resolution in the density models for the FSM solution. Figure 2.6 shows the difference between the geometries that are used by both methods for three spatial resolutions in the FSM, 1x1 arc-deg, 0.5x0.5 arc-deg, and 0.1x0.1 arc-deg. The higher resolution approximates the tesseroidal geometry much better. The high-resolution spectral geometry shows the well known Gibbs effects. However, the calculated gravity values are averaged over a 1x1 arc-deg potential field grid, therefore most of the Gibbs effect will be removed.

The results of the benchmark are shown in Figure 2.7. The 1x1 arc-deg potential field solution is compared to the tesseroid solution in Figure 2.7a and d, without and with a correction, respectively. Figure 2.7d shows a slight improvement compared to the uncorrected result, which was expected after inspecting the convergence criterion, because models up to order and degree 180 in the spherical harmonics can have geometries up to 100 km deep, according to Figure 2.3. This particular Moho model stays well within the correct domain of the convergence criterion. Nevertheless, the maximum difference between the tesseroid and corrected spectral gravitational solutions is $\pm$ 60 mGal, which is around 10% of the signal. This difference can be attributed to the different approximation methods for the geometry (Figure 2.6) and is best visible in regions with large gradients in geometry.

This difference should be reduced after increasing the resolution of the spectral method. Figure 2.7b and e show the results using the 0.5x0.5 arc-deg grid without and with a correction, respectively. Here, the residuals of the comparison become smaller, which can be attributed to a better approximation of the shape of the Moho boundary. The proposed correction still does not have a great effect, because at many locations the convergence criterion is passed. Except at the Himalaya and the Andes Mountain Range some differences can be seen between the corrected and not-corrected solution.

The gravitational potential of an even higher resolution model compared to the tesseroid solution is shown in Figure 2.7c and f, without and with a correction, respectively. The effect of failing the convergence criterion is clear, differences of $\pm 10^6$ mGal are visible (Figure 2.7c). Thus, despite the increased spatial resolution, the fast spectral method performs much worse than the lower spatial resolution model. That is because, to represent the 0.1x0.1 arc-deg resolution, the spherical harmonics coefficients must be estimated up to 1800 degree. From the convergence criterion we learn that in that case the mass layer cannot deviate more than 10 km from the reference sphere (Figure 2.3). Yet, in the benchmark the Moho interface is on average 30 km deep, which causes this particular model to fail the convergence criterion and produce large errors.

After improving the forward modelling by lowering the reference sphere as explained in the previous section, the differences of the corrected solution with the benchmark stay between ± 2 mGal almost everywhere. We expect some higher variations for large gradients in the geometries such as in the Himalayas and the Andes (4 mGal). Furthermore, a large difference of 15 mGal is found at the North pole, which can be attributed to the high resolution of the tesseroid method there, because of the equiangular grid. The spectral method is unable to perfectly represent similar geometrical shapes, therefore the gravitational effect at these locations is different. Moreover, Figure 2.7f shows a large correlation with the Moho geometry, which is also present in the 0.5x0.5 arc-deg solutions. This can be attributed to the Gibbs effect that is observed in Figure 2.6. These
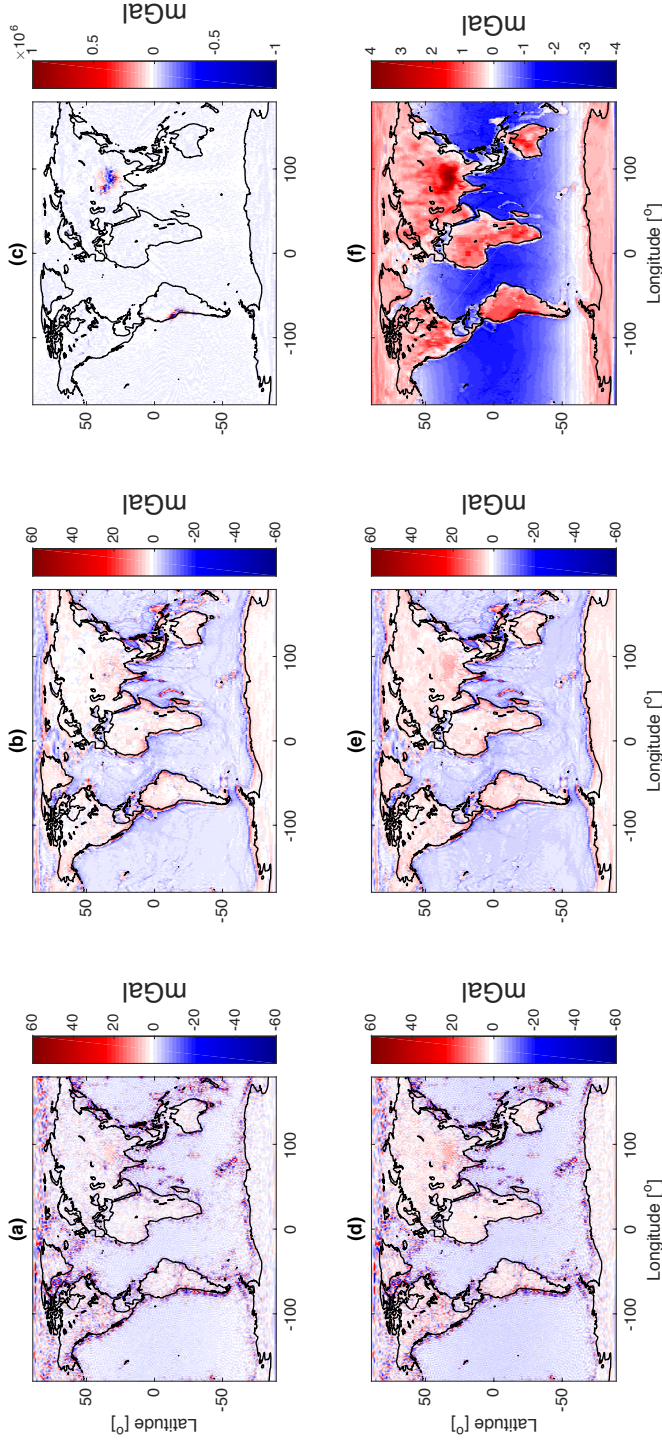
Figure 2.7: The difference between the tesseroid and the FSM forward modelling technique for (a) a 1x1 arc-deg spatial resolution without correction, (b) a spatial resolution of 0.5x0.5 arc-deg without correction, (c) a spatial resolution of 0.5x0.5 arc-deg without correction, and (d) a spatial resolution of 1x1 arc-deg with correction, (e) a spatial resolution of 0.5x0.5 arc-deg with correction, (f) a spatial resolution of 0.5x0.5 arc-deg with correction.

effects are not entirely symmetrical and will therefore not be averaged out completely. The resulting errors are below other gravity modelling errors. For example, *Mooney and Kaban* (2010) showed that errors due to uncertainty in sediment thickness will result in up to 12 mGal, uncertainty in Moho depth contributes to gravity anomalies of 30 mGal, and uncertainty in the thickness of the crystalline crust may reach up to 50 mGal.

Concluding, the benchmark shows that, despite the convergence error, the FSM can be improved to produce potential field solutions which differ from the tesseroid method less than the typical uncertainty in global gravity field modelling.

6   Conclusions

We have reviewed the fast forward gravitational modelling method using spherical harmonic representation (*Rummel et al.*, 1988). The FSM is capable of producing global gravitational potential fields from 3D-density structures after applying the correction proposed in this study. Because the results are computed in the form of spherical harmonic coefficients, they can be easily compared to geopotential models to which spectral filtering is applied. The method is computationally efficient compared to the rigorous spectral method in global topographic reductions.

Our analysis showed that the method is prone to large errors when modelling mass layers are situated at greater depths in the Earth, such as crustal and mantle layers. The error occurs due to truncation of the binomial series. A mitigation strategy for this depth-dependent error was devised by lowering the reference sphere during the global spherical harmonic analysis. This is followed by the transformation of the spherical harmonic coefficients back to the original sphere before their synthesis to a potential field. This strategy makes the spectral method capable of modelling the gravitational potential of mass density layers at any depth with the sufficient accuracy, as was demonstrated by benchmarking against a commonly used forward gravitational modelling software using tesseroids. The main difference between both methods is in the way how the geometry of the mass layers is approximated, where it can be argued that even though they imperfectly represent tesseroids, spherical harmonics are not necessarily less suitable to represent density variations than tesseroids. Despite these differences, similar gravitational field solutions were constructed with a difference of only ± 4 mGal, which is well below other model errors. Thus the method can be used for constraining global density models of the crust and upper mantle with gravity data.

Acknowledgements

Appendix: Introducing radial dependent mass density distribution

If the radial density distribution within a layer can be approximated by a polynomial model, then the following equations show how to use this particular distribution distribution with the FSM. The model was introduced for modelling atmospheric potential fields in *Novák* (2000). To simplify the derivation, a quadratic mass density distribution is taken:

$$\rho(r', \Omega') = \rho_0(\Omega') \left[\, 1 + a \, (R - r') + b \, (R - r')^2 \,\right] \qquad (2.30)$$

where $\rho_0(\Omega')$ is the mass density of the layer at $r' = R$, i.e. at the reference sphere and α and β are defined as:

$$a = \frac{\mathrm{d}\rho}{\mathrm{d}r'} \frac{1}{\rho_0} \;, \qquad (2.31a)$$

$$b = \frac{\mathrm{d}^2\rho}{\mathrm{d}r'^2} \frac{1}{\rho_0} \;. \qquad (2.31b)$$

When the mass density is dependent on r', the derivation of the FSM deviates starting from the radial integral in Eq. (2.5), because the mass density is now inside the integral:

$$\int_{r_{lower}(\Omega')}^{r_{upper}(\Omega')} \rho(r', \Omega') \, r'^{n+2} \mathrm{d}r' \;. \qquad (2.32)$$

Substituting Eq. (2.30) in the multiplication inside the integral as follows

$$\rho(r', \Omega') \, r'^{n+2} = \rho_0(\Omega') \left[\, r'^{n+2} + (a \, R + b \, R^2) \, r'^{n+2} - (a + 2b \, R) \, r'^{n+3} + b \, r'^{n+4} \right]. \quad (2.33)$$

Then, (2.32) becomes

$$\rho_0(\Omega') \Bigg\{ \frac{1 + aR + bR^2}{n + 3} \qquad \left[(R + U(\Omega'))^{n+3} - (R + L(\Omega'))^{n+3} \right]$$

$$- \frac{a + 2bR}{n + 4} \qquad \left[(R + U(\Omega'))^{n+4} - (R + L(\Omega'))^{n+4} \right]$$

$$+ \frac{b}{n + 5} \qquad \left[(R + U(\Omega'))^{n+5} - (R + L(\Omega'))^{n+5} \right] \Bigg\} \qquad (2.34)$$

The relation can be simplified by the same procedure as previously using the binomial series expansion. After truncating the binomial series the radial integral eventually results in

$$\rho_0(\Omega') \, R^{n+3} \Bigg\{ \frac{(U - L)}{R} + \frac{(n + 2) - aR}{2R^2}(U^2 - L^2)$$

$$+ \frac{(n + 2)(n + 1) - 2(n + 2)aR + 2bR^2}{6R^3}(U^3 - L^3) \Bigg\} \;. \quad (2.35)$$

Equation 2.35 is similar to Eq. (2.10) but with extra terms resulting from the polynomial density gradient coefficients. After this, the derivation proceeds as for the FSM for layers with constant density. The second-order polynomial coefficients, a and b, are visible in the second and third terms of the binomial series expansion. When examining this further, higher-order polynomial coefficients would modify the fourth and higher terms of the binomial expansion. When only three terms are used in the series expansion, a cubic polynomial for the radial mass density distribution cannot be used.

Paper II - Glacial Isostatic Adjustment in the static gravity field of Fennoscandia

"In the second place the assumption may be wrong that there have been no other processes going on in this part of the Earth's crust besides the isostatic readjustment. Part of the vertical movements or part of the gravity anomalies might have been caused by other phenomena. Considering these possibilities it is indeed remarkable that the agreement is as good as it is."

– F.A. Vening Meinesz, *The determination of the Earth's plasticity from post-glacial uplift of Scandinavia, (Physics,1937)*

Glacial Isostatic Adjustment in the static gravity field of Fennoscandia

B.C. Root[a], *W. van der Wal*[a], *P. Novák*[b], *J. Ebbing*[c], *and L.L.A.Vermeersen*[a,d]

Abstract

In the central part of Fennoscandia the crust is currently rising, because of the delayed response of the viscous mantle to melting of the Late Pleistocene ice sheet. This process, called Glacial Isostatic Adjustment (GIA), causes a negative anomaly in the present-day static gravity field as isostatic equilibrium has not been reached yet. Several studies have tried to use this anomaly as a constraint on models of GIA, but the uncertainty in crustal and upper mantle structures has not been fully taken into account. Therefore, our aim is to revisit this using improved crustal models and compensation techniques. We find that, in contrast with other studies, the effect of crustal anomalies on the gravity field cannot be effectively removed, because of uncertainties in the crustal and upper mantle density models. Our second aim is to estimate the effects on geophysical models, which assume isostatic equilibrium, after correcting the observed gravity field with numerical models for GIA. We show that correcting for GIA in geophysical modelling can give changes of several km in the thickness of structural layers of modeled lithosphere, which is a small but significant correction. Correcting the gravity field for GIA prior to assuming isostatic equilibrium and inferring density anomalies might be relevant in other areas with ongoing post-glacial rebound such as North America and the polar regions.

keywords: Glacial Isostatic Adjustment, static gravity field, Fennoscandia, crustal structures

1 Introduction

The static gravity field of Fennoscandia is known with high accuracy ($\pm$ 2 mGal) at a wavelength of 100-200 km (*Mayer-Gürr et al.*, 2011). Figure 3.1 shows the satellite-derived free-air anomaly observed in the Fennoscandian region. The negative gravity anomaly observed in the Bay of Bothnia (for geographical references see Figure 3.2) is linked to the Glacial Isostatic Adjustment (GIA) in that area (*Heiskanen and Vening Meinesz*, 1958),(*Balling*, 1980), and (*Sjöberg et al.*, 1994). However, the characteristic elliptic shape of GIA is not immediately visible in the static gravity field. Other sources contribute to the gravity field, such as density anomalies in the crust or mantle, crustal thickening or even a long-wavelength feature related to the Icelandic mantle plume (*Marquart*, 1989; *Steffen and Wu*, 2011). The question that arises is whether,

---

(a): Delft University of Technology, The Netherlands
(b): University of West Bohemia in Pilsen, Czech Republic
(c): NGU in Trondheim, Norway
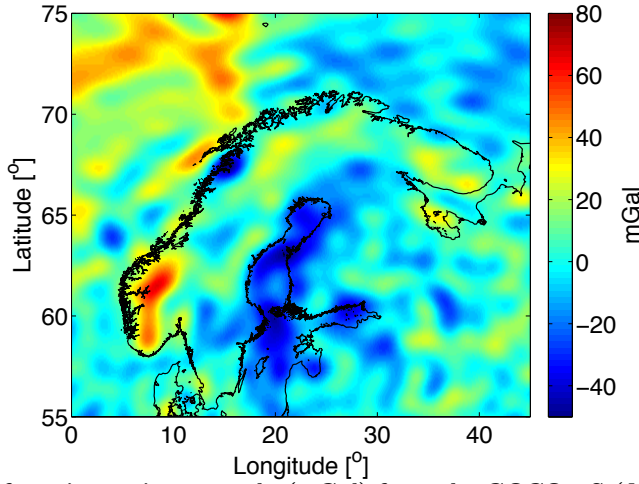(d): NIOZ, Texel, Netherlands

Figure 3.1: The free-air gravity anomaly (mGal) from the GOCO03S (*Mayer-Gürr et al.*, 2011) model up to spherical harmonic degree and order 180.

given the contribution of all these sources, it is possible to extract information from static gravity field observations to constrain GIA modeling. In the following, the free-air gravity anomaly that exists at present due to incomplete rebound will be referred to as the GIA gravity signal, or gravity anomaly.

Several studies have aimed to separate the GIA gravity signal from the observed gravity field. However, the conclusions of these studies differ significantly. *Heiskanen and Vening Meinesz* (1958) estimated a contribution of -20 mGal to the gravity anomaly, but stated that local density anomalies made the problem very complex. *Honkasolo* (1964) could not find a spatial correlation between the gravity anomaly and the region of GIA induced uplift. *Balling* (1980) concluded that -15 to -20 mGal in the area could be explained by post-glacial uplift after removing the gravity anomaly correlated with topography. This number was subsequently used to constrain mantle viscosities in GIA modeling (*Peltier and Wu*, 1982; *Wu and Peltier*, 1983; *Mitrovica and Peltier*, 1989). However, *Anderson* (1984) suggested that crustal structures explain a large part of the observed gravity anomaly and should be accounted for. After removing the effect of crustal thickening, the negative anomaly in the gravity field was almost completely removed (*Marquart*, 1989), supporting the conclusion that crustal thickening is dominant in the gravity field. A more elaborate method (*Sjöberg et al.*, 1994) improved on this study and concluded that post-glacial uplift was responsible for -28 mGal and crustal thickening for -12 mGal in the observed gravity anomaly. In a recent study, *Sjöberg and Bagherbandi* (2013) apply bandpass filtering to the spherical harmonic coefficients, assuming the GIA signal resides mainly between coefficients of degree and order 10 and 70. They obtain a negative geoid anomaly of -12 m, which corresponds to a negative free-air anomaly of -30 mGal in central Fennoscandia.

The largest limitation of most of these studies was the use of a homogeneous crust
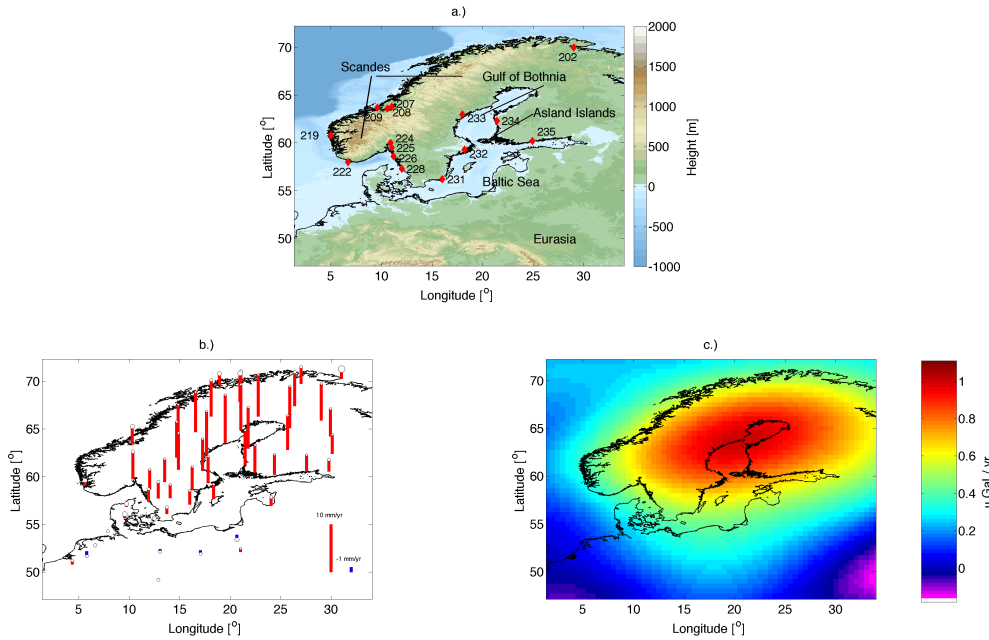
Figure 3.2: These figures represent the datasets used in this study. a.) The topography of Northwestern Europe with the locations of the regional relative sea level (RSL) observation sites (red diamonds) that are used in this study. b.) The location of the GPS stations with the value of vertical motion (*Lidberg et al.*, 2007). The white circles are error estimates. Red bars show uplift and blue bars represent measured subsidence. c.) Gravity rate estimated from GRACE data for the period January 2003 to December 2011 after smoothing with 400 km Gaussian filter halfwidth.

(*Kakkuri and Wang*, 1998). With the increasing number of seismic measurements in the area it was possible to construct an improved crustal density model. With this improved crustal model *Kakkuri and Wang* (1998) concluded that the negative gravity anomaly produced by crustal effects was actually twice as large as the observed gravity anomaly and the density variations in the upper mantle made a dominant contribution to the observed gravity field. A more recent study (*Kaban et al.*, 2010), with improved crustal models shows a positive residual gravity anomaly in the Bay of Bothnia after the removal of crustal effects, leaving no contribution for the GIA gravity signal. *Ebbing* (2012) proposed a model for the lithosphere and mantle in which crustal thickness variations were compensated by intra-crustal densities to achieve isostatic equilibrium. This model leaves up to -20 mGal unexplained in the area of GIA.

Given these different conclusions the question is still open on whether it is possible to separate the gravity effect caused by GIA from other sources. This study explores the possibilities to observe and separate the GIA gravity signal from static gravity field observations using improved crustal models of Fennoscandia and various assumptions of isostatic compensation. Furthermore, we will investigate the opposite question, whether the effect of a GIA correction in a geophysical model, which assumes isostasy, is signifi-
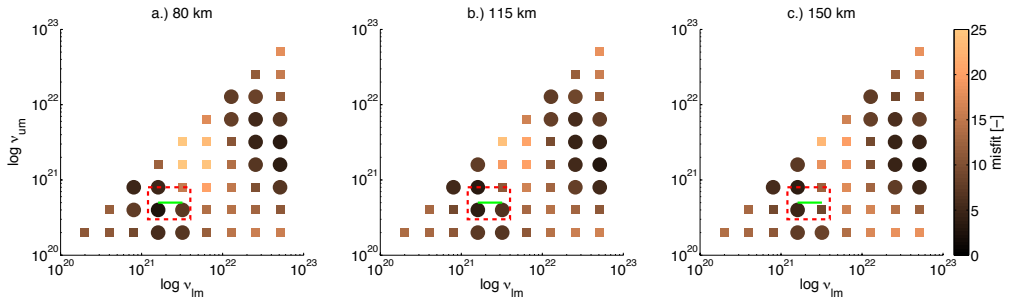
Figure 3.3: Misfit with respect to the selected (see Appendix B) relative sea level data (RSL) of *Tushingham and Peltier* (1992) in Fennoscandia for the GIA model with varying upper and lower mantle viscosity with three different lithosphere thicknesses: a.) 80 km, b.) 115 km, and c.) 150 km. Parameter combinations for which the misfit falls within the 95% confidence region are shown by circles. The dashed red area represents the range of viscosities of VM2 (*Peltier*, 1996) and the green solid line represents the VM5a (*Peltier and Drummond*, 2008) viscosity model. Viscosities are in Pas.

cant.

2   GIA model

The magnitude and uncertainty of the GIA gravity effect is computed for comparison with the uncertainty in the gravity field models introduced by current density models of the crust. The GIA model is based on the normal mode method (*Wu and Peltier*, 1982) for a multi-layer model (*Vermeersen and Sabadini*, 1997) with self-consistent sea-levels (*Mitrovica and Peltier*, 1991). Details are given in *van der Wal et al.* (2009). Geocenter motion has been added but not rotational feedback, as this latter effect is quite small in regional studies. The ice model ICE-5G is used as ice loading model (*Peltier*, 2004), representing one full glacial cycle up to 122 ka. Adding another glacial cycle does not significantly change the selection of preferred GIA models. Also, the remaining gravity anomaly and deflection of the lithosphere in Fennoscandia are not affected significantly. To support these statements, a worst case scenario was modeled. The results in the remainder of this study will be modelled with only one ice cycle. For details see Appendix A. The GIA models that have the lowest misfit to relative sea level data, GPS-based uplift rates, and GRACE observed gravity change, will be used in the rest of the study.

An incompressible Maxwell rheology is used, where the viscosity is varied in two layers of the mantle separated at the 670 km discontinuity. These layers can be resolved using misfit minimisation of sea level data. *Paulson et al.* (2007) found a small effect of compressibility on misfit for GRACE data and RSL data in North America. We assume the same holds for Fennoscandia, in which case the choice of preferred models is not affected. Neglecting compressibility does affect the displacement and induced gravity anomaly of our models, but we think that the estimated uncertainties from variations
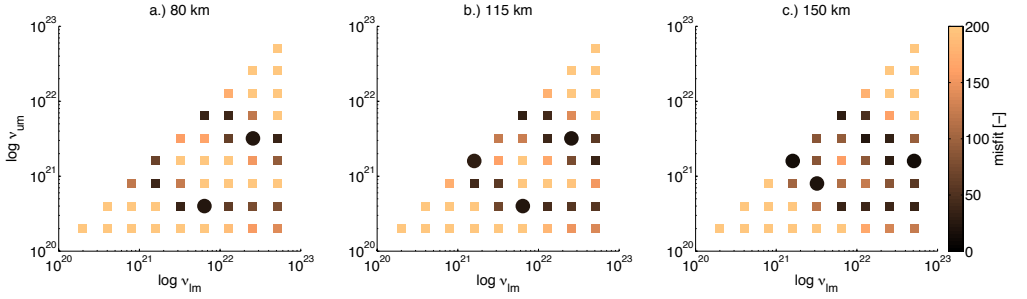
Figure 3.4: Misfit with respect to GPS data from the BIFROST project (*Lidberg et al.*, 2007) with three different lithosphere thicknesses: a.) 80 km, b.) 115 km, and c.) 150km. Viscosities are in Pas.

in viscosity are large enough to accommodate the effect of compressibility. Upper and lower mantle viscosity are varied from 2×10^{20} Pas to 512×10^{20} Pas in steps of a factor 2. The elastic lithosphere is modeled with a thickness of 80, 115, and 150 km, to sample the range of plausible values for lithosphere thicknesses in Fennoscandia (*Whitehouse*, 2009), (*Steffen and Wu*, 2011). There are three issues and assumptions in our modelling that need to be addressed. First, ICE-5G implicitly uses a certain mantle viscosity profile. However, since ICE-5G is created in a global sense, it is possible that regionally the rheology deviates, and regional studies have commonly varied viscosity for a fixed ice loading history (*Milne et al.*, 2001), (*Wang et al.*, 2008), and (*Steffen et al.*, 2010). Second, the uncertainty in the ice loading history is not known and third, the mantle viscosity does not only vary in radial directions. To deal with the last two issues we also compare output from a GIA model that uses an ice model that was created independently from mantle rheology, with our results. Viscosity in the Earth model component of the GIA model varies laterally as well as radially. Misfit analysis in *van der Wal et al.* (2013) already yielded preferred models and the model output is used as is.

Models are searched which minimise a chi-squared misfit with respect the observational data, defined as:

$$\chi^2 = \frac{1}{N} \sum_{i=1}^{N} \left(\frac{o_i - p_i}{\sigma_i} \right)^2 \tag{3.1}$$

Here, N is the number of observations, o_i are the observations, p_i are the predicted values from the models interpolated at the measurement locations and σ_i are the standard deviations corresponding to the observations. Certain models with a different viscosity distribution can result in a misfit which is statistically indistinguishable from the best-fitting model. To obtain a confidence region we use a contour that contains 95 percent of the probability distribution of the parameters (*Press et al.*, 1992). For the 2 degrees-of-freedom in these models this is represented by a χ^2 misfit contour that differs less than 5.99 with the minimal misfit value.

As the first data source we use the relative sea level (RSL) data from the database of *Tushingham and Peltier* (1992) to constrain the GIA modelling. Only RSL sites sensitive
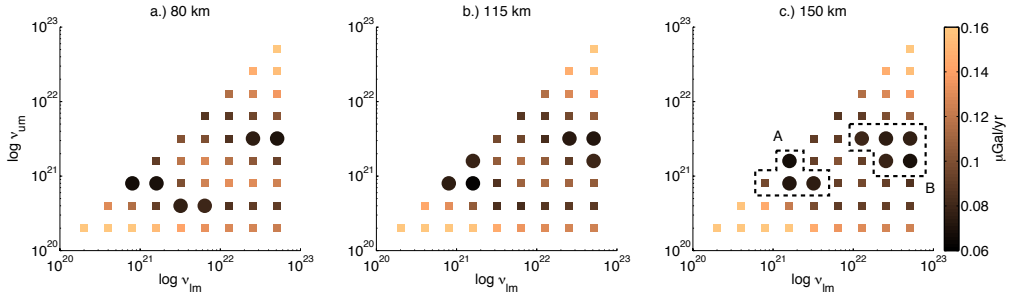
Figure 3.5: The standard deviation of the difference between the models and GRACE time-variable gravity observations with three different lithosphere thicknesses: a.) 80 km, b.) 115 km, and c.) 150km. The circles in the plot denote standard deviations smaller than 0.08 μGal/yr. Viscosities are in Pas. The black dashed areas are the selected viscosity profiles for model set A and model set B.

to Fennoscandia deglaciation are used to obtain an estimate for the regional viscosity profile. The used geological sites are shown in Figure 3.2a and the RSL curves can be found in Appendix B. For σ_i, both the height errors and timing errors are incorporated in a similar fashion as *van der Wal et al.* (2011). The misfit results are shown in Figure 3.3 for three different lithosphere thicknesses. The misfit plots show two regions of low-misfit which is observed in misfit plots for other GIA observables (e.g. (*Lidberg et al.*, 2010), (*Schmidt et al.*, 2014)) and is sometimes called bifurcation (*Schmidt et al.*, 2014). One area of low misfit is close to the viscosity profiles of VM5a (*Peltier and Drummond*, 2008) and VM2 (*Peltier*, 1996), depicted in Figure 3.3 by the green line and the red dashed area, respectively. Also, the average viscosity found in the study by *Mitrovica* (1996) of 0.65-1.10 $\times 10^{21}$ Pas is within this region. Furthermore, there are no significant changes between the results of different lithosphere thicknesses. The results show that this particular set of RSL observations is not capable to distinguish between lithosphere thicknesses in our area of interest. Part of the reason is that different subsets of the Fennoscandian RSL data set prefer different lithosphere thicknesses (*Steffen et al.*, 2014) possibly as a result of actual variation in lithosphere thickness. The second region of low misfit, which contains the minimum misfit, is found for models with an upper mantle viscosity of $1.6 - 3.2 \times 10^{21}$ Pas and a lower mantle viscosity of 5.12×10^{22} Pas. These values are situated in the top-right area in Figure 3.3. It is known that the lower mantle viscosity cannot be constrained by Fennoscandian data, therefore it will not be discussed further. The upper mantle viscosity is at the high end of the viscosity ranges in most studies for Scandinavia. We do note that some of the RSL curves predicted by the model with high upper-mantle viscosity do not fit well to the data (Appendix B). Also, misfit according to equation (3.1) is sensitive to the fit in only one or a few sites with small standard deviation due to the power of two in the equation (e.g. (*van der Wal et al.*, 2010)). Still there are studies which show a good fit of models with upper mantle viscosity above 10^{21} Pas to measure uplift rates or sea-level rates ((*Davis et al.*, 1999), (*van der Wal et al.*, 2011), (*Schmidt et al.*, 2014)).
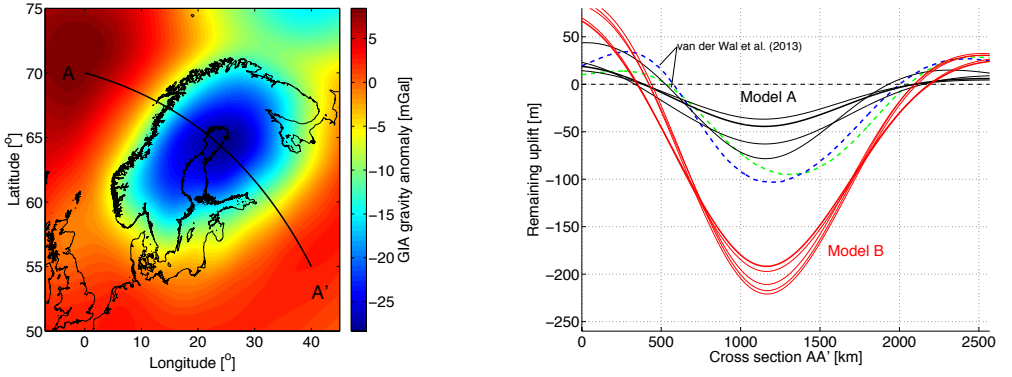
Figure 3.6: a.) Current free-air gravity anomaly due to GIA (Model B) b.) Remaining uplift for the different GIA models. Black lines represent model A with the thick black line being the best fitting model as described in the text ($\nu_{um} = 8 \times 10^{20}$ Pas and $\nu_{lm} = 16 \times 10^{20}$ Pas). Red lines represent model B with the thick red line being the best fitting model ($\nu_{um} = 16 \times 10^{20}$ Pas and $\nu_{lm} = 256 \times 10^{20}$ Pas). The blue dashed line represents the GIA model with dry composite rheology with grain size of 10 mm. The green dashed line represents a GIA model with dry composite rheology with a grain size of 4mm (van der Wal et al., 2013).

This bifurcation in the misfit plots cannot be resolved solely using RSL observations. Therefore, a similar comparison is made between the GIA models and GPS determined uplift rates at 53 sites in Fennoscandia from the BIFROST project, see table 1 in *Lidberg et al.* (2007). Misfit values are computed using equation (3.1). The preferred misfits are denoted by the solid circles in Figure 3.4. Here, a confidence region of 99 percent is chosen (9.21 away from the minimal misfit), because of the small uncertainties in the GPS measurements and the large misfit values. This comparison shows a different misfit pattern than for the RSL results, but the bifurcation is still visible. Fewer GIA models offer an explanation for the GPS data, as only three to four models pass the misfit criteria. The misfit becomes smaller with increasing lithosphere thickness.

To complete the GIA model selection, the GIA model results are also compared with gravity change observations of the GRACE satellite mission. We use CSR release 5 solutions from September 2002 until November 2012. The observations are filtered with a Gaussian filter with 400 km halfwidth (see Figure 3.2c). In this case the chi-squared misfit of equation (3.1) could not be used, since there is no meaningful standard deviation corresponding to the GRACE observations in Fennoscandia. Formal errors, computed according to the procedure of *Wahr et al.* (2004), are largely constant across Fennoscandia, around 0.02 μGal/yr, but systematic errors are not well known. Therefore, the standard deviation of the difference between the observation and model results is shown in Figure 3.5 instead. The solid circles represent comparisons with a standard deviation less than 0.08 μGal/yr. These figures show similar results as in the RSL and GPS cases. Again two regions where the models represent the observations best can be observed in Figure 3.5. Furthermore, a slight decrease in standard deviation is noticed with increasing lithosphere thickness. The GRACE data confirms the conclusions from the RSL and GPS measurements, but is also not able to distinguish between the two
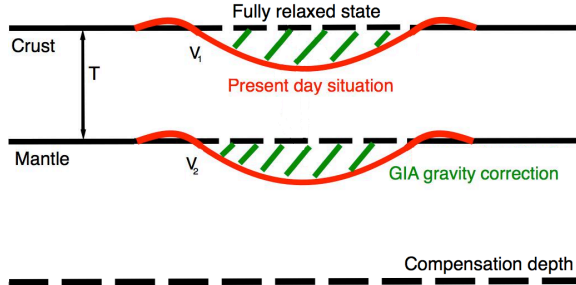
Figure 3.7: Sketch illustrating the lithosphere in isostatic equilibrium (black lines) and the lithosphere bended as it is still relaxing from the load of a former ice sheet (red lines). The green-shaded volumes are responsible for the GIA gravity effect.

regions of low misfit.

By inspecting the RSL, GPS and GRACE observations in the comparisons with the GIA models results, two sets of GIA models are selected, model set A and model set B. Both models have a lithosphere thickness of 150 km, due to the observed slight decrease in misfit with GPS and GRACE data for an increasing lithosphere thickness. Model set A represents the choice of viscosities that agrees with viscosity profiles VM2 and VM5a. Model set B represents a viscosity profile with larger upper and lower mantle viscosity. The GIA models that are used in the construction of these two models are shown in Figure 3.5 by the dashed black areas. They were selected, because most of the GIA models are situated in minimum misfit contours of the RSL comparison. The GIA model with viscosity profile, $\nu_{um} = 8 \times 10^{20}$ Pas and $\nu_{lm} = 32 \times 10^{20}$ Pas was added to model set A, because of the evidence in the misfit comparison of GRACE data.

To illustrate the models, Figure 3.6a shows the free-air gravity anomaly for the GIA model with viscosity profile, $\nu_{um} = 16 \times 10^{20}$ Pas and $\nu_{lm} = 256 \times 10^{20}$ Pas (Model B). The shape of the gravity anomaly is similar to the measured uplift rates (*Lidberg et al.*, 2007). The minimal value of the GIA static gravity anomaly can be found in the Gulf of Bothnia. This extreme is close to where the maximum ice thickness of the Late Pleistocene ice sheet is believed to have been situated. This is also the location of maximum gravity change, according to the GRACE gravity measurements and corroborated by the GPS uplift measurements, which observe maximal uplift in that area. Furthermore, Figure 3.6b shows the different remaining uplift or deflection of the lithosphere results of the selected models at cross section AA'. A clear distinction between model set A and B is noticed. Model set A has a minimum deflection of -57 m (± 20 m) and a minimum free-air gravity anomaly value is -8.2 mGal (± 2.9 mGal). Model set B shows a minimum deflection of 196 m (± 21 m) and a corresponding minimum free-air gravity anomaly value of -28.3 mGal (± 3.0 mGal). These values are constructed by calculating the mean deflection and gravity anomaly of the model set, whereas the uncertainty is found by computing the minimal and maximal deviation from the mean in the selected sets of GIA models.

To show the effect of another ice loading model and 3D composite mantle rheology, GIA models from *van der Wal et al.* (2013) are also shown in Figure 3.6b. The
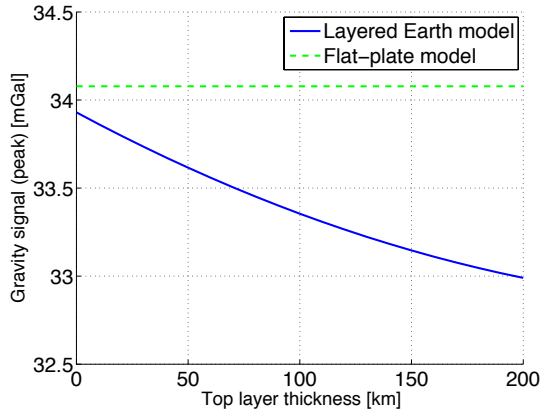
Figure 3.8: The GIA gravity signal for a flat-plate model (*Watts*, 2001) (green) and the spherical layered Earth model with varying lithospheric thickness, as described in the text (blue).

Table 3.1: The GIA gravity anomaly contributions from the different lithosphere models experiencing the GIA deflection. The simple model (*Watts*, 2001) is able to describe the gravity signal almost completely. The gravity signal of the multi-layer model is created by the sum of effects of uplift of the separate density contrasts.

Density contrast	Gravity signal [mGal]	Percentage
GIA modeling	28.7	100
Simple model (*Watts*, 2001)	28.6	∼99
Multi-layer model		
Topographic boundary	21.2	74.0
Intra-crustal boundaries	4.6	16.1
Moho boundary	3.0	10.4
LAB	-0.1	-0.5

blue dashed line represents a GIA model with dry rheology with grain-size of 10 mm and mantle temperatures derived from surface heat-flow data. The green dashed line represents a GIA model with a dry rheology and 4 mm grain-size, but with mantle temperatures derived from a global tomography model. The ice loading history is created from a simple ice flow law with ice extent matching geologic evidence. These models provided the best match to the observed maximum uplift rate in Scandinavia. Despite using a 3D rheology and a different ice loading model, the results are similar to model A.

The bifurcation in the comparison with RSL and uplift rate observations could be resolved by looking at the static gravity field. The gravity anomaly of model set A fits best with the predictions of *Balling* (1980) and *Heiskanen and Vening Meinesz* (1958).

The gravity anomalies of model set B are more negative, being in the range of -25 and -30 mGal (*Mitrovica and Peltier*, 1989), (*Sjöberg et al.*, 1994), and (*Sjöberg and Bagherbandi*, 2013). The spread in predicted gravity anomalies shows that the observed static gravity anomaly could be a useful constraint on GIA modelling, provided that the uncertainty from other static gravity sources can be corrected for. As stated in the introduction, one of the aims of this study is to find out if the observed gravity anomaly can be used as constraint, given uncertainties in crustal models. The answer will be shown to be negative.

3   The relation between the GIA gravity signal and lithosphere deflection

In this section the relation between the bending of the lithosphere due to the ice loading and the GIA gravity effect in the static gravity field is discussed. We use this relation in Section 4.4 to correct for the GIA gravity signal. The gravity signal due to the post-glacial deflection can be approximated with the following equation (*Watts*, 2001):

$$\Delta g_{GIA} \approx 2\pi G y \rho_{mantle} \tag{3.2}$$

Here, ρ_{mantle} is the mantle density, y is the vertical deflection which depends on the location, and G is the universal gravitational constant. The thickness of the lithosphere drops out of the equations in the approach described in *Watts* (2001), because only mantle material is removed, but in reality a thicker lithosphere will put the source of that particular mass source deeper. The assumption that the lithosphere thickness has a negligible effect on the GIA gravity signal is tested using a simple model sketched in Figure 3.7. This model consists of two layers of constant thickness. The upper layer, which simulates the lithosphere, is bended with both its upper boundary (V_1) and its lower boundary (V_2) having the same deflection according to the GIA model results. The lower layer simulates the asthenosphere, where its lower boundary remains at a constant depth of 300 km. The top layer has a mean density of 2650 kg/m^3 and the lower layer has a mean density of 3300 kg/m^3. These values are representative for the Fennoscandian area (*Ebbing*, 2007a). Figure 3.7 shows the deflected lithosphere in its current state and in its fully relaxed form. Due to the mass deficit in the current state a negative gravity anomaly is present, compared to the fully relaxed state. With the methodology explained in *Novák and Grafarend* (2006), the gravity effect can be forward modeled. The thickness, T, of the elastic layer in the model is varied from 0 to 200 km thickness, which covers most known lithospheric thicknesses. A deflection with a peak value of 245 m is used, resembling the maximal possible deflection of GIA model results in model B with a lithosphere thickness of 80 km in order to obtain the largest gravity signal. Figure 3.8 shows a small variation between the value from equation (3.2) at the location of maximal deflection and the modeled results with varying lithosphere thickness. A difference of around 1 mGal is seen when the lithospheric thickness increases to 200 km. This is well below the uncertainty in the observed gravity field in Fennoscandia. Thus, equation (3.2) is a good approximation for correcting the gravity field for GIA in Section 4.4.
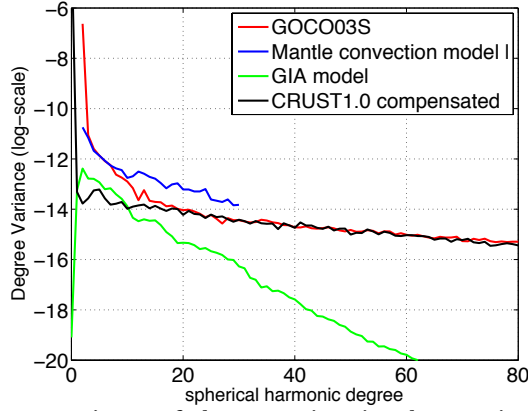
Figure 3.9: The degree variance of three gravity signals: gravity observations based on the model GOCO03S (red), a mantle convection model (*Tosi*, 2007) (blue), best fitting GIA model from set B (green), and gravity signal from the top 100 km layers of the Earth, based on a compensated CRUST1.0 density model (black).

This simple two-layer model can be expanded to a multi-layered Earth model that is used in the GIA modeling of section 4.2, since the total GIA gravity signal is a summation of effects due to the uplift of different density contrasts. The GIA deflection obtained from the GIA modeling was superimposed on each layer of the multi-layered Earth model to calculate the contribution to the GIA gravity signal (Δg_{GIA}) for that specific layer. The Earth model that is used comprises one sedimentary layer with a density of 2500 kg/m^3, three crustal layers with density increasing with depth from 2700 to 2950 kg/m^3 and two mantle layers consisting of an elastic lithosphere with a density of 3330 kg/m^3, slightly higher than the viscous asthenosphere (3300 kg/m^3). Incompressible elastic bending is assumed in the lithosphere. The results of the forward modeling are shown in Table 3.1 and compared with the gravity anomaly computed by the GIA model described in section 2. The topographic contribution to the GIA gravity signal is the largest, 74.0 percent (21.2 mGal), because the topographic boundary has the largest density contrast ($\rho_{air} - \rho_{crust}$). The second most important density contrast is the Moho. The deflection of this density contrast introduces a contribution to the GIA signal of 10.4 percent (3.0 mGal). The rest of the GIA gravity signal is produced by the deflection of the internal density contrasts in the crust, added together they contribute 16.1 percent (4.6 mGal) to the complete GIA gravity signal. The density contrast of the sedimentary layer and upper crustal layer in this Earth model is small, so it will have a small effect in the GIA signal. However, this could be different in areas where the density contrast between sedimentary and crustal layers is significant. The gravity effect due to the lithosphere-asthenosphere boundary (LAB) is opposite in sign due to the inverse density contrast, removing 0.5 percent of the GIA gravity signal. The complete gravity signal can be almost completely reproduced using equation (3.2) with the density of the asthenosphere, because when all the different density contrasts are combined, they add up to the asthenosphere density. This also holds for models with

continues radial density distributions.

4   Results and discussion

First we aim to answer the first research question, namely: can the GIA gravity signal be isolated from the observed gravity signal? Doing so would require a density model of the lithosphere, based on seismic measurements, to be subtracted from the observed gravity field. It is not possible to separate the GIA gravity signal from gravity observations using only seismic observations as the lithosphere seen by seismic measurements is still deflected due to the former ice load. In theory, the amount of bending of the lithosphere should be visible in the seismic observations, which itself would be a possible constraint on GIA models. Based on model set B, the maximum deflection could be expected to be as large as 217 meters. However, in observations of surface topography it is already difficult to observe this amount of bending. The Gulf of Bothnia is lower than its surroundings, but the east-west dimension of the Gulf of Bothnia is much smaller than the predicted wavelength from GIA modeling. The bending of the lithosphere could also be visible at the Moho. However, the current accuracy of the Moho depth determination is up to 5 km (*Grad et al.*, 2009), which causes the GIA deflection to fall within the uncertainty of the observations.

Therefore, the following section will discuss two different approaches to separate the GIA gravity signal from the observed gravity field. First, it is separated using filtering of the spherical harmonic coefficient representation of the gravity field. This idea is based on the belief that GIA can be isolated from other gravity signals based on wavelength separation. The second section (4.2) will assume isostatic compensation of crustal densities determined from seismic measurements to isolate the GIA gravity signal, which is a non-isostatic effect. This will prove to be unsuccessful due to inaccurate knowledge of crustal and upper mantle structures. Therefore, the last two sections discuss the second research question, to quantify the effects of the GIA correction in geophysical modeling. Section 4.3 will show the effect in a regional crustal model using the remaining uplift estimate and Section 4.4 shows the GIA gravity correction on gravity anomalies and its effect on interpretation of the gravity anomaly.

4.1   Separating GIA gravity signal using spherical harmonic coefficients truncation

Some studies (e.g., *Sjöberg et al.* (1994)) have separated the GIA signal from other gravity anomaly sources by filtering the spherical harmonic series. For example, *Sjöberg and Bagherbandi* (2013) use the geoid signal in the spherical harmonic domain of degree and order 10-70 (12 m peak value) to constrain remaining uplift in Fennoscandia to 80 m. The idea behind this band-pass filtering of the spherical harmonic coefficients is to eliminate short and long wavelength sources from the observed gravity field, which are believed to contain non-GIA sources such as mantle convection and high-resolution topography.

In Figure 3.9, the degree variance of the gravity field of the Earth is plotted together with a mantle convection model (*Tosi*, 2007) and the GIA gravity signal. The degree
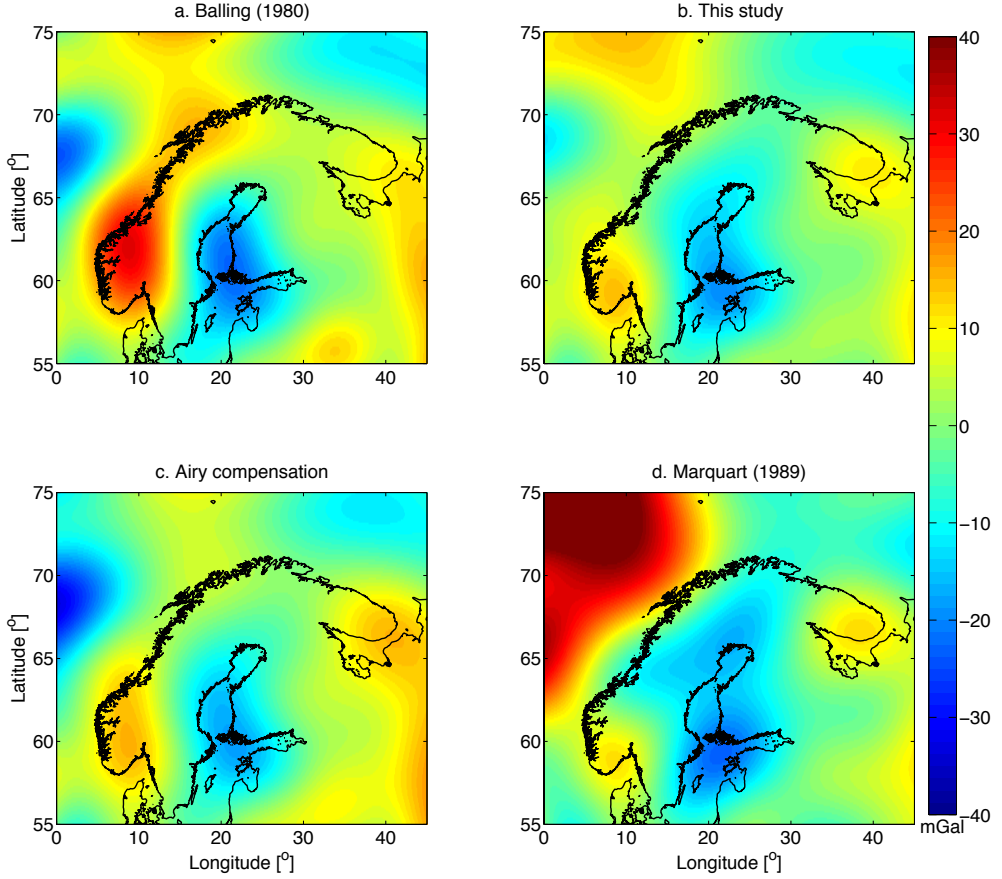
Figure 3.10: Isostatic gravity anomalies constructed by four different methods: a) the statistical method of *Balling* (1980). b) a local compensation scheme which puts the compensating masses in the upper mantle. c) Airy compensation. d) Pratt compensation (*Marquart*, 1989)

variance is defined in the following way (*Rapp*, 1982):

$$V_l^2 = \sum_{m=0}^{l} (C_{lm}^2 + S_{lm}^2) \qquad (3.3)$$

The normalized spherical harmonic coefficients are represented by C_{lm}^2 and S_{lm}^2, with degree l and order m. It can be seen that both the convection model as well as the GIA model have most of their energy in the first 30 spherical harmonic degrees. Furthermore, a gravity model of the top 100 km of the Earth is included in Figure 3.9 based on the topography and crustal masses of CRUST1.0, which are compensated by a local isostasy scheme where the density of the mantle is changed to obtain isostatic equilibrium. The spectrum of the GIA signal overlaps with that of the crustal and topographical masses
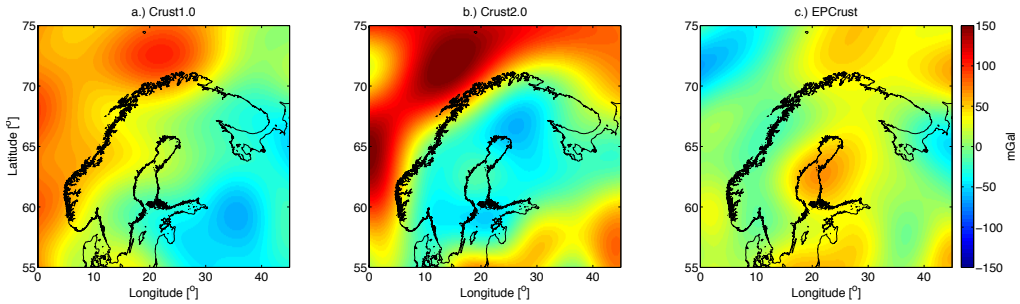
Figure 3.11: Isostatic gravity anomalies of Fennoscandia where the crustal structures are compensated by density differences in the mantle for different crustal models: a.) CRUST1.0 b.) CRUST2.0 c.) EPCrust. The compensation depth is 300km.

for the higher degree spherical harmonic coefficients. Both results show that it is not possible to separate the GIA gravity signal simply by applying a band-pass filter in the spherical harmonic domain, since it overlaps with the signal of mantle convection and crustal masses.

This can be seen in more detail by looking at the effect of the choice of truncation limits. After inspecting the gravity signal of the GIA model results, we conclude that the spherical harmonic domain of degree and order 4-45 contains most of the Fennoscandian GIA signal. Adding coefficients with lower or higher degree and order will change the modeled GIA gravity anomaly by not more than 1 mGal. However, other studies state a spherical harmonic domain of 10 to 70 degree and order (*Bjerhammar et al.*, 1980). For example, the estimated -12 m geoid in *Sjöberg and Bagherbandi* (2013) changes as a function of lower degree boundary. For the domain 5-70, the peak geoid undulation is -20 m, domain 8-70 gives -15 m and 11-70 results in -8 m. This quick investigation shows that any lower degree truncation includes a signal from mantle convection or removes the GIA signal of interest. Therefore, we conclude that these low degree signals must be taken into account when studying the GIA effect in the static gravity field.

4.2   Separating GIA gravity signal using isostasy

Section 3 showed that GIA gravity signal cannot be separated using solely geometric models of the crust because GIA is superimposed in the current observed crustal geometry. Also, the GIA gravity signal cannot be separated by using only spherical harmonic band filtering. Therefore, a different approach is needed to separate the GIA gravity signal from the observations. Since GIA is a non-isostatic effect, this section studies if it is possible to separate the signal from isostatic gravity effects.

The isostatic anomalies are constructed by compensating known masses, which can be topography or crustal structures such that the total mass up to the compensation depth is equal for all locations. Both cases are discussed in the following. First, four different methods from literature are used to generate different topographic isostatic anomalies, where topographic masses are compensated in four different ways. The spread between the models gives information about the uncertainty in the isostatic anomaly introduced
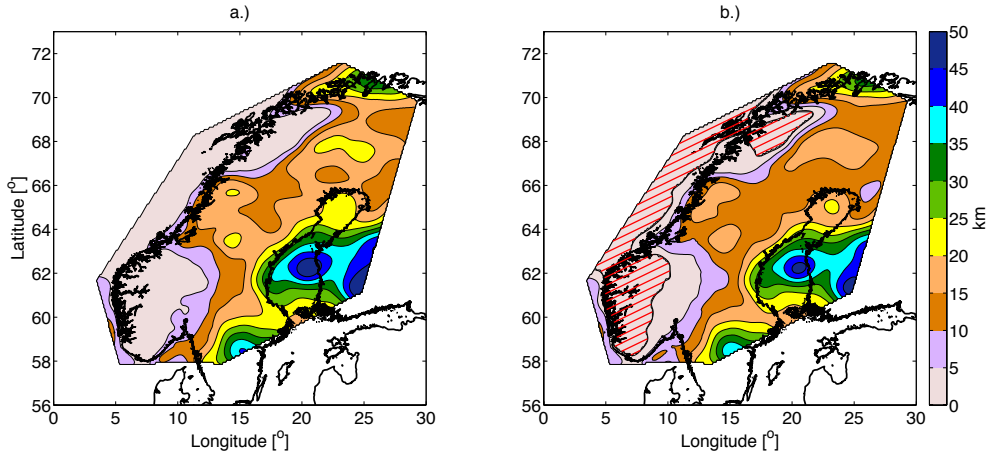
Figure 3.12: The LCB thickness in Fennoscandia from *Ebbing* (2007a) a.) uncorrected and b.) corrected for GIA effect. The red hatched area represents the location of a negative LCB thickness due to the GIA correction.

by the choice of compensation method. The methods are a.) a statistical technique, which assumes a linear regression between the topography and the gravity anomaly (*Balling*, 1980), b.) a local isostatic compensation scheme, where the compensating masses for the topography are modeled by density anomalies in the upper mantle defined by the CRUST1.0 Moho and a lower boundary of 100 km depth, c.) Airy compensation ($T = 30$ km and a density contrast of 650 kg/m^3), and d.) Pratt compensation using the geoid undulation (*Marquart*, 1989). The computed isostatic geoid undulation of this last method is converted into a gravity anomaly for a consistent comparison. The isostatic anomalies are computed with the global gravity field model GOCO03S (*Mayer-Gürr et al.*, 2011) and topography from the ETOPO2v2 model. Figure 3.10 shows the isostatic anomaly constructed by the four methods. Some local differences are visible, but the overall correlation is high. The observed negative anomaly at the the center of the Gulf of Bothnia is between -14 mGal and -20 mGal, but the largest negative anomaly is located south of the Åsland Islands. The standard deviation of these different solutions is between 5 and 10 mGal in the area of the Fennoscandian post-glacial uplift. The uncertainty in the choice of compensation is small enough that the GIA gravity signals from different models can be distinguished. However, this kind of compensation neglects the fact that crustal structures should also be compensated.

To compensate the crust, a similar approach is followed as the compensation of the topography, shown in Figure 3.10b. Every mass column is given a total mass given by a reference crust of 27 km thickness and a density of 2800 kg/m^3 and a mantle density of 3420 kg/m^3. Anomalous masses in the crust are corrected by changing the density in the upper mantle of the model. The forward modeled gravity field of this model is subtracted from the gravity observation, resulting in a crustal isostatic gravity anomaly that consists of non-isostatic effects.

To see the magnitude of the uncertainty introduced by unknown crustal structure,

three crustal density models based on seismic data are employed here: the global CRUST2.0 (*Bassin et al.*, 2000), the improved CRUST1.0 (*Laske et al.*, 2013) and the regional model EPCrust (*Molinari and Morelli*, 2011). The area outside EPCrust is filled in by CRUST2.0 such that it can be used as a global model in the forward modeling scheme. The density models are forward modeled up to degree and order 45 in spherical harmonic coefficients as beyond degree 45 there is little GIA signal (section 4.1). The resulting isostatic gravity anomalies are shown in Figure 3.11. In all three models, a different anomaly is seen in the region of expected maximum GIA uplift. The CRUST2.0 result shows a large low gravity anomaly where the Baltic craton is expected whereas EPCrust shows some correlation with the Moho geometry from *Grad et al.* (2009), which is used in the construction of EPCrust. CRUST1.0 shows a long wavelength east-west gradient in the anomaly. The variation of the anomaly in the area of maximum uplift ranges from -50 to 60 mGal in between the three crustal models. A spread of 110 mGal is well above the uncertainty in the GIA models, and therefore it will not be possible to select between competing GIA models such as model set A or model set B. This illustrates that the uncertainty in density models of the crust and associated compensation in the upper mantle is still too large to extract the GIA gravity signal from the gravity observations even without consideration of the mantle convection signal.

4.3   Correcting crustal models for the deflection due to GIA

This section will investigate research question (ii), what effect does the correction for GIA have on crustal density interpretations. An earlier study already showed the significance of correcting for GIA (*McKenzie*, 2010). To quantify this effect, the study of *Ebbing* (2007a) is chosen as example. In this model, the assumption of equal mass columns is made to constrain the thickness of a high density lower crustal body (LCB) located at the bottom of the crust. If the GIA signal is not taken into account, the crustal masses are overcompensated in the areas where ongoing post-glacial rebound is present, as explained in the previous part. This overcompensation results in a too large thickness of the LCB. The thickness of the LCB is obtained by setting the mass of every column equal to that of a reference mass column, as stated in *Ebbing* (2007a):

$$\rho_{topo}D_{topo} + \sum_{i=1}^{3} \rho_{c,i}D_{c,i} + \rho_{LCB}D_{LCB} + \rho_{mantle}D_{mantle} + \rho_{asth}D_{asth} = \sum_{i=1}^{5} \rho_{ref,i}D_{ref,i}$$

(3.4)

Here, D is the thickness of the layer, given in the subscript, and ρ is the density of that layer. The density model consists of a topographic layer, three crustal layers plus the LCB, the upper mantle lithosphere and the asthenosphere. The reference model used by *Ebbing* (2007a) consists of 5 layers. He deduced the density of those layers from crustal observations in the coastal areas ($h_{topo} \approx 0$) around Fennoscandia.

Correcting for the remaining GIA uplift can be done by introducing the GIA deflection to all the crustal layers in the model of *Ebbing* (2007a). As a result of this correction, extra asthenosphere mass per column is introduced. The amount of extra mass is location dependent and described by the shape of the GIA deflection. Equation (3.4) has to be changed to account for additional mass that simulates the non-isostatic

effect of GIA. This is done by introducing an extra layer of mass ($\rho_{asth}D_{GIA}$) in the density model. The relation becomes,

$$\rho_{topo}D_{topo} + \sum_{i=1}^{3} \rho_{c,i}D_{c,i}^{new} + \rho_{LCB}D_{LCB}^{new} + \rho_{mantle}D_{mantle} + \rho_{asth}D_{asth} + \rho_{asth}D_{GIA}$$

$$= \sum_{i=1}^{5} \rho_{ref,i}D_{ref,i} \quad (3.5)$$

To find the new thickness of the LCB layer, equation (3.4) is subtracted from (3.5), resulting in:

$$(\rho_{c3}D_{c3}^{new} + \rho_{LCB}D_{LCB}^{new}) - (\rho_{c3}D_{c3}^{old} + \rho_{LCB}D_{LCB}^{old}) + \rho_{asth}D_{GIA} = 0 \quad (3.6)$$

All layers keep the same thickness except the LCB and the lower crust. The sum of thicknesses of the third crustal layer and the LCB is chosen equal for both the old model and the new model. This means only the upper bound of the LCB is changed. The relation for the new LCB thickness can be found:

$$D_{LCB}^{new} = D_{LCB}^{old} - \frac{\rho_{asth}}{\rho_{LCB} - \rho_{c3}} D_{GIA} \quad (3.7)$$

Thus, the geometry of the new LCB depends on the amount of GIA displacement remaining and the densities of the three layers. The new LCB thickness depends largely on the difference in density of the LCB and lower crustal layer. If these densities are close the LCB becomes even thinner.

For the correction we use the GIA model with maximum deflection to show the largest effect. This model with viscosity structure of $\nu_{um} = 16 \times 10^{20}$ Pas and $\nu_{lm} = 256 \times 10^{20}$ Pas has a maximum deflection of 217 m. Correcting the density model with this GIA model according to equation (3.7) results in a reduction of the thickness of the LCB of 3.2 km using the density values of *Ebbing* (2007a). This is 6.4 percent of the total thickness of the LCB layer, which is small, but can be considered to be within the resolution of seismic measurements. Forward modeling the new density model with the corrected LCB produces a decreased gravity anomaly due to the smaller LCB layer compared with the initial model, by a value of 30 mGal. This roughly agrees with the GIA gravity signal caused by the subsided lithosphere.

Figure 3.12 shows the differences between the uncorrected and corrected LCB thickness in the Fennoscandian area. The shape is similar, but there are some subtle changes. Around the Gulf of Bothnia the changes are largest, corresponding to the location of maximum uplift. The large LCB thickness in west and mid Finland is still present, but the GIA correction has reduced the variation of the LCB thickness in other regions. Overall, the GIA correction does not alter the conclusions made by *Ebbing* (2007a). Still, we suggest to apply a correction with the best fitting GIA model, because the uncertainty in the GIA model is small enough that crustal density estimates can be improved.
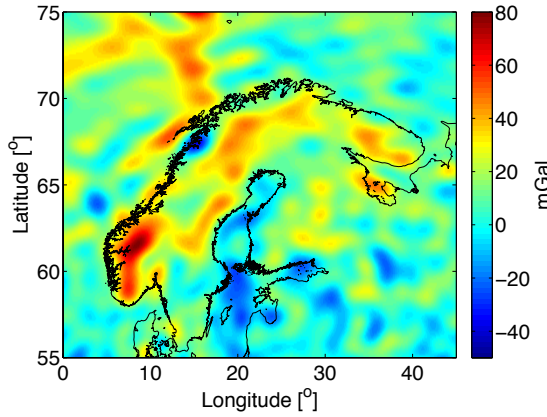
Figure 3.13: The free-air anomaly in Fennoscandia corrected for the GIA gravity signal using a GIA model of model set B ($\nu_{um} = 16 \times 10^{20}$ Pas and $\nu_{lm} = 256 \times 10^{20}$ Pas).

4.4   Correcting observed gravity anomalies for the gravity anomaly due to GIA

In the previous section, the effect of correcting for the remaining uplift was studied. Gravity anomalies in Scandinavia can also be corrected for GIA, in which case the corrected gravity anomaly represents the future gravity field, when the lithosphere has fully relaxed from the melting of the ice sheet. Studies that use gravity data, together with the assumption of isostatic equilibrium to constrain density structures, mistakenly compensate the deflected lithosphere due to GIA by increasing mass below the lithosphere. Section 3 showed the GIA gravity signal induced by the deflection of the lithosphere. The observed free-air gravity anomaly can be corrected for this GIA gravity signal in the following way:

$$g_{corrected,FA} = g_{FA} - \Delta g_{GIA} \tag{3.8}$$

The GIA gravity signal, Δg_{GIA}, can be calculated from GIA modeling or by using the GIA deflection according to equation (3.2), g_{FA} is the observed free-air anomaly from GOCO03S (*Mayer-Gürr et al.*, 2011) seen in Figure 3.1. Figure 3.13 shows the free-air anomaly after correcting for the GIA effect. The large negative (blue) anomaly disappears after the GIA correction, which indicates that it is mainly caused by post-glacial rebound. The positive gravity anomalies in the South Scandes are slightly enhanced, which reduces the need for a thick crustal root to support the mountains in order to match the observed, GIA corrected, gravity anomaly. It should be stressed that this correction only makes sense when the assumption of isostatic equilibrium is made in the modeling approach.

The Bouguer anomaly can also be corrected for the GIA gravity effect; however, the topography that should be used is that of the fully relaxed topography. The GIA corrected Bouguer anomaly becomes

$$\Delta g_{corrected,B} = \Delta g_{corrected,FA} - 2\pi G \rho_c h_{corrected} \tag{3.9}$$
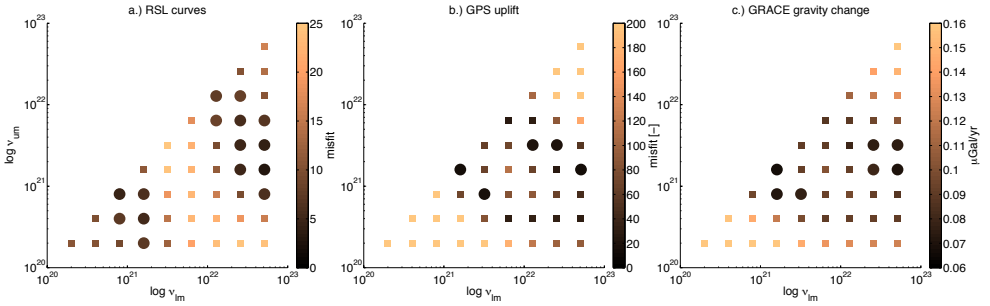
Figure 3.14: a.) Misfit with respect to relative sea level data (RSL) of *Tushingham and Peltier* (1992) in Fennoscandia for the GIA model using a pre-cycle ice loading and a lithosphere thicknesses of 150 km b.) Similar, but for GPS uplift rates c.) The standard derivation deviation of the difference between the models and the GRACE gravity change observations.

with $h_{corrected} = h_{obs} - h_{GIAdeflection}$, where the GIA deflection is obtained from GIA modeling. The corrected Bouguer anomaly is close to the uncorrected Bouguer anomaly, because GIA is removed in both the gravity signal and the topography. Most of the GIA signal is situated in the displacement of topography, as discussed in Section 3.

5   Conclusions

The goal of this study was to answer two questions. First, can the GIA gravity effect be separated from the observed static gravity field? This question is answered by applying different techniques from the literature to isolate the GIA signal from the static gravity field.

The GIA gravity signal is generated by the deflection of the isostatic lithosphere, pushing away mantle material. From the layered lithosphere modeling, it is found that 74 percent of the GIA gravity signal is generated by the deflection of the topography. The remainder of the signal is due to the uplift of the remaining density contrasts in the crust.

Separating the GIA gravity effect by considering a particular bandwidth in the spherical harmonic domain is unsuccessful, due to the overlap in bandwidth of dynamic deep mantle anomalies, GIA and signals from the crust. Furthermore, separating the GIA gravity signal using models for the crust in combination with isostatic compensation in the mantle was investigated. Several different methods to achieve isostatic compensation have been pursued and it is shown that the uncertainty due to the compensation techniques is small (within 5-10 mGal). However, the uncertainty in crustal models based on seismic observations is still too large to separate GIA from density anomalies in the crust and upper mantle. It is concluded that, contrary to earlier findings, it is not possible to extract the GIA signal from the observed gravity field with sufficient accuracy to be useful as constraint in GIA modeling

Current GIA models have less uncertainty than the global and regional density mod-

els, such as CRUST2.0, CRUST1.0 and EPCrust, for gravity field modeling purposes. Therefore, it is suggested to correct gravity observations and models using the results from GIA modeling. Such a correction is necessary if the modeling assumes that all topography and crustal masses are isostatically compensated, as the deflections introduced by GIA are non-isostatic. Which brings us to the second research question: what is the effect of the GIA correction in geophysical models constrained by gravity?

A simple correction is done by superimposing the lithosphere deflection, obtained from GIA modeling, onto topography and density layers. The corrected density models have effects in geophysical modeling of the crust and lithosphere (up to 5-10 percent in thickness of lower crustal layer in the example study). Gravity observations can be corrected by using the simple relations in equations (3.2) and (3.8). It will be interesting to see if GIA models in other regions, such as North America and polar regions, are accurate enough to apply a GIA correction there.

Acknowledgments

A: Extra glacial period

As shown by *Johnston and Lambeck* (1999), *Kaufmann et al.* (2000), and *Kaufmann and Wu* (2002), adding another ice loading cycle affects estimates using RSL curves and other observables. Therefore, the used data sets, regional RSL curves, GPS uplift rates and GRACE gravity change, are compared with GIA models using two ice cycles to see if it affects the conclusions in this study. The extra ice loading cycle before ICE-5G is modeled with a linear growth rate beginning at 227 ka, obtaining a maximum at 135 ka, in height identical to the height at the glacial maximum modeled by ICE-5G. After the penultimate glacial maximum, melting occurs until zero ice mass is reached at the beginning of the ICE-5G ice model (122ka). No inter-glacial period is chosen, because literature is still relatively unclear about the length of this period (*Svendsen et al.*, 2004a),(*Penaud et al.*, 2008). Furthermore, neglecting an inter-glacial period will have the most effect on the state of the GIA models, because less relaxation is obtained prior to the last glacial cycle. The ice loading history is used in the GIA modeling using similar settings as in section 2.

The resulting misfit plots are shown in Figure 3.14 for a lithosphere thickness of 150 km. The comparisons of the models with other lithosphere thicknesses give similar deviations and result in similar selection of viscosity profiles. Overall, the introduction of the extra ice loading cycle does not significantly change the RSL, GPS uplift and
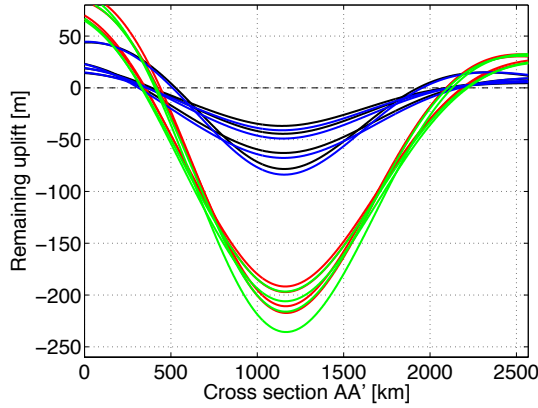
Figure 3.15: Modeled remaining uplift for the different GIA models. Black and red lines represent model A and B using only ICE-5G for ice loading history. The models using an extra ice loading cycle are shown in blue (model set A) and green (model set B) lines.

GRACE gravity change, compared to the results in Figures 3.3, 3.4, and 3.5. When inspecting Figure 3.14 in more detail, it can be noticed that there are small changes in the misfit plots. These changes, however, do not change the conclusions for selecting the GIA models, A and B.

The effect of the extra ice cycle is also inspected for the modeled remaining uplift. Figure 3.15 shows the similar cross-section as in Figure 3.6 of model set A and B. The black (model set A) and red (model set B) lines are the results obtained using only ICE-5G. The results using an extra ice loading cycle are included in blue for model set A and green for model set B. For model A an extra deflection of 6 meter is observed at maximum deflection, which is around 5 percent of the total value. Model B shows a bit more variation, especially the GIA model with upper mantle and lower mantle viscosity of 32×10^{20} Pas and 512×10^{20} Pas, respectively. The larger viscosity shows more sensitivity to earlier ice loading changes, whereas low viscosity does not "remember" these loads. With the exception of the mentioned model, the differences are small and similar to model set A. The mentioned GIA model has a difference of 18 meter, which is 7.8 percent of its total maximum deflection. Inspecting the gravity field differences give similar results, within 10 percent of the deflection value. It can be concluded that previous ice loading cycles have a small effect on the Fennoscandian GIA modeling done in this study. Nevertheless, for more accurate GIA modeling, extra ice loading histories should be modeled.

B: Data used

This section presents the RSL data used in the GIA modelling. The RSL curves are a selection from the dataset of *Tushingham and Peltier* (1992). Only sites in Fennoscandia are used and for which a long time series is available. This results in 15 sites with the
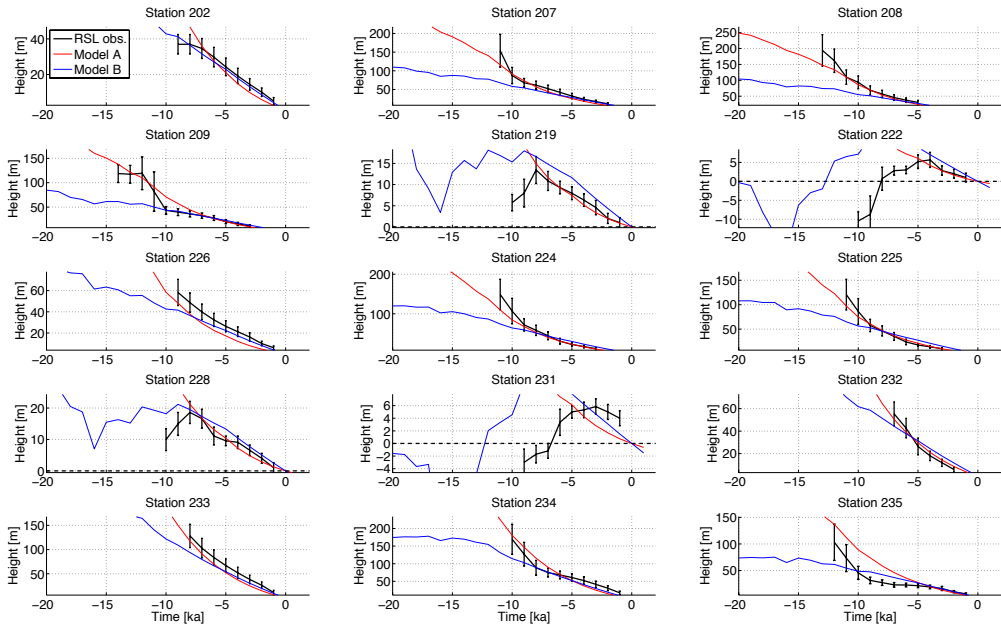
Figure 3.16: The 15 RSL curves from *Tushingham and Peltier* (1992) with two best-fit results from GIA modelling, Model A (red) and Model B (blue).

locations shown in Figure 3.2a. The data with its spatial and time error estimates are plotted in Figure 3.16 together with RSL predictions from the two best fitting GIA models from the discussed model set A and B.

Paper III - Comparing gravity-based to tomography-derived lithosphere densities: a case study of the British Isles and surrounding areas

"Up to the Twentieth Century, reality was everything humans could touch, smell, see, and hear. Since the initial publication of the chart of the electromagnetic spectrum, humans have learned that what they can touch, smell, see, and hear is less than one-millionth of reality."

– R. Buckminster Fuller, *R. Buckminster Fuller on Education (University of Massachusetts Press, 1979, p.130)*

Comparing gravity-based to tomography-derived lithosphere densities: a case study of the British Isles and surrounding areas

B.C. Root[a], *J. Ebbing*[b], *W. van der Wal*[a], *R. England*[c], *and L.L.A.Vermeersen*[a,d]

Abstract Lithospheric density structure can be constructed from seismic tomography, gravity modelling, or studies using both data sets. The different approaches have their own uncertainties and limitations. This study aims to characterise and quantify some of the uncertainties in gravity modelling of lithosphere densities. To evaluate the gravity modelling we compare gravity-based and seismic velocity-based approaches to estimating lithosphere densities.

In this study, we use a crustal model together with lithospheric isostasy and gravity field observations to estimate lithosphere densities. To quantify the effect of uncertainty in the crustal model, three models are implemented in this study: CRUST1.0, EuCrust-07, and a high resolution P-wave velocity model of the British Isles and surrounding areas. Different P-wave velocity-to-density conversions are used to study the uncertainty in these conversion methods. The crustal density models are forward modelled into gravity field quantities using a method that is able to produce spherical harmonic coefficients. Deep mantle signal is assumed to be removed by removing spherical harmonic coefficients of degree 0-10 in the observed gravity field. The uncertainty in the resulting lithosphere densities due to the different crustal models is ± 110 kg/m^3, which is the largest uncertainty in gravity modelling. Other sources of uncertainty, such as the V$_P$ to density conversion (± 10 kg/m^3), long-wavelength truncation (± 5 kg/m^3), choice of reference model ($< \pm 20$ kg/m^3), and Lithosphere Asthenosphere Boundary uncertainty (± 30 kg/m^3), proved to be of lesser importance.

The resulting lithosphere density solutions are compared to density models based on a shear wave velocity model (*Schaeffer and Lebedev*, 2013). The comparison shows that the gravity-based models have an increased lateral resolution compared to the tomographic solutions. However, the density anomalies of the gravity-based models are three times higher. This is mainly due to the high resolution in the gravity field. To account for this, the gravity-based density models are filtered with a spatial Gaussian filter with 200 km halfwidth, which results in similar density estimates (± 35 kg/m^3) with the tomographic approach. Lastly, the gravity-based density is used to estimate laterally varying conversion factors, which correlate with major tectonic regions. The independent gravity-based solutions could help in identifying different compositional domains in the lithosphere, when compared to the tomographic solutions.

(a): Delft University of Technology, The Netherlands
(b): University of Kiel, Kiel, Germany
(c): University of Leicester, United Kingdom
(d): NIOZ in Yerseke, The Netherlands

keywords: British Isles, crustal P-wave velocity model, gravity field, lithosphere density

1   Introduction

There is abundant evidence that the lithosphere is highly heterogeneous (*Kaban et al.*,
2016; *Griffin et al.*, 2009; *Afonso et al.*, 2008; *Jordan*, 1975). Variations in temperature
and composition at lithospheric depths result in laterally varying shear-wave velocity
and density anomalies (*Khan et al.*, 2015). Thus, temperature and composition can
be studied by using seismic observations (*Afonso et al.*, 2016a) and gravity modelling
(*Herceg et al.*, 2016; *Kaban et al.*, 2004) or in joint-inversion studies combining both
techniques (*Khan et al.*, 2015; *Cammarano et al.*, 2011; *Simmons et al.*, 2010; *Deschamps
et al.*, 2001; *Forte et al.*, 1994). However, all these studies have their limitations, which
result in uncertainties in the final model of the lithosphere (*Foulger et al.*, 2013).

Several V_S models are available for the upper mantle, e.g. *Schaeffer and Lebedev*
(2013); *Debayle and Ricard* (2012); *Ritsema et al.* (2011); *Schivardi and Morelli* (2011).
The velocity anomalies are caused by temperature, density, and composition changes in
the upper mantle (*Jordan*, 1978) and point to a complex structure in the lithosphere.
There are other causes as well, e.g. anisotropy due to crystal structure or pre-stress
anisotropy, but the effect of temperature is believed to be the most important (*Forte*,
2007). One of the drawbacks of passive seismic experiments, like delay time analysis,
receiver functions, and travel-time tomography, is the uneven distribution of the seismic
events and receiver stations. Areas without any data or sparse data coverage need in-
terpolation and results in large uncertainties. A second drawback is that some of these
techniques need an *a-priori* crustal model to account for the corresponding travel-time
corrections (*Schaeffer and Lebedev*, 2013). Unmodelled crustal effects introduce errors
in the lithosphere region (*Lekić and Romanowicz*, 2011; *Schaeffer and Lebedev*, 2013).
Furthermore, the 3D structure of the wave-speed anomalies is difficult to determine be-
cause of the smearing problem along the ray bundles (*Foulger et al.*, 2013). Moreover,
the wave velocities are not uniquely related to parameters like temperature, or composi-
tion. The wave velocities are related to elastic parameters (*Artemieva*, 2001), which are
influenced by temperature and composition. The relations between elastic parameters,
temperature, and composition are determined in the laboratory and have their own un-
certainties (*Cammarano et al.*, 2011). Finally, shear wave observations are found to be
insensitive to density variations (*Khan et al.*, 2015). A detailed review of tomographic
imaging is given in *Foulger et al.* (2013), the uncertainty in the V_S models proves to be
difficult to quantify.

Lithospheric structures can also be explored by using the gravity field (*e.g. Herceg
et al.* (2016); *Root et al.* (2015); *Kaban et al.* (2004)). However, due to the intrinsic non-
uniqueness of gravity modelling the solutions need to be constrained, which introduces
uncertainties in the final model. First, the long wavelength features in the gravity field
are assumed to be from the deep mantle (below 300 km) or even core-mantle boundary
effects (*Forte et al.*, 1993). Usually, these features are removed by removing low-degree
spherical harmonic coefficients from the gravity field observations. For example, the
regional study of *Herceg et al.* (2016) used a truncation limit of degree and order 10 in
agreement with *Bowin* (2000, 1991). This particular truncation corresponds to removing
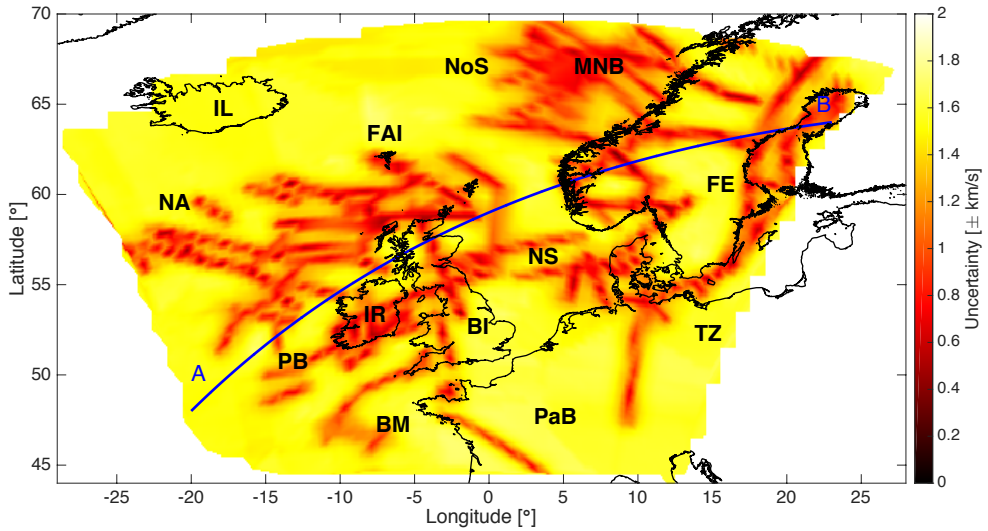
Figure 4.1: Depth-average of the uncertainty in the P-wave velocity model. The blue line denotes a cross section AB that is shown in Figure 4.2. Several locations that are used: BI British Isles, BM Biscay Margin, FE Fennoscandian craton, FAI Faroe Islands, IL Iceland, IR Ireland, MNB Mid-Norwegian Basin, NA North Atlantic ocean, NoS Norwegian Sea, NS North Sea, PaB Paris Basin, PB Porcupine Basin, and TZ Tornquist Zone.

signals with wavelengths larger than 2000 km. Second, the gravity signal of the crust needs to be removed from the observations (*Kaban et al.*, 2004) to reveal the lithosphere. Errors in the used crustal model lead to uncertainty in the lithosphere solutions (*Root et al.*, 2015; *Kaban et al.*, 2004; *Panasyuk and Hager*, 2000). For example, the global crustal model CRUST1.0 (*Laske et al.*, 2013) suffers from lack of data in large parts of the world.

Regional crustal structures can also be observed by high-resolution seismic observations, like wide-angle seismic data in the form of P-wave velocity (Vp) models, and can be converted to density profiles (*e.g.* (*Artemieva and Thybo*, 2013; *Kelly et al.*, 2007; *Tesauro et al.*, 2008)). A high-resolution V_P model of the British isles and surrounding areas was presented by *Kelly et al.* (2007), together with uncertainty estimates of the seismic observations. This regional Vp model is used in the present study to study the effect of increased radial resolution in crustal models. The high resolution observations in these models reduce the uncertainty in crustal structure compared to global models and should therefore result in improved lithosphere models.

Finally, many joint studies using seismic models and gravity observations have been performed. After a joint study of seismic wave velocities and gravity observation, *Forte et al.* (1994) found that the mantle heterogeneities from seismic observations fit the long wavelengths of the potential field, but have a large mismatch to the free-air anomalies. Others estimated the scaling factor between shear wave and density (*Deschamps et al.*,
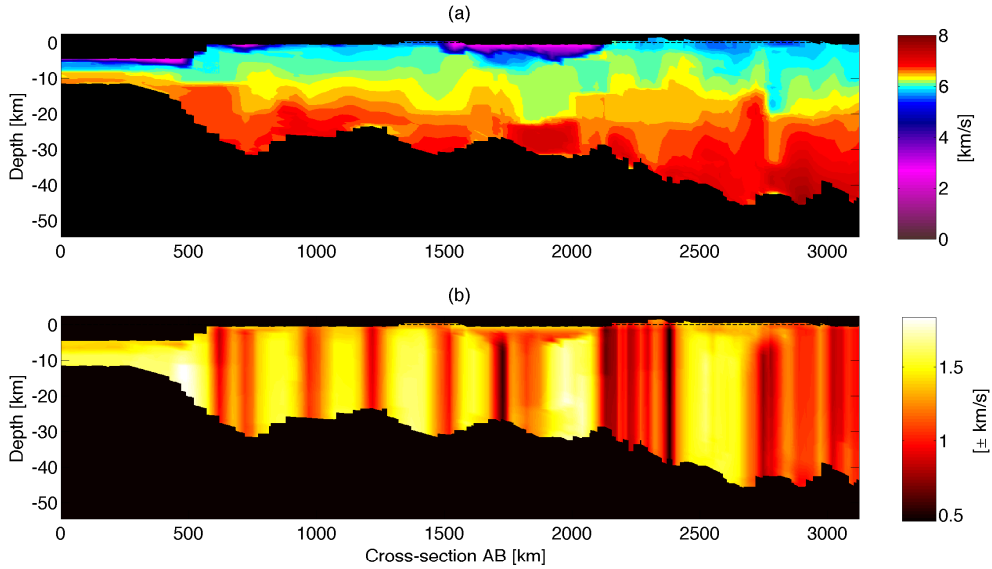
**Figure 4.2: Cross-section AB (see Fig. 4.1) through the regional Vp crustal model of
Kelly et al. (2007) with (a) the V$_P$ values and (b) the uncertainty of the P-wave velocity.**

2001). They also found that the geoid between spherical harmonics coefficients 11-16
is most sensitive to lithosphere anomalies. More sophisticated models have been devel-
oped, where seismic wave observations were combined with gravity data, plate motions,
dynamic topography and mineral physics such as the GYPSUM model (*Simmons et al.*,
2010). *Cammarano et al.* (2011) found that by inserting a petrological lithosphere, the
fit to geoid and topography data improved. Moreover, they introduced lateral compo-
sitional variations in the lithosphere did not change the thermal interpretation of the
seismic models significantly, which shows that the seismic waves have different sensitiv-
ities to the fundamental parameters of temperature and composition. Another study
proposed to include electrical conductivity in the joint lithosphere studies, due to its
different sensitivity to temperature and composition (*Khan et al.*, 2015). The most
advanced joint inversion studies are characterising the thermochemical structure of the
lithosphere using seismic data, gravity observations, and surface heat flow, together with
geochemical information of the rock composition (*Afonso et al.*, 2013a,b, 2016b).

In this study, we focus on the exploration of lithospheric density structures using
mainly the gravity field to fully understand the possibilities and limitations of this ob-
servation. We examine the uncertainty of the gravity-based density modelling of the
lithosphere. In order to do this, we propose a new gravity modelling approach to esti-
mate lithosphere densities. This methodology makes use of a crustal model, lithosphere
isostasy, and gravity field observations. Constraints needed in the modelling such as the
crustal model, truncation of the gravity data, and Lithosphere Asthenosphere Boundary
(LAB) model introduce uncertainties in the final lithosphere densities. We will quan-

tify these uncertainties for the different constraints. After this, the question arises of how a gravity-based lithosphere compares to a seismic-derived lithosphere? The seismic tomography models have their own uncertainties and drawbacks. Especially, the sensitivity of Vs tomography to density is limited. Nevertheless, the comparison between the two approaches is useful as a first step to see if a meaningful lithospheric density model can be derived from a purely gravity based model

In the first section, uncertainties due to the crustal model will be quantified. The crustal models use different Vp observations, different Vp to density conversion relations, and different radial resolution. Section 2 discusses the different crustal models that are used in this study. Secondly, the effect of the long wavelength truncation of the gravity field and its effect on the estimation of the lithospheric densities is examined. Moreover, we look at the uncertainties introduced by selecting a LAB model and an isostatic reference model. Section 5 shows the resulting lithospheric densities of the different models and their fit to the gravity fields. Finally, we discuss the differences between gravity-based and tomography-based lithosphere densities.

2   Crust models

The region of the British Isles and surrounding areas is well covered by seismic profiles and contains oceanic crust, continental margin, elevated continental crust, and cratonic crust. This makes it a good region to explore differences in gravity-based lithosphere densities due to crustal model uncertainties and evaluate the proposed methodology for different tectonic regions. The impact on the final lithosphere model of the different crustal models is examined. Also uncertainties due to the Vp to density conversion discussed in Section 2.2 are studied.

To investigate the error introduced by the uncertainty in crustal models, three crustal models are used in this study. Model A is the global representation of the crust by CRUST1.0 (*Laske et al.*, 2013). The seismic observations are converted to density by using conversions for sedimentary rock (*Gardner et al.*, 1974) and the *Christensen and Mooney* (1995) conversions (CM95) for depth dependent crustal rock. Model B will use the regional crustal model EuCrust-07 (*Tesauro et al.*, 2008), which consists of one sedimentary layer and two crystalline-crust layers. The model covers the area between 35°N-71°N, 25°W-35°E. Model C is constructed from a regional Vp model of the British Isles and surrounding areas (*Kelly et al.*, 2007). The implementation of this model is discussed in Section 2.1. It has a high resolution representation of the crustal masses, especially in the radial direction, compared to model A and B. Model B has used similar data for the area as model C. This makes it possible to study the effect of increased radial resolution in a crustal model. For both regional models, the crustal masses outside the study area are complemented by the CRUST1.0 model (*Laske et al.*, 2013) and interpolated on a 0.5x0.5 arc-deg grid.

2.1   Regional Vp model (Model C)

The regional Vp model that is used to compare with CRUST1.0 in this study is an updated version of *Kelly et al.* (2007). The updates consist of the LISPB-Delta data,
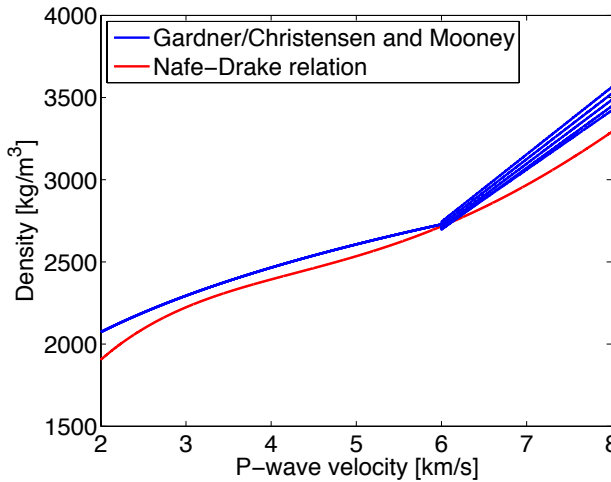
Figure 4.3: The relation between crustal density and P-wave velocity according to two studies. The red line shows the Nafe-Drake relationship (*Ludwig et al.*, 1970) and the blue line shows the Gardner rule for sedimentary rocks, complemented by empirical relations of *Christensen and Mooney* (1995) for crustal rocks, which are depth dependent.

which runs NNW-SSE across Wales and SW England and fills an important gap in observations of the crustal structure (*Maguire et al.*, 2011). Furthermore, new data is added in southern Scandinavia from the MAGNUS REX profiles (*Stratford et al.*, 2009; *DeGiorgio*, 2012). The model describes the crustal seismic velocity structure of the British Isles and surrounding areas and uncertainty in the velocity model (Figure 4.1). The seismic observations suffer from coupled uncertainties between velocity and depth of the interfaces (*Kelly et al.*, 2007) that makes it difficult to determine if the uncertainty is in the velocity distribution or the geometric boundaries. Nevertheless, it is constructed using 3D kriging designed from an analysis of variograms derived from the seismic data (for details see *Kelly et al.* (2007)). The advantage of this interpolation is that there is an error estimate of the P-wave velocity solution. The maximum depth of the model extends to around 60 km underneath the Fennoscandian craton. The radial density resolution is an improvement compared to the eight-layered CRUST1.0 crustal model and the three-layered EuCrust-07 model.

A cross-section of the model (Figure 4.2) shows the radial distribution of the P-wave velocity anomalies and their uncertainties. Sedimentary bodies are defined by velocities ranging between 2.27 - 5.0 km/s. Crustal velocities, close to the crust-mantle boundary, can go up to approximately 7.8 km/s. The uncertainty of the Vp model is more visible in the uncertainty map in Figure 4.1, where the locations of seismic profiles are easily identified. Locations with seismic observations have an uncertainty of ±0.5-0.8 km/s, whereas areas without observations have uncertainties of more than ±1.8 km/s around the mean velocity. Figure 4.2b shows no clear increase or decrease of uncertainty with increasing depth.

The topography is obtained from ETOPO1 (*Amante et al.*, 2009). The Moho bound-

ary is defined as the transition between crustal and upper mantle material at $V_P = 7.8$ km/s. The Moho is very deep in Fennoscandia (*Kinck et al.*, 1993; *Korsman et al.*, 1999) and becomes gradually shallower to the southwest. Away from the continental plateau the Moho is found to be at depths shallower than 20 km, where oceanic lithosphere can be found. In the Fennoscandian area all sedimentary material has been removed by recent glacial periods (*Steffen and Wu*, 2011). Also, Iceland is free of sediments, because it is relatively new land due to the diverging plate boundary. A number of prominent sedimentary basins are present in the study area (see Fig 4.1): the Porcupine Basin, the Biscay margin, the Rockall Through and the Mid-Norwegian Basin. These basins have depths to the basement of up to 10-12 km. In the Mid-Norwegian Basin area an improved structure of the sedimentary basins is expected, because many more seismic profiles were available in the regional model compared to CRUST1.0. The large-scale, but shallow, sedimentary basin northeast of Faroe Islands is not present in the sediment layer. This can be related to an absence of constraining data in the model in that region.

2.2 Transformation to density model

Averaged relations between crustal P-wave velocities and density are usually empirically determined (*Brocher*, 2005). We use two common relations to study the effect of the conversion uncertainty on the density modelling of the crust: the Nafe-Drake relation (*Ludwig et al.*, 1970) and the Gardner/CM95 relations (*Christensen and Mooney*, 1995). Figure 4.3 illustrates the two different relations between P-wave velocities and density. These relations are used in many modelling studies (*Tesauro et al.*, 2014; *Kaban et al.*, 2014; *Herceg et al.*, 2016).

First, the Nafe-Drake relation relates Vp observations to density for sedimentary and crustal rocks. A review of the Nafe-Drake relation is made by *Brocher* (2005), who reviewed the data and estimated a simple relation through all the data. Second, the Gardner/CM95 conversion uses the Gardner rule (*Gardner et al.*, 1974) for sedimentary rocks and the empirically determined relations of *Christensen and Mooney* (1995) for the crystalline-crustal rocks. *Zooback and Mooney* (2003) found a small error in *Christensen and Mooney* (1995). The *Christensen and Mooney* (1995) relations have different depth dependencies for crustal rocks, which is illustrated by the different lines in Figure 4.3. The two conversions have an overall similar shape. The main difference between the two relations is that the Nafe-Drake relationship produces a crust that has an overall lower density than the Gardner/Christensen-Mooney relation. This means that the crustal signal plays a slightly smaller role in the overall gravity signal of the complete lithosphere signal.

3 Lithosphere models

Here, we present a procedure to estimate the density distribution in the lithospheric part of the upper mantle by using gravity observations and a density model of the crust. First, lithospheric densities are computed by assuming isostatic equilibrium. This isostatic model is then used as a starting model for fitting lithosphere densities to the gravity field. This will produce the values for the lateral densities in the lithosphere.
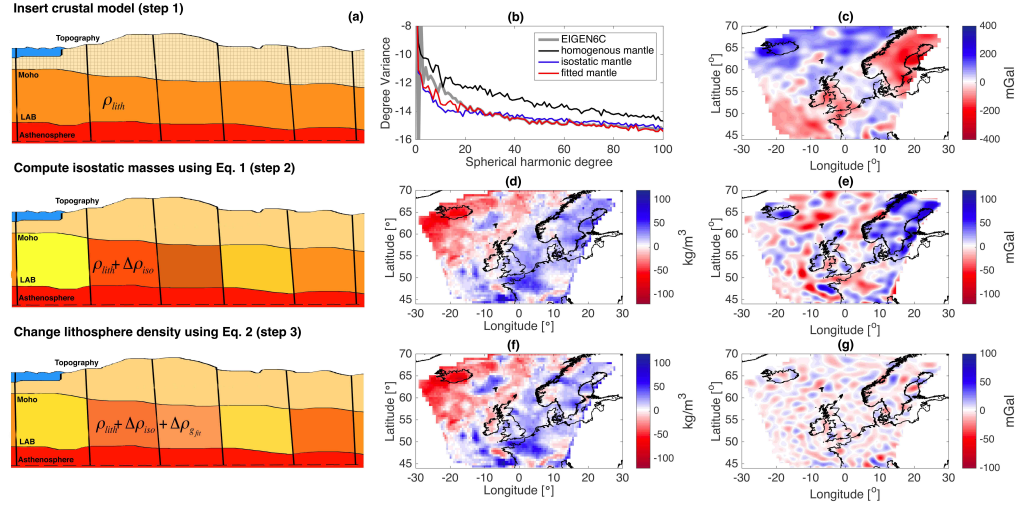
Figure 4.4: **(a) A sketch of how the gravity-based lithosphere model is constructed in three steps: first a crustal model is selected and complemented by a lithosphere and asthenosphere up to 300 km depth. Then lithospheric density anomalies are computed using lithosphere isostasy with equal pressure at 300 km(Eq. (4.1)). Finally, the lithospheric densities are changed such that the complete model is fitted to the gravity field. (b) the degree variance of the gravity fields of the observations and density models during the three steps. (d) and (f) the density maps of the lithosphere after step 2 and 3, respectively. (c) Gravity residual of EIGEN6C with the model at step 1. (e) Gravity residual of EIGEN6C with the model at step 2 (isostatic model). (c) Gravity residual of EIGEN6C with the model at step 3 (fitted model).**

Finally, we describe the procedure to obtain density anomalies from S-wave tomography models, such that they can be compared to the gravity-based solution. For a thorough discussion on the uncertainties in S-wave tomography we refer to *Foulger et al.* (2013) or *Afonso et al.* (2016a).

3.1   Gravity-based model of the lithosphere

In order to construct a lithosphere model both gravity field observations and the concept of isostasy are used. The construction of the lithosphere model is done in three steps (Figure 4.4a). First, a crustal model is chosen which is complemented by a reference mantle density (ρ_m) up to 300 km depth. The different crustal models are discussed in Section 2. Second, an *a priori* model of the lithosphere density anomalies ($\Delta\rho_{iso}$), assuming lithospheric isostasy (*Turcotte and Schubert*, 2014), is computed (see Figure 4.4d). In the third step, the model is completed by computing extra lateral density anomalies ($\Delta\rho_{g_{fit}}$) in the lithosphere (Fig 4.4f) needed to reduce the gravity residual of the model in line with the observed gravity. Figure 4.4b shows the improvement of the gravity field fit of the models to observations. With a homogeneous lithosphere, the degree variance of the gravity results is one order larger than the observed gravity field,

which results in residual gravity anomalies of ± 400 mGal (Fig 4.4c). When lithospheric isostasy is used the degree variance drops to the same order as the observed field, reducing the residuals to ± 100 mGal (Fig 4.4d). Step 3 reduces the residuals to ± 45 mGal, removing any correlation in the residual with geological structures (Fig 4.4g).

Crustal masses are assumed to be compensated in the upper mantle, which we define from now on as the lithosphere. These variations in the density structure are stable over a long timescale, because the lithosphere is not involved in mantle convection (*Jordan*, 1975). The lower boundary of this region is referred to as the Lithosphere Asthenosphere Boundary (LAB). The temperature at that boundary is estimated to be between 1250 and 1350 °Celsius, which represents the boundary between a conducting and convecting thermal regime (*Artemieva*, 2001, pp. 7). This corroborates our assumption that compensated masses are situated in the region between the LAB and the Moho. The compensation is shown to represent the global gravity observations well in most of the spectral domain (*Root et al.*, 2015). The separation between the lithosphere and asthenosphere is obtained from *Hamza and Vieira* (2012), which is based on global databases of heat flow (*Vieira and Hamza*, 2010) and crustal structure (*Laske et al.*, 2013). We deliberately choose not to use an LAB obtained from seismic tomography data to be independent from that data set.

To establish isostatic equilibrium, each mass column in the density model will be equal to the mass of a column of the reference model. The reference mass ($\rho_{ref}V_{lith}$) column consists of a 30 km thick crust with a density of 2850 kg/m^3 complemented by a mantle with a density of 3300 kg/m^3. These crustal thickness and density values are chosen after inspection of the CRUST1.0 model. The average crustal thickness and density in areas were the model has 0 ± 50 m topography are estimated to be around these values. The sensitivity of these chosen values and their effect on the final result will be presented in Section 5. The following relation for every mass column (i) can be set up:

$$
\begin{aligned}
\int_{300km}^{0km} \rho_{ref}\mathrm{d}V &= \int_{Moho}^{topo} \rho_{crust,i}\mathrm{d}V + \int_{LAB}^{Moho} \rho_{lith}\mathrm{d}V \\
&+ \int_{300km}^{LAB} \rho_{asth}\mathrm{d}V + \int_{LAB}^{Moho} \Delta\rho_i\mathrm{d}V
\end{aligned}
\tag{4.1}
$$

The mass of the crust will be determined by computing the spherical volume and multiplying it with the density from the converted P-wave velocity model or CRUST1.0. The mantle part of the model is constructed from the initial lithosphere (ρ_{lith}) with a density of 3330 kg/m^3 and is complemented by an asthenosphere up to 300 km deep using a homogeneous density of 3300 kg/m^3. The extra mass ($\Delta\rho_i$) needed to compensate the crust is calculated between the Moho and LAB, and added to the initial lithosphere density.

The isostatic model can be improved to better fit the observed gravity field. In step 3 of the gravity modelling, the lithosphere density is changed such that the complete density model better fits the gravity observations. Figure 4.5 illustrates the iterative process in a flow chart. It starts by computing the gravity field solution of the isostatic density model. This solution is compared with gravity model EIGEN6C (*Shako et al.*, 2014). It was found that the geoid (N) has the best convergence properties in this
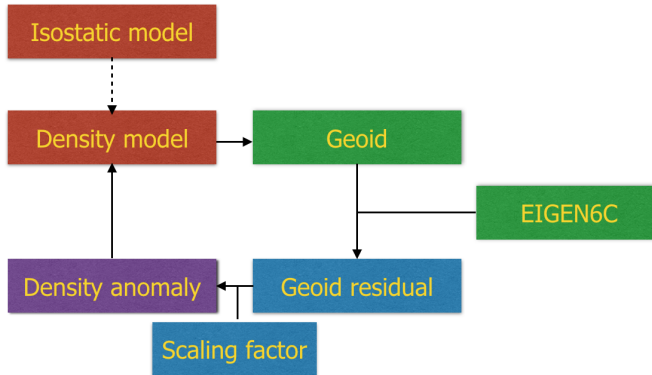
Figure 4.5: The iteration process starts with the a-priori isostatic model. Gravity field quantities of the density model are computed using the spectral forward modelling method described in *Root et al.* (2016). The geoid is compared with the EIGEN6C gravity model and a residual field is calculated. This residual is normalised and scaled to construct a density map that is added to the lithosphere density of the model to improve the fit to the gravity field. This process is repeated until convergence is obtained.

process, and that it is sensitive to lithospheric structures. The normalised geoid residual is used to calculate a density anomaly:

$$\Delta\rho_i = \sigma \frac{N_{EIGEN6C} - N_{model,i}}{|(N_{EIGEN6C} - N_{model,i})|_{max}} \tag{4.2}$$

This density anomaly, $\Delta\rho_i$, is added to the lithospheric density of the old model, to be used in the next iterative step (n). The scaling parameter, σ, ensures that the process converges within respectable time. This is repeated several times until the geoid residual between the modelled and observed field converges. Figure 4.4h shows the final results of the fitting process. Almost all of the density changes due to the gravity fitting process are smaller than ±25 kg/m^3 compared to the isostatic lithosphere model (step 2). This shows that lithospheric isostasy is a good first order approximation for the density distribution in the lithosphere.

3.2   Tomographic model of the lithosphere

In this study, the seismological density model of the lithosphere is based on SL2013sv (*Schaeffer and Lebedev*, 2013). To obtain the density of the lithosphere, the conversion factor from *Karato* (2008, p.373) is used to convert the lithospheric S-wave velocities to density values which can be compared to the gravity-based lithosphere structures of this study. The conversion factor is defined by the following relation:

$$\frac{\Delta\rho}{\rho} = p\frac{\Delta V_S}{V_S} \tag{4.3}$$

A constant conversion factor (p), or scaling factor, of around 0.2 is suitable for the lithospheric region (*Karato*, 2008, p. 377), this value is also approximately used by

other models (*Steinberger*, 2016). We assume that all S-wave anomalies are caused by thermal effects. The purpose of this study is not to determine the best estimates of mantle temperatures from seismic observations, but to study the differences between the two approaches.

With the estimated densities from gravity observations, we are able to determine a conversion factor (*Forte and Mitrovica*, 2001) that varies in lateral but not in radial direction. We compare these lateral variations in the conversion factor with tectonic settings of the area. Because the estimated density is an average density anomaly for the lithosphere, the V_S anomalies must be radially averaged before they are converted to density. Here, the lithosphere is defined by the same area between the Moho and the LAB used in the gravity modelling, ensuring that the same regions are compared. Introducing radially varying density estimates in the lithosphere is for future studies. The conversion factor can be used to see the influence of temperature and composition on the shear wave velocity distribution of the lithosphere. A positive conversion factor usually means a temperature anomaly, whereas a negative value could indicate compositional effects (*Cammarano et al.*, 2003), but in many cases the anomaly has contributions from both. The ratio can readily become infinity, if one of the two fields is small. Therefore, we neglect locations where $\frac{\Delta \rho}{\rho} < 0.05\%$ and $\frac{\Delta V_S}{V_S} < 0.02\%$.

4   Forward gravity modelling

The density models are converted into a gravitational potential field using a spherical harmonic forward modelling technique (*Rummel et al.*, 1988; *Novák and Grafarend*, 2006; *Root et al.*, 2016). This method divides the density model in several spherical density layers that can have both lateral density variations and varying upper and lower boundary layers. The separate layers are converted to spherical harmonic coefficients representing the gravity potential field of that layer. This is done with a global spherical harmonic analysis using a weighted least squares algorithm (*Sneeuw*, 1994), that estimates the spherical harmonic coefficients (V_{nm}) from the density and geometry of the layer. The potential field (V) of the layer is represented as follows:

$$V(r, \Omega) = \frac{GM}{R} \sum_{n,m}^{\infty} \left(\frac{R}{r} \right)^{n+1} V_{nm} \, Y_{nm}(\Omega) \tag{4.4}$$

Y_{nm} represents the fully normalised associated Legendre functions and Ω is a shorthand notation for the lateral coordinates longitude and latitude. Multiple layers are analysed and combined, which results in a gravity potential solution for the complete density structure.

To ensure high-resolution in the radial structure the forward model consists of several layers starting with a radial thickness of 2.5 km, starting with the topography up to 10 km depth. From 10 km depth up to the Moho, the layers will have an increased thickness of 5 km. The lithosphere and asthenosphere layers will have a thickness of 25 km. This thin layering is needed to satisfy the convergence criterion of the spectral forward method (*Root et al.*, 2016) and preserve the high-resolution information of model C.

Table 4.1: Top part of the table shows statistical values of differences between forward modelled gravity field and gravity observation of EIGEN6C. The bottom part shows the statistics of the estimated lithospheric density anomalies. μ and σ are mean and standard deviation, respectively.

	Geoid		Gravity	
	μ [m]	σ [m]	μ [mGal]	σ [mGal]
EIGEN6C - Model A	-0.04	0.43	-0.05	8.04
EIGEN6C - Model B: CM95	-0.0024	0.66	0.08	12.2
EIGEN6C - Model B: NafeDrake	-0.0006	0.65	0.06	11.9
EIGEN6C - Model C: CM95	-0.08	0.51	-0.72	9.43
EIGEN6C - Model C: NafeDrake	-0.06	0.44	-0.39	8.06
	Density			
Model	μ [kg/m^3]	σ [kg/m^3]	min [kg/m^3]	max [kg/m^3]
Model A	-15.8	32.2	-121.5	104.8
Model B: CM95	-20.5	28.0	-112.3	88.3
Model B: NafeDrake	-12.8	29.9	-110.7	101.2
Model C: CM95	-30.7	27.3	-147.0	69.3
Model C: NafeDrake	-15.2	27.0	-118.6	105.7

5 Results

To quantify the effect of the different constraints in our modelling, we show the results of the various lithosphere models due to varying crustal models, V$_P$-to-density conversions, long-wavelength truncation of the gravity data, choice of reference model, and LAB. The difference between crustal model A and B gives information about the uncertainty in crustal models, whereas the difference between model B and C gives information about the effect of increased radial resolution in the crustal model. In all three cases, our modelled lithosphere densities are in the range of ± 110 kg/m^3. After the model comparisons, the uncertainty due to spherical harmonic truncation, isostatic reference model, and uncertainty in LAB model is considered.

Table 4.1 states the statistics of the differences of observed and modelled gravity field quantities both for the geoid and for the gravity anomaly. All values, mean (μ) and standard deviation (σ), should be zero for a perfect fit to the observations. So, these statistics are parameters to judge the performance of the modelled gravity solution to the observed gravity field. Model B has the highest standard deviation (12.2 and 11.9 mGal) from the gravity observations. The other models show a small improvement (Model A is 8.04, and Model C are 9.43 and 8.06 mGal). Similar observations can be gathered from the geoid misfit results and it can be seen that the iterative gravity fitting converges to a geoid anomaly standard deviation ranges from 0.45-0.65 m.

Furthermore, the gravity field residuals maps in Figure 4.6a, b, and c show gravity field variations of approximately ± 45 mGal in mostly random-looking patterns. Similar to in the table results, Model B has a higher residual compared to the other two models. In Model C a boundary misalignment at the eastern border of the study area is visible. The cratonic crust in CRUST1.0 compared to the regional model produces a large step in the mass of overall density model, resulting in an erroneous gravity anomaly. The rest
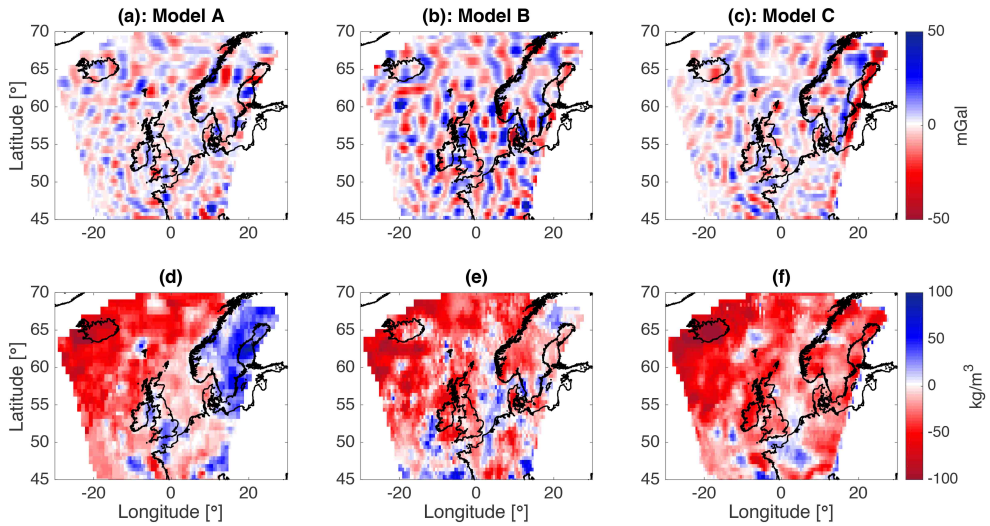
Figure 4.6: The top part of the Figure shows the gravity field residuals of the different models: (a) EIGEN6C - Model A, (b) EIGEN6C - Model B, and (c) EIGEN6C - Model C. The bottom part of the Figure shows the corresponding lithospheric densities for three cases: (d) Model A using CRUST1.0 for the crustal model, (e) Model B using EuCrust-07 model for the crustal model and the Christensen and Mooney conversion relations, and (f) Model C using the regional model for the crustal model and the Gardener/Christensen and Mooney conversion relations.

of the study area shows no large residuals in the three model solutions. Overall, there is little correlation between the gravity residuals and geologic structures, which also suggests a proper model fitting to the gravity field for the different lithosphere models.

5.1   Crustal models

The bottom part of Table 4.1 shows the statistics of the lithosphere density solutions. The lithosphere densities have a variation of ± 110 kg/m^3 around their mean value. These values are within reasonable mantle density estimates, when compared to other estimates for variation in mantle density, *e.g.* ± 150 kg/m^3 (*Kaban et al.*, 2004). The mean mantle density in the different models is between 3300 and 3328 kg/m^3. An interesting observation is that the mean value of model A (CRUST1.0) is similar to the Nafe-Drake models instead of the CM95 conversion relations.

Figure 4.6d, e, and f show the column-averaged density anomalies of the lithosphere with respect to the reference density of 3330 kg/m^3. The density anomaly maps from the three models illustrate the uncertainty introduced by the crustal models. Density anomalies become more positive when traveling from the oceanic to the continental lithosphere part of the region. In all three models, the lowest lithospheric density is found underneath Iceland. This can be explained by the existence of the spreading ridge, where hot asthenosphere is brought to the surface. The high temperature decreases the

density of the mantle material with respect to the continental lithosphere. Higher density is found underneath the continental crust to compensate the buoyant continental crust (*Christensen and Mooney*, 1995). The most visible difference between model A and model B and C is the density estimate of the lithosphere underneath Fennoscandia, which can be linked to the Baltic craton. Model A shows a pronounced density anomaly underneath Norway and Sweden, whereas model B and C show more small-scale features in the area. Moreover, the value of the density anomalies are largest in model A (-100 kg/m^3). Another distinct feature that is different between the three models is the density anomaly northwest of the Faroe Islands. This density anomaly could be attributed to the different Moho geometries in the crustal models. The density underneath the British Isles is similar for model B and C, but differs from model A. This could be attributed the the improved V$_P$ measurements available in that area for model B and C.

Some geologically interesting locations are discussed in the following section (see Figure 4.1 for location markers). One of the biggest lithospheric density mismatch is in the Fennoscandia region, where the density values between model A and C differ more than 150 kg/m^3. We hypothesise that CRUST1.0 is underestimating the density in the cratonic area. This is corroborated by lithospheric modelling of the Fennoscandian craton (*Kozlovskaya et al.*, 2004), where similar conclusions about the underestimated crustal density in CRUST1.0 have been made. Moreover, the lateral variations in the upper mantle underneath South Norway (*Maupin et al.*, 2013) are visible in model B and C, but do not show up in model A. This distinct mantle anomaly was needed to explain the isostatic compensation of the mountain range in South Norway (*Maupin et al.*, 2013; *Ebbing*, 2007a).

Furthermore, in the Porcupine sedimentary basin, offshore southwest Ireland, we can see more regional differences in the lithospheric density distribution. It is known that sedimentary basins are a large source of error in gravity modelling, because of uncertainty in their geometry and density distribution. The Mid-Norwegian Basin shows very local differences in lithospheric densities, but these density residuals can be considered small. In the Porcupine basin, model C shows distinct features in the lithosphere that are related to the Porcupine sedimentary basin, whereas in model A these are less prominent. To comply with isostasy in this area, the lithosphere needs to have a high density to compensate for the deep sedimentary basin. Local density differs in the lithosphere with approximately 75 kg/m^3 between model A and C. These differences are due to the extra information in model C from new seismic profiling of the Porcupine basin. The density structure correlates well with the free-air anomaly of that region (*Reston et al.*, 2001). Oddly, a distinct light density anomaly is situated underneath the positive anomaly. This particular signature can be explained because the sedimentary basin is divided by a volcanic ridge due to extensional stresses allowing basaltic rocks to rise into the upper part of the crust (*Reston et al.*, 2001). Local depletion of the mantle could explain the strip of low lithospheric density surrounded by the high density needed to compensate the sedimentary basin.

In addition, model B predicts high density features underneath the crust of the North Sea, that are not visible in model A and C. These density features are not related to any geological structures, such as the North Sea Graben, and might be artefacts. Furthermore, in the proximity of the Faroe Islands the feature discussed earlier can

also be seen in the lithosphere densities. All models have a high density just north of the Faroe islands. Model A shows a single density structure, whereas model B and C show a double feature. This structure does not correlate to the bathymetry in the area, but does correlate with the Moho geometry. The deep Moho in the regional models need high density in the lithosphere for compensation. There is evidence for magmatic underplating in this region (*Richardson et al.*, 1998), which greatly affects the radial density distribution. When this structure is not taken into account, for example because of low radial resolution of the crustal model, it introduces errors in the lithosphere model.

Continuing the comparison, a difference in lithospheric density can be seen onshore France. A positive density anomaly underneath the Paris Basin is visible in model B and C. Model A does not show this feature. Again, the high density can be explained by isostasy to compensate the sedimentary basin, where relatively lighter material is abundant. Overall, the regional model results show that the different crustal models do have an effect on the determination of lithospheric structures from gravity data. This comparison shows that local density features in the lithosphere can differ significantly due to the selected crustal model.

5.2 V_P-density conversion

To quantify the uncertainty introduced by the conversion of V_P to density both model B and C are constructed using the two different conversion relations, discussed in Section 2.2. Figure 4.7 shows the resulting lithospheric density maps. The spatial structure of the density maps is comparable for the different conversion relations. Some density anomalies are more pronounced using the Nafe-Drake conversion, like the Faroe anomaly in model C. The mean and standard deviation of the differences between the two conversion relations for model B are: μ_B = -7.7 kg/m^3 and σ_B = 8.4 kg/m^3. For model C the values are similar of magnitude: μ_C = -15.5 kg/m^3 and σ_C = 10.1 kg/m^3. These variations are smaller than the variations due to different crustal models. This suggests that improvement in the seismic model of the crust is more important than the improvement of V_P to density conversion when considering the uncertainty of density in the lithosphere derived from gravity.

5.3 Long-wavelength signal removal

The bandwidth of the gravity observations should be selected such that it is sensitive to density anomalies of the lithosphere. Some studies state that spherical harmonic degree 10 is the appropriate lower truncation limit to remove deep mantle anomalies (*Herceg et al.*, 2016; *Bowin*, 2000), but others conclude that deep mantle dynamics have a significant contribution to higher wavelengths of the gravity field (*Root et al.*, 2015). *Deschamps et al.* (2001) found that the geoid anomalies between spherical harmonic coefficients 11-16 are most sensitive to the lithosphere.

To study the effect of the truncation limit on the results, the limit of the gravity observations is varied during step 3. The upper truncation limit is fixed at degree and order 180, because there is only 1x1 arc-deg crustal information from CRUST1.0. We have varied the lower truncation limit to the following values: 3, 5, 10, 20, 30, and 35. We examine the overall density variation to see where the truncation has significant
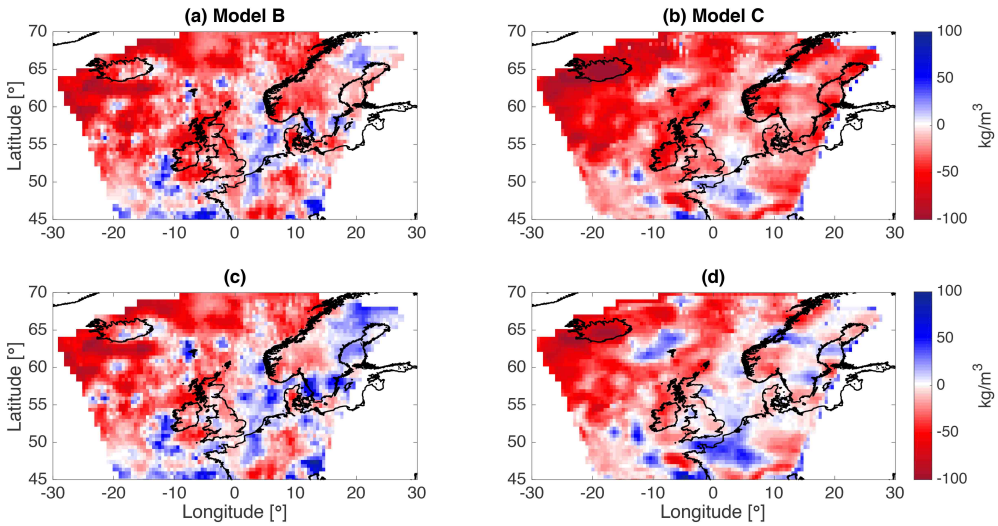
Figure 4.7: Lithosphere density maps of (a) Model B using the Christensen and Mooney conversion relations for the crustal structures, (b) Model C using the Christensen and Mooney conversion relations, (c) Model B using the Nafe-Drake conversion relations for the crustal structures, and (d) Model C using the Nafe-Drake conversion relations.

Table 4.2: Statistical values of lithospheric density solutions and their fit to the observed geoid using different bandwidth selections in the iterative density fitting process. The models are depicted by their spherical harmonic truncation. μ and σ are mean and standard deviation, respectively.

Spectral bandwidth	Density μ [kg/m³]	σ [kg/m³]	min [kg/m³]	max [kg/m³]	Geoid fit 3σ [m]	# of iterations	scaling factor
Isostatic	-13.6	24.2	-94.4	96.5			
3-180	-9.3	22.6	-94.4	100.8	2.7	25	0.15
5-180	-15.1	22.6	-98.6	93.4	3.0	20	0.1
10-180	-15.2	25.3	-111.5	99.9	1.6	14	0.5
20-180	-14.5	26.0	-112.4	100.6	1.2	8	1
30-180	-14.6	26.5	-116.4	102.7	0.9	8	1.5
35-180	-14.3	26.2	-113.4	101.7	1.1	5	2

effect. Table 4.2 shows the statistics of the different lithospheric density solutions, their geoid, the amount of iterations needed, and the scaling factor used. Most of the variation (σ) in the density values is between 22-26 kg/m³ to adjust the isostatic model, such that it fits with the gravity field observations. Solutions with lower truncation degree limit (3 to 5) show a slightly smaller standard deviation than with a higher truncation, degrees (10 to 35).

The spatial variation between solutions with different truncation are shown in Figure 4.8. The density variation between the solutions with spherical harmonic truncation 3 and 35 is around ±20 kg/m³. The largest variation is a west-east trend and is situated
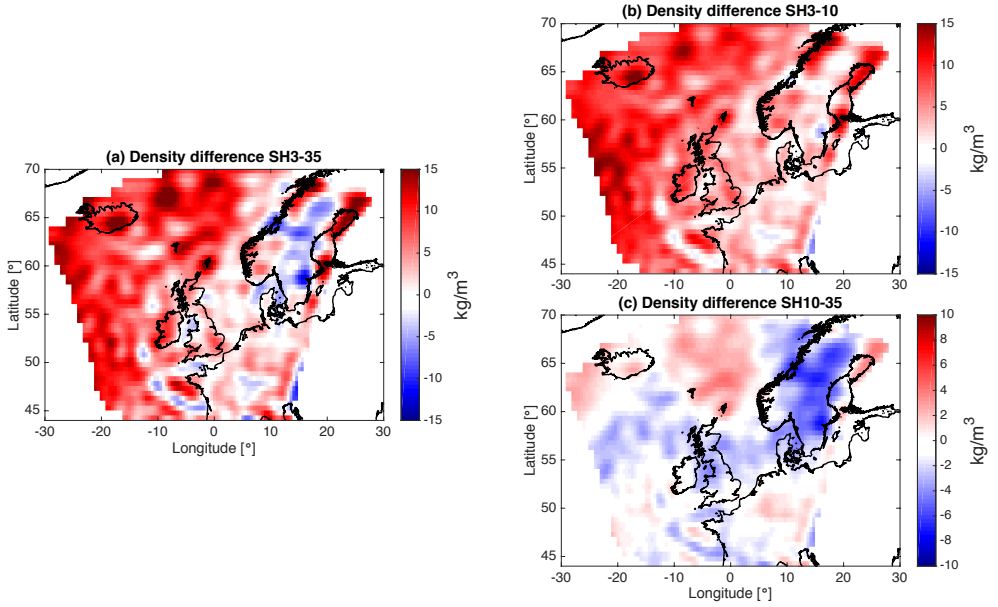
Figure 4.8: Density variation in the lithosphere when using different spherical harmonic truncations. The difference in density between models using a lower truncation limit of (a) 3 and 35, (b) 3 and 10, and (c) 10 and 35.

in the spherical harmonic coefficients 3 to 10, as can be seen in Figure 4.8b. Figure 4.8c shows the variation between the solution using 10 and 35. Here, can be seen that the choice of truncation between 10 and 35 introduces an uncertainty of approximately $\pm$ 5 kg/m^3 in the computed density models. Overall, the statistical results of the lithosphere models with higher truncation limits do not differ significantly. From this evidence, we suggest using a truncation limit of degree 10 to remove deep mantle effects, which agrees with other studies.

5.4 Reference model

To study the effect of the chosen reference model in Equation (4.1) the model is varied to see the effects on the final result. The selected reference model, or nominal model, used in this study has 30 km crustal thickness with crustal density of 2850 kg/m^3, complemented by the 270 km thick mantle layer with a density of 3300 kg/m^3. The reference model is varied by changing the mantle density between 3200 and 3400 kg/m^3 with increments of 25 kg/m^3. The chosen variation in mantle densities encompasses enough uncertainty to quantify the effect of the reference model on the final result.

The resulting lithosphere density anomalies are inspected to asses the effects of the changes to the reference model. The results show that the lithosphere densities differ
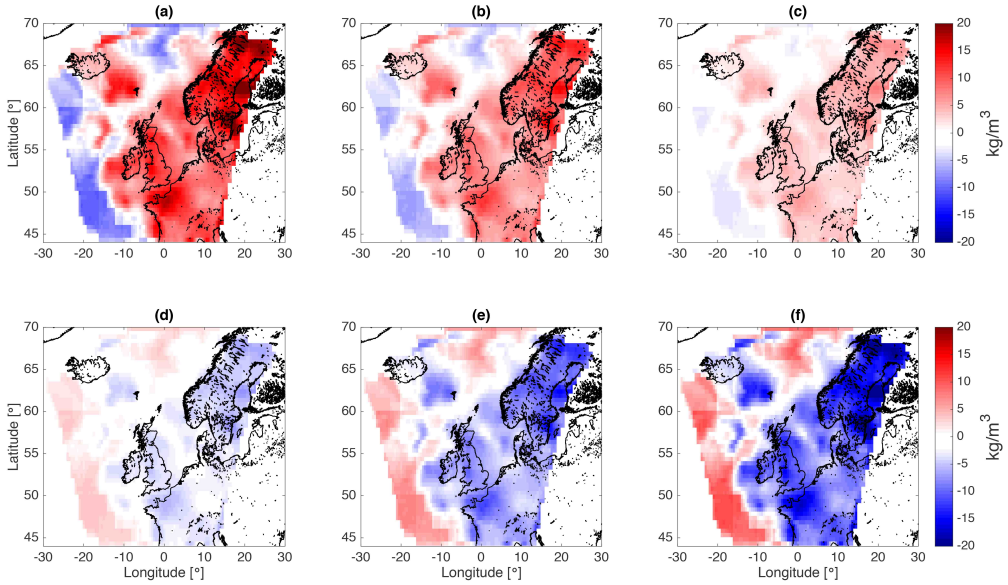
Figure 4.9: Density anomaly difference in the lithosphere when using different reference mantle density compared to the nominal model: (a) 3275 kg/m³, (b) 3250 kg/m³, (c) 3225 kg/m³, (d) 3325 kg/m³, (e) 3350 kg/m³, (f) 3375 kg/m³.

± 20 kg/m³ from the densities in the nominal model in extreme cases of averaged mantle densities of 3200 and 3400 kg/m³. The other models have smaller differences with the nominal reference model results (see Figure 4.9). All density differences have a correlation with the Moho geometry of the chosen crustal model. This correlation can be explained because the model is trying to balance mantle and crustal masses, such that they fit the gravity field. When the reference mantle density is changed, the equilibrium is changed by an amount of mass that correlates to the Moho geometry.

5.5   Uncertainty in the LAB model

Finally, to examine the influence of uncertainties in the LAB model, Eq. (4.1) is evaluated for a model with a lithosphere thickness (D_{lith}) and a model with a lithosphere thickness plus an uncertainty ($D_{lith} + \Delta D$). By combining the two relations and neglecting the spherical representation, the following relation is obtained:

$$\Delta\rho_{old}D_{lith} = (\rho_{lith} - \rho_{asth})\Delta D + \Delta\rho_{new}(D_{lith} + \Delta D). \qquad (4.5)$$

Typical errors in LAB depth underneath cratons are found to be around 10 percent (*Kuskov et al.*, 2014). An uncertainty of the LAB thickness of 10 percent, $\frac{\Delta D}{D_{lith}} = 0.1$, is

substituted to Eq. (4.5). This results in a relationship for the density of the lithosphere

$$\Delta\rho_{new} = \frac{\Delta\rho_{old} - 0.1(\rho_{lith} - \rho_{asth})}{1.1} \tag{4.6}$$

With this relation it can be proven that the density in the lithosphere also has around 10 percent uncertainty, which is around ± 11 kg/m^3 for the ± 110 kg/m^3 variation in this study area.

6   Comparison to tomography

The independently determined lithosphere structures from gravity modelling can be compared with models of lithospheric structures from seismic tomography. However, Figure 4.10 shows the gravity-based models have a different spectral signature to the tomography model. Over the complete spectrum, the degree variance of the gravity-based models is much larger. In order to make the spectral signature comparable, we apply a Gaussian filter to the gravity-based density models such that short-wavelength features are reduced (*Jekeli*, 1981), as SL2013sv is made with a nodal spacing of around 280 km (*Schaeffer and Lebedev*, 2013). After studying several limits it was found that applying a Gaussian filter with a halfwidth of 200 km best approaches the spectral signature of the S-wave model. This can be seen in Figure 4.10. Here, the gravity-based model that is filtered with a 200 km halfwidth Gaussian filter is almost completely overlapping with the degree variance of the V_S model. After this filter is applied, the spherical harmonic coefficients equal to and lower than degree and order 10 are truncated, because these were also truncated in the gravity fitting process. The filtered results are shown in Figure 4.11.

After the filtering, the tomographic and the gravity-based models have a density variation and spatial structure of similar character. The main features of the lithosphere are represented by all four models. The density anomalies that mark the Icelandic region are represented by all models, as are the large scale anomalies around the British Isles. The S-wave based densities show a density anomaly underneath Scotland and Ireland, which is best represented by model C. The southewst density high was not seen in the unfiltered gravity-based models, but is now present in all models. Underneath Denmark and Germany, the density low is also present in all models except model B. This density signal could be a remnant of the North Sea anomalies. However, the density high underneath the west coast of France is best represented in model C. Models A and B underestimate the inland extent of the anomaly, failing to model the Paris Basin signal. Moreover, there are other large scale features in the seismic observations that cannot be reproduced by the gravity-based lithosphere models. Fennoscandia is different in all gravity-based models. Model A over-estimates the density low due to the cratonic area, whereas model C under-estimates this feature. Moreover, north of the British Isles a large misfit is seen between the lithospheric density estimates. The Faroe anomaly, discussed in Section 5 and most pronounced in model B and C, is not seen in the S-wave model. Model A shows a much less pronounced density anomaly in the Faroe Island area. On the contrary, a positive anomaly northeast of the Faroe Islands in the Norwegian Sea is seen in the S-wave model, but is not present in all the gravity-based models.
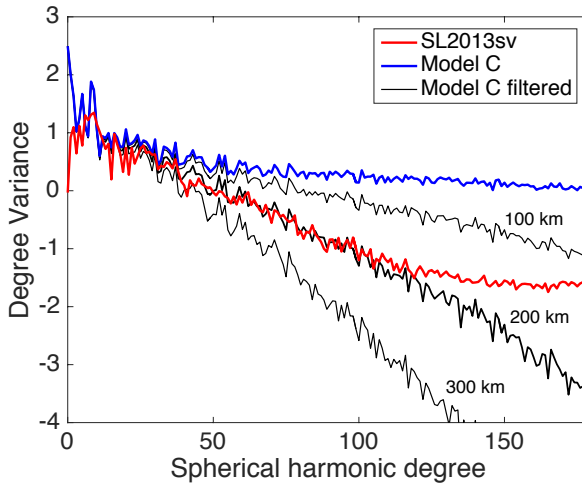
Figure 4.10: The spectral degree variance of the lithosphere density derived from $\mathbf{V}_S$ anomalies of SL2013sv model (red) and lithosphere density anomalies of model C using the Nafe-Drake crustal conversion (blue). The black lines are the filtered densities of model C using different Gaussian halfwidths: 100, 200, and 300 km.
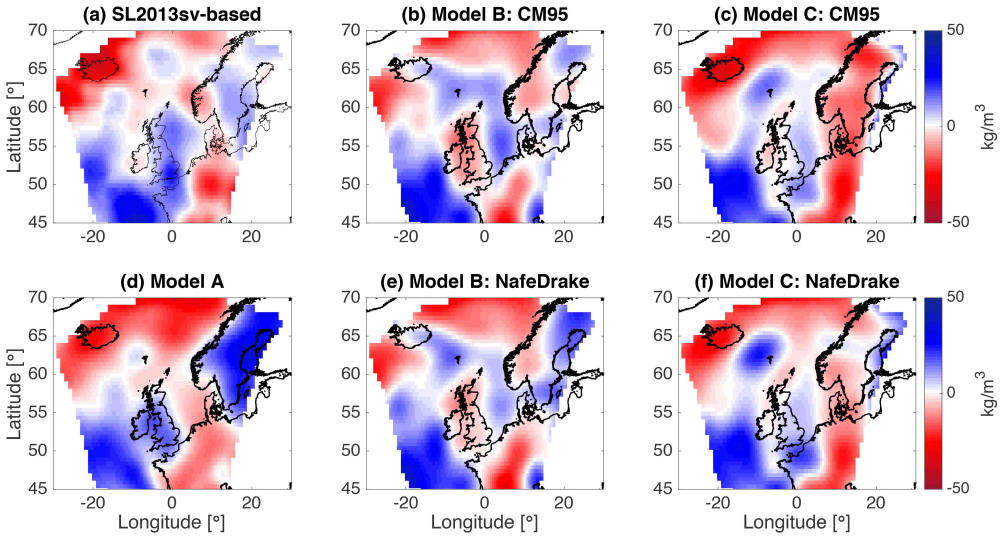
Figure 4.11: Lithospheric densities from the S-wave velocity conversions and gravity-based solutions for model A, B, and C. The gravity-based results are filtered using a Gaussian filter with 200 km halfwidth.

Table 4.3: Statistical values of the Gaussian filtered lithospheric density fields of the tomographic model (SL2013sv) and the gravity-based models. The differences between the tomographic model and the gravity-based models are in the bottom part of the table. μ and σ are mean and standard deviation, respectively.

Model	Density μ [kg/m^3]	σ [kg/m^3]	min [kg/m^3]	max [kg/m^3]
SL2013sv	0.52	12.9	-39.5	39.4
Model A	0.37	15.1	-32.6	34.5
Model B: CM95	1.38	11.5	-27.9	40.7
Model B: NafeDrake	1.20	12.4	-32.0	40.7
Model C: CM95	-3.41	13.5	-35.6	28.5
Model C: NafeDrake	-0.57	12.7	-30.9	28.8
SL2013sv - Model A	0.15	11.5	-34.4	26.5
SL2013sv - Model B: CM95	-0.86	11.9	-42.1	28.1
SL2013sv - Model B: NafeDrake	-0.68	12.1	-43.0	27.0
SL2013sv - Model C: CM95	3.93	9.4	-23.0	26.9
SL2013sv - Model C: NafeDrake	1.08	8.8	-30.3	24.8

Table 4.3 shows the density comparison between the filtered models. Now, the density values of the tomographic model are similar to the gravity-based models with density variations of $\pm$ 30-40 kg/m^3. These values are much lower than other gravity studies have reported ($\pm$ 70-150 kg/m^3) (*Herceg et al.*, 2016; *Kaban et al.*, 2004), as well as our results for the unfiltered models ($\pm$ 110 kg/m^3). This indicates that it is important that both modelling approaches have the same spectral content. However, we have seen that the main differences are due to local features. This is also corroborated by the bottom part of Table 4.3, where the differences between the tomographic and the gravity-based lithosphere models are presented. As in the unfiltered case, model C (Nafe-Drake) performs best, but also here the differences between the other models are not significant. The main differences are due to the dissimilar modelling of Fennoscandia by model A and large anomalies at the Faroe islands and the Porcupine basin in model B and C.

With the filtered density values we can compute laterally varying conversion factors. Figure 4.12 shows the estimated conversion factor between the S-wave velocities and gravity-based densities from model C using the Nafe-Drake conversion. The colours depict the magnitude of the conversion factor. Blue depicts positive values and red for negative, whereas grey illustrates zones that are undetermined, because of our cut-off constraints discussed in Section 3.2. Some correlation between the conversion factor and tectonic regions can be deduced. A low conversion factor is seen in central Fennoscandia, which could mean that the compositional effect is more important than the thermal effect on the V_S to density conversion in that area. Cratonic areas are thought to have different composition due to depletion of the mantle material (*Jordan*, 1979). Further to the south a negative conversion factor is present at the Tornquist zone (*Bock et al.*, 2001). Here, the transition between cratonic and continental lithosphere is present. More positive conversion factors are seen in the continental region of western Europe, including the English part of the British Isles. Only western Ireland shows a small
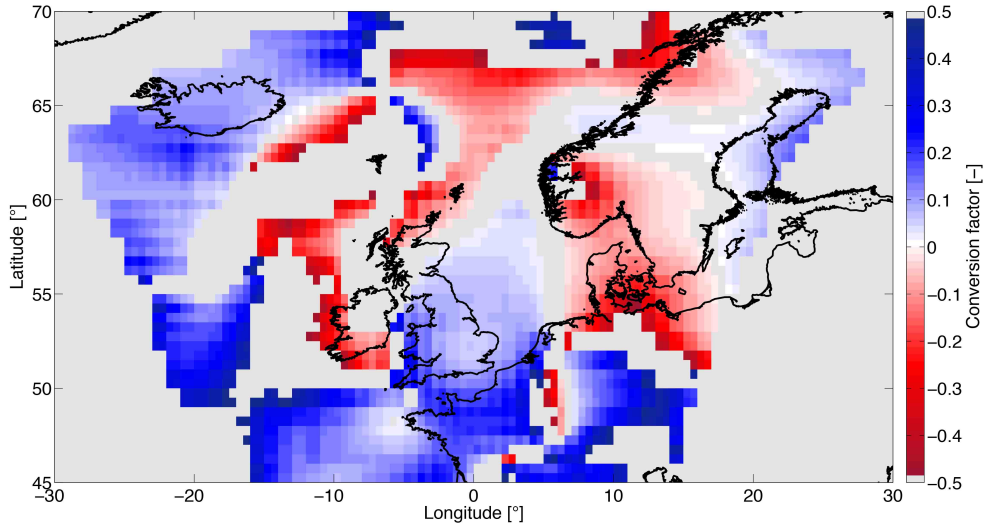
Figure 4.12: **The laterally varying conversion factor between the S-wave velocities of
SL2013sv in the lithosphere and the gravity-based densities of model C (Nafe-Drake).
The gravity-based results are filtered with a Gaussian filter (halfwidth of 200 km). The
grey zones are areas where the conversion factor could not be determined.**

negative anomaly, becoming more positive towards the east, which could be related to
the Proto-Ireland plume (*Landes et al.*, 2007; *Fullea et al.*, 2014; *Jones et al.*, 2014).
The plume had a thinning effect on the solid lithosphere and changed the composition
of the lithosphere (*Landes et al.*, 2007; *Al-Kindi et al.*, 2003). Comparing our results
with the density models of Fullea et al. (2014), the changing conversion factor could be
explained by the proposed compositional change between western and eastern Ireland.
Furthermore, a clear change in conversion factor cuts through southern Scotland and
central Ireland, depicting the old boundary between Avalonia and Laurentia. North of
this boundary, the conversion factor is negative. It separates thinned cratonic crust of
Laurentia to the northwest from Proterozoic basement of Gondwanan age (Avalonia)
to the southeast. Here, both thermal and compositional processes would dominate the
density of the lithosphere. Overall, this shows that the determination of density from
seismic and from gravity data can help distinguish tectonic settings.

7   Concluding remarks

In this study, we have compared lithospheric structures determined by gravity-based and
seismic-based modelling. The drawbacks of seismic modelling are uneven distribution
of observation data, the dependency on an *a-priori* crustal model, coupled uncertain-
ties between velocity and depth-to-interface, and the uncertain relations between wave
velocity and physical parameters, such as density, temperature, and composition. The

uncertainty in gravity-based modelling is based on the introduction of constraints to eliminate deep mantle effects and the crustal gravity signal. Furthermore, we have proposed a novel gravity modelling methodology to estimated lithospheric density anomalies, using a crustal model, lithospheric isostasy, and gravity field observations.

The three different crustal models used for eliminating the crustal gravity signal are: CRUST1.0, EuCrust-07, and a regional P-wave velocity model. The variation in crustal P-wave velocity to density conversion show less differences between the conversion methodologies than differences due to different crustal models. The uncertainty in the crustal models is mainly caused by data acquisition. The regional crustal model in this study shows a small improvement in misfit to the observed gravity field, but the averaged differences between the three models are not significant. The different crustal models can cause variations in lithosphere density up to ± 110 kg/m^3. The different conversion relations introduce an uncertainty in the lithospheric density of of ± 10 kg/m^3. Moreover, the effect of different truncations of the spherical harmonic representation of the gravity field does not have a significant effect (± 5 kg/m^3), when a lower truncation value of 10-35 is chosen. Also, the reference model used in the isostatic step of the methodology does not have a significant effect. The estimated lithosphere density varied by not more than ± 20 kg/m^3 due to reference model changes. Finally, the LAB uncertainty causes density variations in the lithosphere of around 10 percent.

The variation in density needed to fit the gravity field in the lithosphere (± 110 kg/m^3) is larger than the density variations obtained by converting the S-wave velocity observations (± 35 kg/m^3), due to spectral imbalance. After filtering the gravity-based lithosphere solutions, we have shown that tomographic and gravity-based lithosphere models are comparable. The best Gaussian filter to compare our gravity-based results to density estimated from the tomography model SL2013sv has a halfwidth of 200 km.

With the proposed gravity-based lithosphere modelling, density structures can be determined independently from mantle tomography. However, high-resolution V_P crust models are needed to reduce the uncertainty in the estimated density maps. The independent density estimates can be used together with tomographic models to compute lateral variations in the conversion factor, giving insights on the importance of compositional and thermal effects on seismic velocity anomalies.

Acknowledgments

Paper IV - GRACE gravity observations constrain Weichselian ice thickness in the Barents Sea

"One man's noise is another man's signal."

– Edward Ng, *New York Times, (1990)*

GRACE gravity observations constrain Weichselian ice thickness in the Barents Sea

***B.C. Root**[a], L. Tarasov[b], and W. van der Wal[a]*

Abstract

The Barents Sea is subject to ongoing postglacial uplift since the melting of the Weichselian ice sheet that covered it. The regional ice sheet thickness history is not well known because there is only data at the periphery due to the locations of Frans Joseph land, Svalbard, and Novaya Zemlya surrounding this paleo ice sheet. We show that the linear trend in the gravity rate derived from a decade of observations from the GRACE satellite mission can constrain the volume of the ice sheet after correcting for current ice-melt, hydrology and far-field gravitational effects. Regional ice loading models based on new geologically-inferred ice margin chronologies show a significantly better fit to the GRACE data than that of ICE-5G. The regional ice models contain less ice in the Barents Sea than present in ICE-5G (5-6.3 m equivalent sea level vs. 8.5 m), which increases the ongoing difficulty in closing the global sea level budget at the Last Glacial Maximum.

1 Introduction

The geological sea-level record in Barbados (*Peltier and Fairbanks*, 2006) estimates the sea level at the Last Glacial Maximum (LGM) to be on average 120 meter lower than the present-day sea level. The widely used ICE-5G reconstruction (*Peltier*, 2004) has a total volume of LGM-grounded ice equivalent to a 118.7 m sea-level rise assuming the present-day ocean area. However, since publication of the model, recent reconstructions of the Antarctic ice sheet have a smaller LGM-grounded ice volume compared to the 17.3 m eustatic sea level (ESL) of ICE-5G (*Peltier*, 2004). These include both pure Glacial Isostatic Adjustment (GIA) reconstructions (7 mESL) (*Ivins et al.*, 2013), as well as hybrid glaciological/GIA modelling approaches (8-10 mESL) (*Whitehouse et al.*, 2012) and (6-15 mESL) (*Briggs et al.*, 2014). Geodetic data of North America have indicated a smaller ice sheet there (*Lambert et al.*, 2006; *van der Wal et al.*, 2009; *Argus and Peltier*, 2010) as also occurs in a recent data-calibrated glaciological reconstruction (*Tarasov et al.*, 2012). *Clark and Tarasov* (2014) suggest previously unaccounted for grounded ice in the Northern Hemisphere as solution for missing LGM ice. To exacerbate the problem, a revision of the GIA model to reflect the effect of a high-viscosity slab in the mantle below Barbados brings the sea level rise inferred from Barbados to about 130 m (*Austermann et al.*, 2013). Thus, the total ice volume required to match sea-level data is increased, while the contribution from the known ice sheets in North America and Antarctica is smaller than previously thought. The missing ice must come from other ice sheets of which the thickness is not well constrained yet.

(a): Delft University of Technology, The Netherlands
(b): Memorial University in St. John's, Newfoundland, Canada
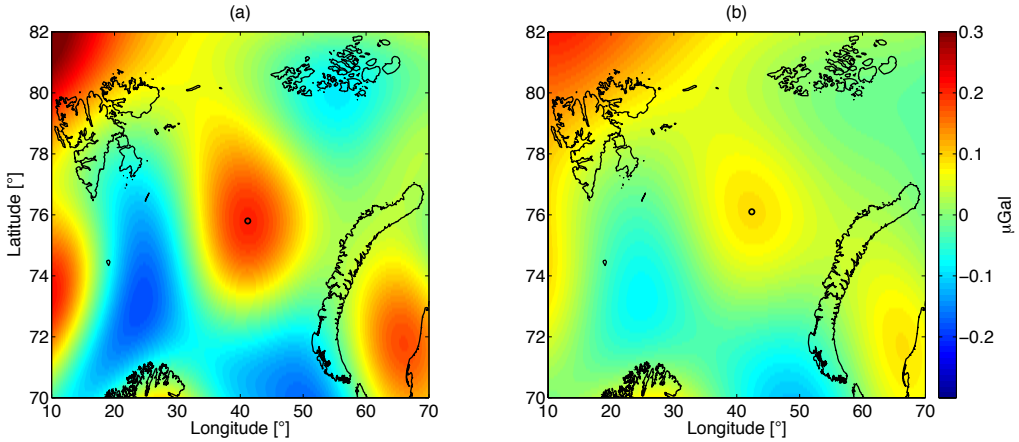
Figure 5.1: GRACE gravity trends at the surface after band-pass filtering and correction for present-day ice-mass change. A band pass filter with high-pass half width of (a) 200 km and (b) 300 km and low-pass halfwidth of 600 km for both models is assumed. The present day ice mass change corrections adopted are: -3.3 Gt/yr (Svalbard), -4.2 Gt/yr (Novaya Zemlya), and -0.9 Gt/yr (Frans Joseph Land). The black dot depicts the location of maximum gravity change.

One possibility to locate some of the missing ice is the Barents Sea Region, which delivers 8.5 m of sea-level rise in the ICE-5G model. This area is one of the largest continental shelves, which could have been completely ice covered during the LGM (*Svendsen et al.*, 2004a). However, the ice cover during the LGM in this area is heavily debated, with some stating that large parts of the northern coastal areas of Russia were covered with ice sheets (*Grosswald*, 1998). Furthermore, sea-level curves collected from the coasts of Svalbard, Novaya Zemlya and Frans Joseph Land indicate grounded ice in the Barents Sea region at the LGM (*Kaufmann*, 1997). Others argue that the ice margin during the LGM was situated offshore, covering only the northern tip of the Taymyr Peninsula (*Mangerud et al.*, 2002; *Lambeck*, 1996). Unfortunately, all these studies could only use observations that are located at the boundaries of the predicted post-glacial uplift, probing areas far away from the maximum expected uplift. Observations in the center of the Barents Sea (see Figure 5.1) could reduce the uncertainty of LGM ice mass estimates and contribute to resolving the global ice budget of land ice at the LGM.

Observations of time-variable gravity from the GRACE satellite mission have been able to constrain ice-loading history in North America (*Tamisiea et al.*, 2007) and are successfully used in Scandinavia (*Steffen et al.*, 2008; *Root et al.*, 2015). The gravity rate in areas of uplift in North America and Scandinavia were shown to agree with uplift rates measured by GPS uplift rates (*van der Wal et al.*, 2011). With the increased precision of later GRACE releases and longer observational time-series, signals of smaller spatial scale should become more visible against background noise. This study investigates the constraint provided by GRACE data on models of the past ice sheet in the Barents Sea. We compare the GRACE-derived gravity rate with the predicted gravity rate from GIA models with different mantle parameters and for different ice-loading histories, assessing

whether or not the employed ice-loading models are a good representation of the past ice thickness at the Barents Sea region.

2   Ice-loading models

The regional ice-sheet chronologies are from an ongoing Bayesian calibration of the glaciological Glacial Systems Model (GSM) for Northern Europe and adjacent continental shelves. The Bayesian calibration follows the approach of *Tarasov et al.* (2012) and thereby generates a posterior probability distribution of ice-sheet chronologies given GSM run fits to the calibration constraints. The latter consists of RSL data, present-day vertical velocities, and a geologically-inferred deglacial ice-margin chronology (DATED) (*Hughes et al.*, 2014). The RSL data is from a slightly cleaned up 2006 snapshot of the University of Toronto database upon which ICE-5G was based (*Peltier*, 2004). The ice-margin chronology is distinguished by the inclusion of inferred max/min ice-margin isochrones for each time slice. This DATED chronology was recently revised, and we include results from calibrations with both the older and newer versions of DATED, which had respectively later ("late deglaciation models") and earlier ("early deglaciation models") deglaciation of the Barents Sea region. The initial calibration used uplift data from *Argus and Peltier* (2010) while the revised calibration with the newer version of DATED also used an updated and much larger set of geodetic constraints from *Kierulf et al.* (2014).

The selected regional ice loading models, which have a low misfit to the RSL and uplift data, are compared to the ice thicknesses of the global ice loading model, ICE-5G (*Peltier*, 2004). We use ICE-5G version 1.2 with an order 256 Gaussian grid for the complete time period of 0-122 ka, downloaded from: http://www.atmosp.physics.utoronto.ca/peltier/data.php. In the case of the regional ice-sheet models, the North Eurasian ice sheets in ICE-5G were replaced by the calibrated ice sheets. ICE-6G ice thickness values are not available, we therefore use the published Stokes coefficients for ICE-6G_C (VM5a), see Figure 5.2a and b. The latest ANU model (*Schmidt et al.*, 2014) is outdated and a new model will be published soon (pers. comm. Kurt Lambeck), so it is not used in this study.

The ice-volume-equivalent sea level for the different ice models for the Barents Sea Region used in this study can be seen in Figure 5.2c and d. The selected regional models all have low misfit values to the RSL and GPS uplift data sets. The ESL change for the Barents Sea is a numerical conversion of the ice volume change above $69°$ latitude and between $0°$ and $60°$ longitude, using a density ice and liquid water to be 920 kg/m^3 and 1000 kg/m^3, respectively. The contribution from the grounded ice in the Barents Sea region ranges from 8.5 m (ICE-5G) to 5-6.3 m (DATED models). The older late-deglaciation calibrated ice models have a similar onset of glaciation as the ICE-5G model.
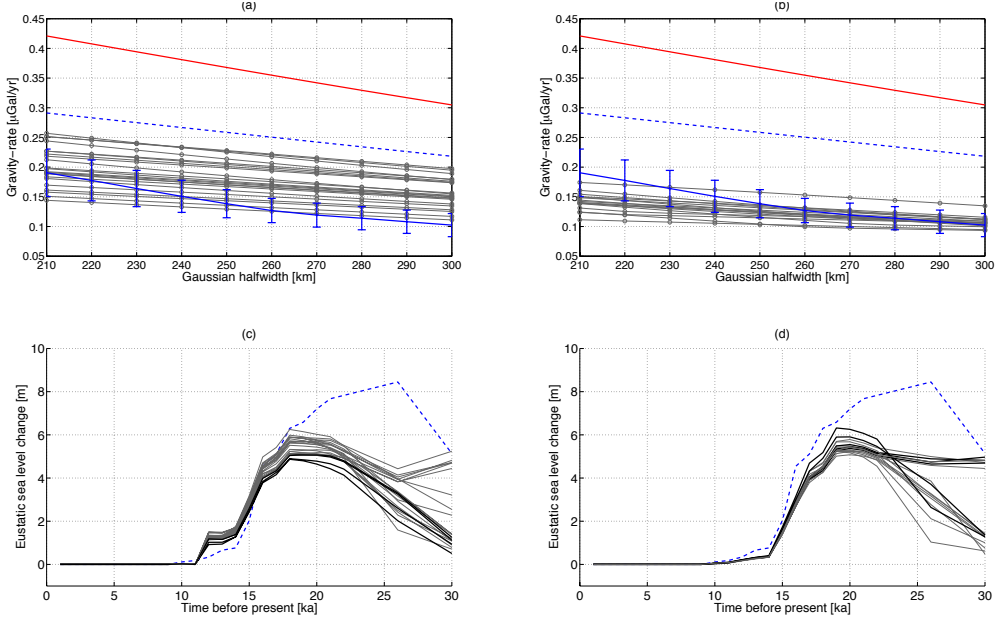
Figure 5.2: Top: Maximum gravity rate in the Barents Sea. The solid blue line depicts the GRACE observations with the error bar indicating the uncertainty in ice mass loss estimates from Table 5.1 and the formal errors. The dashed blue line shows the GIA model results using ICE-5G, the red represents ICE-6G. The spread in maximum gravity rate of the *Tarasov et al.* (2012) models are shown (grey) for: (a) late deglaciation and (b) early deglaciation. On the x-axis are different low-pass filter half widths. The high-pass filter halfwidth is set to 600 km for this particular representation. Bottom: The ice volumes of the different models expressed as equivalent sea level change. The dashed blue line is the ICE-5G model. (c) Regional models with late deglaciation. (d) Regional models with early deglaciation. The grey lines represent ice loading models that failed the GRACE criteria and the solid black lines passes this criteria.

3   GIA model

In GIA modeling, the surface load consists of land-ice and water redistribution. These are obtained by solving the full sea-level equation, including melt-water influx, time-dependent continent margins and rotational feedback (*Mitrovica and Peltier*, 1991), (*Kendall et al.*, 2005). The response of the solid Earth to a surface load is computed using the multi-layered normal-mode method (*Wu and Peltier*, 1982; *Vermeersen and Sabadini*, 1997). Full details can be found in *van der Wal et al.* (2009). To see the effect of the different ice loading histories on the gravity change, similar rheological models for the Earth layers are used. The model consists of an elastic lithosphere of 60 km, followed by a 40 km thin sub-lithospheric layer with a viscosity of 1×10^{22} Pa s, an upper mantle (570 km) with a viscosity of 0.5×10^{21} Pa s, and a double layered lower mantle, with viscosities of 1.6×10^{21} (500 km) and 3.2×10^{21} (1720 km). This viscosity structure is called VM5a (*Peltier and Drummond*, 2008). Later, the rheological parameters will be varied to study their effect on gravity change estimation in the Barents Sea.

Table 5.1: The ice-mass loss estimates from GRACE based on a global mascon solution compared to results from literature. The study of *Jacob et al.* (2012) also uses a global mascon model and *Moholdt et al.* (2010, 2012) is based on ICESat altimetry data of the melting ice sheets.

Location	Area [km^2]	Estimate [Gt/yr]	Jacob et al. (2012) [Gt/yr]	Estimate [Gt/yr]	Moholdt et al. (both) [Gt/yr]
Svalbard	56,400	-3.3 ±1.2	-3 ±2	-4.8 ± 0.3	-4.3 ± 1.4
Novaya Zemlya	47,600	-4.2 ±1.0	-4 ±2	-8.0 ± 0.3	-7.6 ± 1.2
Frans J. Land	16,150	-0.9 ±0.7	0 ±2	-1.9 ± 0.6	-0.9 ± 0.7
Total:	120,150	-8.4 ±1.7	-7 ±3.5	14.7 ± 0.73	-12.8 ± 2.0
				ICESat period	**(2003-2008)**

To evaluate the different models, a misfit criterion is defined (*Press et al.*, 1992):

$$\chi^2 = \frac{1}{N_i} \sum_i \left(\frac{o_i - m_i}{s_i} \right)^2, \qquad (5.1)$$

where the corrected GRACE observations are represented by o, with the standard deviation expressed in s. The GIA model results are represented by m and the subscript i represent different filter settings to the GRACE data (see supplementary material, which can be found on website of original publication). N is the number of data points, which reflects the number of different filter settings of the GRACE data.

4   GRACE data

The GRACE observations used in this study are the CSR Release-5 monthly gravity fields (*Bettadpur*, 2003) for the period February 2003 up to and including July 2013. The degree-2, order-0 coefficients are replaced by the values from Satellite Laser Ranging (*Cheng et al.*, 2013). A linear trend is estimated in the presence of an annual and semi-annual signal. In the Barents Sea, these linear-trend gravity solutions contain the gravity change due to GIA as well as ongoing ice melt, continental water storage changes, and noise.

Ice-mass loss in the Arctic Archipelagos of the Barents Sea can be estimated independently from GRACE with data from the ICESat mission (*Moholdt et al.*, 2010, 2012; *Nuth et al.*, 2010), but it stopped operating after 2008. Therefore, in this study we employ mass-loss-rate estimates from GRACE based on a global mascon model (*Schrama et al.*, 2014) (Table 5.1). Mass-loss estimates need to be corrected for GIA effects. The correction introduces an uncertainty, however, this is small compared to other systematic errors in the mass-loss estimation. To validate, the values from the mascon solution are compared with those of *Jacob et al.* (2012) and they overlap within uncertainties. Furthermore, the solutions agree within the uncertainty with the estimates in the ICESat-based studies of *Moholdt et al.* (2010) and *Moholdt et al.* (2012) for the period of 2003-2008 (see Table 5.1).

To correct the GRACE data for ongoing glacial-mass changes, the areal extent of the ice melt is required in addition to the mass-loss estimates. The ice mass losses are homogeneously distributed over the glaciated areas of Svalbard (approximate melt area of 56,400 km^2), Frans Joseph land (approximated melt area is 16,150 km^2), and Novaya Zemlya (approximated melt area is 47,600 km^2) north of 73° latitude. The ice mass losses in Table 5.1 are converted to surface-mass changes and subsequently converted to gravitational-potential coefficients taking into account elastic loading (*Wahr et al.*, 1998).

Finally, continental water-storage changes are corrected for using the GLDAS model (*Rodell et al.*, 2004) from which glaciated areas were excluded. A Gaussian bandpass filter is used to reduce remaining noise in the GRACE observations. However, too much filtering removes a substantial part of the GIA signal while too little leaves noise in the data. In the supplementary material, we show that our conclusion is valid for a range of Gaussian low-pass filter half widths between 200 km and 300 km. Long wavelength signals from other sources, such as the ice mass changes in Greenland and continental hydrology uncorrected for by the GLDAS model, can be mitigated by removing the low degrees in the GRACE data and GIA models, using a high-pass Gaussian filter, varying the half widths between 500 and 700 km. Effects of internal dynamics of the deep Earth are also filtered, but we reckon that this motion is not fast enough to be observed by GRACE. *Greff-Lefftz* (2010) showed that no visible effect is seen in the $\dot{J}_2$ coefficient.

The corrected GRACE data show a positive gravity anomaly rate in the area where post-glacial rebound is expected. We use the maximum value of that signal to compare with the GIA models. Several factors contribute to the uncertainty in the observed gravity rate in the center of the Barents Sea. Formal errors in the GRACE data are estimated assuming that the geophysical signals are explained by an annual signal, a semi-annual signal, and a trend (*Wahr et al.*, 2004). The residuals are upscaled to account for the reduction in noise after removing a trend and annual signal from a random time series. Systematic errors result from error in the present-day ice melt estimates including the GIA correction. Assuming that the formal errors are independent from the systematic errors, uncertainty components are added in quadrature to obtain the total uncertainty estimate for the GRACE derived GIA gravity rate. The total (2σ) uncertainty in the GRACE gravity-change observations is shown as error bars in Figures 5.2a and b.

5   Results

In Figures 5.2a and b, the maximum gravity rates from the different GIA models are compared with the maximum gravity rate derived from the corrected GRACE observation for different settings of the bandpass filter. The GRACE derived gravity rate is smaller than the GIA model result using ICE-5G and ICE-6G. The regional ice models with the late-deglaciation chronology mostly overestimate the GRACE-derived maximum gravity rate in the Barents Sea region. Only four of the late deglaciation models fall completely within the uncertainty of the GRACE observations, irrespective of the filter settings. Many of the early deglaciation models pass the GRACE gravity-rate criterion. However, some tend to underestimate the gravity rate in the region. Misfit

with respect to RSL, GPS uplift, and GRACE observations per individual ice model are shown in the supplementary material.

To examine which characteristics of the ice model cause mismatches with the GRACE derived gravity rate, Figures 5.2c and d illustrate the ESL through time for the different models. The overestimation in the late-deglaciation ice models (including ICE-5G) is a combination between time of melting and the overall ice mass in the region. Only models that have no more than 5.1 mESL during 18-21 ka pass the GRACE criteria: nn43772, nn44901, nn45283, and nn96597 (see supplementary material for numbering). The ice models that fit the GRACE data have less than 4 mESL ice volume at 16 ka and have relative small ice volumes during the 20-30 ka interval.

The early-deglaciation models have a tendency to underestimate the gravity change. As a result of the earlier deglaciation onset, these models can have more ice volume during the LGM while maintaining consistency with GRACE. The model nn54867 has an ice volume of more than 6.2 mESL at 20 ka and still fits the GRACE data. Additionally, early-deglaciation models that pass the GRACE criterion have at least 5.2 mESL of ice at LGM.

Early-deglaciation models that have ice volume continuously above 4 mESL during the 20-30 ka period show a different behaviour. By inspecting Figure 5.2d, a small number of the lowest ice volume early-deglaciation models pass the criterion. Model nn55917 does not pass the criterion even though it has less ice (5.78 mESL) than the early-deglaciation model with the most ice mass during LGM. Finally, ICE-6G is also an early-deglaciation model, but has thick ice in the Barents Sea region around 30 ka, which explains the large overestimation of the gravity-change. This suggests that GRACE is sensitive to ice mass change in the 20-30 ka period.

To further asses the constraint to GIA modelling provided by the GRACE data in the Barents Sea, we examine how much the rheology should change, such that the ice models become acceptable. The upper mantle viscosity is varied from 2, 4, 8, 16 to 32 $\times 10^{20}$ Pa s. The lithosphere thickness is varied between 40 and 160 km with a step size of 20 km. The size of the Barents Sea ice-sheet is too small for the uplift to be sensitive to the lower mantle viscosity (*Steffen and Kaufmann*, 2005); therefore, we keep this parameter fixed at 32×10^{20} Pa s to approximate the VM5a structure.

Figure 5.3 shows the misfit results for the following ice models: ICE-5G, two late-deglaciation models (minimum and maximum overall ice mass), two early-deglaciation models (minimum and maximum overall ice mass) and a third early-deglaciation ice model with large amount of ice (more than 4 mESL) in the 20-30 ka period. The misfit region with 95% (2σ) confidence from the minimum misfit (red dot) is denoted by the grey shading (misfit values below 5.99 (*Press et al.*, 1992)). The VM5a structure, used in the previous part, is denoted in blue. All six results show that GRACE is not able to distinguish between different lithosphere thicknesses in the Barents Sea.

To enable the ICE-5G model to pass the GRACE criterion, a smaller upper-mantle viscosity is required to account for the large ice volume. The smaller upper-mantle viscosity will result in a faster rebound and results in smaller current gravity change, due to the fact that most of the relaxation has finished. The opposite effect is seen with the minimum ice-volume model nn44901, where a larger upper-mantle viscosity is needed, such that there is still enough current gravity change present. The best fitting

rheology for the late-deglaciation model (maximum overall ice mass) and ICE-5G has an upper mantle viscosity of 4×10^{20} Pa s. This is similar to the regional upper mantle viscosity estimate of *Steffen and Kaufmann* (2005). The early deglaciation ice models show a more consistent behaviour. Here, best upper-mantle viscosities have a clear lower limit of 4×10^{20} Pa s. Overall, the ice model with maximum ice mass during LGM (nn54867) constrains the upper mantle viscosity to be between $4\text{-}5 \times 10^{20}$ Pa s.
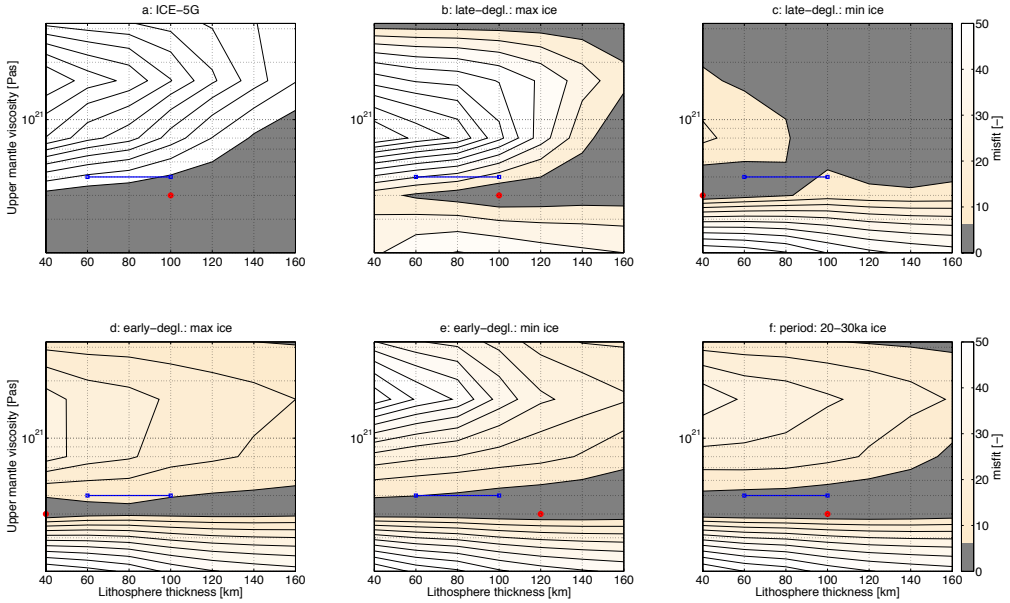
Figure 5.3: The misfit values from the comparison of the GIA model with different ice loading histories to the corrected GRACE observations. The red dot denotes the minimum misfit with a confidence region (2σ) illustrated by the grey area. The different ice loading histories are: (a) ICE-5G (global ice model), (b) Ice model nn44195 (maximum ice volume, late deglaciation), (c) Ice model nn44901 (minimum ice volume, late deglaciation), (d) Ice model nn54867 (maximum ice volume, early deglaciation), (e) Ice model nn55778 (large ice volume at 20-30 ka, early deglaciation), and (f) Ice model nn56597 (minimum ice volume, early deglaciation). The VM5a viscosity profile is illustrated by the blue dots.

Concluding remarks

The increasing timespan of the GRACE gravity-change observations now permits the use these observations for GIA studies of the Barents Sea region. After filtering and correcting for present-day ice melt, GRACE data show a positive gravity-change where GIA is expected. Estimates of the systematic error introduced by correcting for present-day ice melt and for formal error demonstrate that the positive signal is significant.

The global ice-loading models ICE-5G and ICE-6G overestimate the observed gravity change in the Barents Sea region. The regional ice loading models, which contain

less ice mass, predict a gravity rate that is closer to the GRACE derived result. The late-deglaciation chronology models mostly overestimate the observed gravity change. GRACE is therefore able to add new constraints to the ice-mass histories:

- Late-deglaciation ice loading models with less than 5.1 mESL during LGM pass the GRACE criterion.

- Early-deglaciation ice loading models with more than 5.2 mESL during LGM pass the GRACE criterion.

Our rheological sensitivity study indicates that the late deglaciation ice models can be made to fit the GRACE data by lowering the upper-mantle viscosity to 4×10^{20} Pa s, similar rheological changes are needed for ICE-5G. The early deglaciation chronology ice-sheet models result in a clear lower limit of the upper-mantle viscosity of 4×10^{20} Pa s.

To explain the inferred 120-130 m sea level rise since LGM, the total volume of the LGM ice sheets in global models needs to increase. Our results show that it is difficult for the Barents Sea to be a candidate for missing ice. The regional ice models that better fit the GRACE gravity change, contain approximately 2 mESL less overall ice mass in the Barents Sea region than the global ICE-5G and ICE-6G models. GRACE observations constrain the maximum ice thickness to be thinner than predicted by these ice-loading histories with the VM5a Earth rheology. Otherwise the upper-mantle viscosity needs to be lowered with respect to the VM5a viscosity profile that was used to infer ice thickness from RSL constraints. ICE-5G and ICE-6G regional RSL fits would then need to be re-examined. In summary, the GRACE data distinguishes between ice-loading histories that fit the RSL and GPS uplift data and therefore offers new constraint on the deglacial evolution of the Barents Sea region.

Concluding remarks

"The RULES
1 Things fall apart, but centres hold
2 Everything moves in curves
3 You get balls
4 Big balls tell space to bend
5 There are no turtles anywhere"

– Ponder Stibbons in The Science of Discworld by Terry Pratchett, Ian Stewart, and Jack Cohen, (EBURY PRESS, 1999)

The increased resolution and availability of global gravimetric observations have provided new opportunities to study the lithosphere and upper mantle of the Earth. This dissertation discusses several new applications of global gravity field models. Three methodologies are developed in this dissertation that use global gravity modelling, where the spectral content of the dataset plays a crucial role. First, an improved forward modelling methodology, the Fast Spectral Methodology (FSM), is presented in Chapter 2. The improvement lies in the modifications made to the FSM in Chapter 2 that enable it to model deeper mass structures than previous versions of the FSM (*Rummel et al.*, 1988; *Balmino*, 1994). Second, I present a lithosphere isostasy model to compensate crustal masses in Chapter 3 and 4 that better approximates the global spectral content of Earth's gravity field than simple isostasy models used frequently. Finally, a study using gravity-change data from the GRACE mission in the Barents Sea Region is presented in Chapter 5. I show that it is possible to use the GRACE data to constrain the Weichselian ice sheet in the Barent Sea Region after applying corrections to the data. These corrections are developed using spectral analyses of the gravity signal.

Chapter 3, 4, and 5 approach the issue of using global gravity datasets in geophysical studies of the subsurface, in particular for the lithospheric and upper mantle. These studies are a step forward in geophysical research aiming to construct a model of the upper mantle that complies with seismic observations, gravity data, and rheology that fits to GIA constraints. More detailed conclusions in the individual studies are discussed in the following subsections. The effect of GIA in the static gravity field is studied (Chapter 3). I show that due to uncertainty in crustal structures, it is not possible to use the static global gravity field in constraining GIA models better than conventional observations of GIA like geophysical constraints or GPS uplift measurements. Global gravity models do prove to be especially powerful in determining lateral density variations in the lithosphere (see Chapter 4). Furthermore, the long-period dataset of the GRACE mission is able to constrain ice loading histories in the Barents Sea Region (Chapter 5). By applying the new methodologies, I have obtained new insights in GIA and lithosphere research.

6.1   Forward gravity field modelling

I found that a correction (Section 2.4) was needed to keep the binomial series approximation convergent and therefore making the FSM able to compute gravity for density structures at any depth. Numerical tests were constructed to evaluate the accuracy of the topographic mass-to-gravity conversion. Section 2.3.2 confirmed findings by other studies that estimated similar uncertainties (*Martinec et al.*, 1989; *Rummel et al.*, 1988; *Balmino*, 1994). However, the FSM methodology was not suitable for deeper mass layers. Deeper mass layers showed modelling errors, that could easily be interpreted as density anomalies in the mantle. This already happens for crustal layers of CRUST1.0, as I showed in Figure 2.7. Due to the nature of this error, people who forward model CRUST1.0 could interpret these errors as upper mantle anomalies. This particular error was not noticed by other studies, because the FSM was only used for topographic and isostatic mass layers (*Rummel et al.*, 1988; *Vaníček et al.*, 1995). In this thesis, a more elaborate analytical study led to the development of a modified FSM. Section 2.5 showed that the FSM can successfully model forward a density structure in Earth's subsurface with similar accuracy (maximum differences <4 mGal) to the spatial approach (*Kaban et al.*, 2010).

The largest difference between the methodologies used in the benchmark was the approach to model the volume of the mass layer. The spatial method approximates the layer with tesseroids (*Uieda et al.*, 2013). The FSM approximates the mass function with spherical harmonic functions, which are smooth functions. A coarse grid introduces large differences between both methods (Figure 2.6). After increasing the resolution of the grid spacing in the spectral method, to better approximate the volume of the low-resolution tesseroid grid, gravity anomaly residuals were within 4 mGal. This difference between methodologies was also noticed by *Hirt and Kuhn* (2014) and needs to be taken into account when interpreting gravity models. Due to the high uncertainty in subsurface mass structures, it is still unknown which approach is more suitable to approximate reality best.

Future modifications of the methodology is in the direction of modelling radial density

variation inside one layer. This was introduced in Section 6 by following the approach of *Novák* (2000), who approximated radial density distribution by a polynomial function. The V_P model of the crust below the British Isles and surrounding areas seen in Figure 4.2 of Chapter 4 clearly shows a varying radial density structure that needs to be modelled. The observed gradients in the seismic observations can be approximated in the density models by the polynomial functions. Hence, preserving the high-resolution seismic data, yet reducing the complexity of the models compared to high-resolution depth layers in the *Kelly et al.* (2007) model. You would only need four parameters per location to model the crustal structure: Moho depth, ρ_0, α, and β (see Section 2.6). Other crustal models, like CRUST1.0 (*Laske et al.*, 2013) or EUCrust-07 (*Tesauro et al.*, 2008), reduce the information by introducing 2 or 3 crystalline layers by averaging seismic observations, which might remove significant information about the radial distribution of the density. The suggested approach in Section 6 has not yet been used and tested in the forward-modelling software. The introduction of this feature would increase the capability to model more complex density models.

6.2   Global gravity field modelling and GIA

Chapter 3 showed that it is not possible yet to better constrain viscosity models of Fennoscandia in GIA studies with the use of the static gravity field despite claims in the literature (*Heiskanen and Vening Meinesz*, 1958; *Honkasolo*, 1964; *Balling*, 1980; *Anderson*, 1984; *Marquart*, 1989; *Sjöberg et al.*, 1994). This will be followed by the discussion of the uncertainties and capabilities of estimating density anomalies in the lithosphere using global gravity field models.

The static gravity signal has the potential to resolve the issue of the explained bifurcation in regional viscosity models of Fennoscandia (see Figure 3.6b, or *Schmidt et al.* (2014); *Lambeck et al.* (2010)). Regional GIA observables, like RSL curves, GPS uplift rates, and GRACE gravity change, can not make a distinction between the viscosity models. This observed bifurcation in preferred viscosity models in Chapter 3 is not only regionally applicable to Fennoscandia, but can be seen in North America as well (*Métivier et al.*, 2016). The remaining uplift between the two best-fitting viscosity models differs by 150 m, which is identical to a 20 mGal gravity anomaly according to equation (3.2). So, if the GIA gravity signal can be separated from the other sources, the static gravity anomaly would be another geodetical observation to be used to constrain GIA models. However it is proven in Section 4.1 of Chapter 3 to be difficult to extract the GIA signal from the complete gravity field model, due to overlap of other gravity sources.

This difficulty resulted in a debate on the amount of GIA gravity signal present in the negative anomalies observed in Fennoscandia. Studies of the Fennoscandia area (*Métivier et al.*, 2016; *Schmidt et al.*, 2014; *van der Wal et al.*, 2011; *Lambeck et al.*, 2010; *Davis et al.*, 1999; *Bjerhammar et al.*, 1980) and model B defined in Chapter 3 that used the complete negative anomaly in the static gravity field to explain GIA are inclined to find much higher viscosities in the upper mantle. Viscosity model A from Chapter 3 corresponds to the more conventional viscosity models like VM2 and VM5a (*Peltier*, 1996; *Peltier and Drummond*, 2008). Recently, *Métivier et al.* (2016) concluded that the negative gravity signal in Laurentia in the form of the gravity gradients is mainly due to

GIA. Also there, models with a relative high viscosity (lower mantle viscosity of above 2×10^{22} Pa s) were more inclined to explain the complete observed gravity gradients.

Correlation of the gravity field with observed GIA uplift rate or modeled GIA gravity signals does not yet prove that the complete gravity signal is generated by GIA. Unmodelled crustal (*Anderson*, 1984) and lithosphere structures (Chapter 4), as well as deeper mass anomalies (*Forte*, 2007; *Shahraki et al.*, 2015) could have a similar gravity signal as GIA. Therefore, it will always be necessary to reduce other sources from the gravity observations to be able to use the data for GIA studies. As I showed in Chapter 3, the dynamic signal, such as GIA, could be separated from the observations if the complete isostatic lithosphere anomaly can be determined. However, the uncertainty in crustal models is still too large to separate GIA gravity signals from observations. In Laurentia *Métivier et al.* (2016) used CRUST1.0 and different isostatic models to remove the isostatic-crustal signal. Unfortunately, the difference between crustal models is significant in the static gravity field (see Figure 3.11), which could be incorrectly interpreted as the GIA signal.

Another approach to separate gravity sources I studied in Chapter 3 is separation by truncation of spherical harmonic coefficients. By inspecting different GIA models of the Fennoscandia region, I found that almost all of the resulting static gravity signal of GIA models can be represented by the spherical harmonic coefficients 4-45. Spherical harmonic truncation of the gravity models is often used to separate deep mantle effects from more shallow gravity signals (*Bowin*, 1991) as discussed in Chapter 1. However, this simple truncation is not sufficient to decouple deep mantle from GIA gravity signal. In contrast to the spectrum of the isostatic lithosphere model, a clear overlap in spectral signature is seen between GIA and mantle convection model in Figure 3.9. So, to separate the GIA gravity effects from deep mantle sources, I suggest, instead of truncating the spherical harmonics coefficients, to model these sources, such that they can be reduced from the observations.

Previous studies explained the long-wavelength regime of the gravity field with subducting slabs (*Hager*, 1984) and lower mantle structure (Hager et al., 1985). The long-wavelength anomalies are believed to have high correlation with subduction zones and the distribution of hotspots (*Bowin*, 1991), which have their origin in the lower mantle (*Ricard et al.*, 1988). Other models try to find correlation between V_S tomography and the long-wavelength geoid (*Forte et al.*, 1993), but a precise explanation of the long-wavelength regime was not obtained by the different tomographic models (*Panasyuk*, 1998). Also, gravity gradients observed by the GOCE satellite show strong correlation with old subduction zones (*Panet et al.*, 2014). Some argue that a complete model of the mantle convection based on seismic tomography of the mantle must be constructed (*Shapiro et al.*, 1999) to improve our understand of the long-wavelength regime. Many studies (*Tosi*, 2007; *Lay et al.*, 1998) modelled the mantle convection cells and tried to fit to residual gravity anomalies. However, these models are heavily unconstrained due to the unknown viscosity distribution of the mantle. An example of this is given in Figure 3.9. The magnitude of the gravity values was overestimated in a large part of the long-wavelength region for the used mantle convection model (*Tosi et al.*, 2009). The model fits the first 5 degrees of the spherical harmonic coefficients well, but overestimates coefficients degree 6-35. A complete approach was presented by *Métivier et al.*

(2016), who combined the signal from mantle convection, an isostatic lithosphere, and GIA to explain the observed gravity gradient. Their combined approach showed that the gravity signal of mantle convection was smaller than that of the GIA signal in Laurentia. Unfortunately, crustal masses were corrected with the CRUST2.0 model, which is shown in Chapter 3 (Figure 3.11) to differ from newer more sophisticated models of the crust. This could introduce errors in their isostatic lithosphere model.

Another region in the deep Earth that is a candidate for explaining the long-wavelength gravity anomalies would be core-mantle boundary anomalies. Structures at the core-mantle boundary are found to play a role in core and mantle dynamics (*Lay et al.*, 1998). These structures have a large correlation with mantle convection patterns. In seismology this region is called the D" region and is usually explored by long-period shear wave data (*Kendall and Shearer*, 1994). However, there have been attempts to study this region with long-wavelength geoid data (*Čadek and Fleitout*, 2005; *Tosi et al.*, 2009; *Shahraki et al.*, 2015). The lateral heterogeneities above the core-mantle boundary are thought to be caused by the phase transition from perovskite to post-perovskite (*Murakami et al.*, 2004), which would result in density anomalies of less than 0.1 g/cm^3. *Lay* (1989); *Lay et al.* (2006) argued that the lateral structures in this region are a result of plate tectonics and call the region a "plate graveyard". *Spasojevic et al.* (2010) confirm that slab "graveyards" can be responsible for long-wavelength geoid features. From high-temperature and pressure experiments, it has been shown that the composition of subducting slabs can have a higher density than the average mantle density below 720 km depths (*Hirose et al.*, 2005), below which the lithology becomes perovskite-dominant. These experiments provide evidence that subduction of basaltic crust can introduce strong chemical heterogeneity in the lower mantle. *Nakagawa and Tackley* (2005) found that thick post-perovskite layers are typically found in regions where slabs pool above the CMB. They also found that the compositional change affects the seismic velocities more than the temperature variations, except for very long-wavelength structures (first few degree in SH-domain). Others (*Mao et al.*, 2006) have suggested Fe enrichment of the post-perovskite phase due to the influence of the core (*Peltier*, 2007, p.218). After extensive literature study, *Peltier* (2007) suggested that any chemical heterogeneity at the D" region may be entirely core-derived, instead of a "graveyard" of down-going slabs. Future research on the D" and CMB is required in order to compute the percentage of the total long-wavelength potential field that is generated by this layer. Instead of truncating the long-wavelength gravity anomalies, a better approach would be to model the mass structures that are responsible for them, such that an unambiguous gravity-based model of the subsurface can be constructed.

6.3 Global gravity field modelling and lithosphere density

I have studied the effect of the long-wavelength removal by truncating the spherical harmonics coefficients, crustal model uncertainties including V_P-to-density conversion, density background model selection, and lithosphere asthenosphere boundary (LAB) uncertainty on the final estimate of lithosphere densities using global gravity field models.

But before I elaborate on these uncertainties, I would like to discuss some issues about the used isostasy model. In Chapter 4, I improved the isostatic model that compensates crustal density structures, which I have used in Chapter 3 to attempt the separation of the GIA gravity signal from the static gravity field. The improved isostatic lithosphere model is different from the "lithosphere isostasy model" of *Turcotte and Schubert* (1982), because of the fact that I apply this to the complete Earth and not only oceanic regions. *Lachenbruch and Morgan* (1990) used this "lithospheric isostasy model" for the continental region, using thermal expansion to compute the density distributions (*Hasterok and Chapman*, 2007). However, continental lithosphere is much more complicated, due to its long and complex history that can not be captured by simple thermal expansion (*Afonso et al.*, 2016a). So in Chapter 3, I presented a lithosphere isostasy model, where masses are placed between the Moho and a constant depth limit to compensate the crustal mass, for example at 100 km depth. These lithospheric density anomalies are more linked to the crustal structure by isostasy and can relate to thermal and chemical anomalies. This approach is used in studies like *Ebbing et al.* (2007b); *Roy et al.* (2005). Also, *Kaban et al.* (2016) assumed that upper mantle anomalies extended up to 100 km depth, which resulted in 10-25 kg/m^3 density uncertainty underneath the Asian continent.

However, dense cratonic roots are found in the upper 100-250 km depths (*Mooney and Vidale*, 2003). In Chapter 4, I improved the lithosphere density model by introducing a varying lower boundary, instead of using a fixed lower boundary at 100 km depth. The LAB was chosen to be the 1250-1300 °C geotherm, which is believed to represent the boundary between the conducting and convecting mantle (*Artemieva*, 2001). I assumed that the isostatic compensation of the crust can be attributed to the conducting region of the mantle. Subsurface geotherms are best estimated using surface heat flow (*Hasterok and Chapman*, 2007), therefore I have used the LAB model of *Hamza and Vieira* (2012), which uses heat flow measurements to determine this boundary. A problem with a constant lower boundary is that it results in unrealistic densities for thin and thick lithosphere, places where the Moho depth is either shallow (10 km) or deep (70 km). In case of a shallow Moho, such as oceanic lithosphere close to a spreading ridge, a large volume is responsible for the compensation, which results in unrealistic small density anomalies. This introduces an erroneous distinction between density anomalies in oceanic regions and continental regions. There is no evidence that only small density anomalies can exist underneath shallow Moho regions, so the magnitude of density anomalies are underestimated when a fixed compensation depth is chosen. For regions with a deep Moho the opposite behaviour is visible. This is counterintuitive, because in most cases a deep Moho is underlain by a deep LAB (*Durrheim and Mooney*, 1994), and so the compensating masses should be placed in a larger volume. Both issues are resolved by using the laterally-varying LAB as compensation depth instead of using a constant lower boundary. This improved model represents the degree variances (spectral signature) of the gravity field between SH coefficients 20-80 better than topographic isostasy models, comparing for example results presented in *Rapp* (1982) and Figure 4.4. The improved model also enables to estimate realistic lateral density anomalies in the lithosphere using gravity.

Chapters 3 and 4 show that the main source of error in gravity field modelling is

the uncertainty in crustal structures. Similar findings were obtained by *Herceg et al.* (2016). One of the drawbacks of crustal models is that their geometric and density uncertainty is not provided. For example, the global CRUST models are stated without uncertainties. Models that do have uncertainties, i.e. the model from *Kelly et al.* (2007), contain regions with enormous density uncertainties that allow mantle rock densities in sediment layers and sedimentary rock at the Moho. Figure 4.1 shows that the largest uncertainty in V_P/density models is due to the sparsity of data. This explains the huge differences between crustal models found by *Herceg et al.* (2016); *Kaban et al.* (2004) and in Chapters 3 and 4.

Lithosphere density variations underneath the British Isles and surrounding areas are ± 100 kg/m^3. The lateral density variations that I find in Chapter 4 are of the same order and are common in the lithosphere. Underneath the Siberian Craton *Herceg et al.* (2016) find density anomalies of $\pm$ 70 kg/m^3. *Kaban et al.* (2016) find similar density anomalies in the Asian lithosphere. Also, the lithosphere beneath the Barents/Kara Sea region shows density anomalies of ± 200 kg/m^3 (*Ebbing et al.*, 2007b). In the European upper mantle density anomalies of ± 15 kg/m^3 are found (*Tesauro et al.*, 2009) and the North American upper mantle estimates of lateral density variations are ± 40 kg/m^3 (*Kaban et al.*, 2014). However, if crustal models are not improved this observed variation of ± 100 kg/m^3 in lithosphere density anomalies cannot be trusted, because the estimated uncertainty introduced by crustal models is ± 110 kg/m^3. Currently it is difficult to determine if the estimated density variations of the lithosphere are due to the realistic effect of composition and temperature or from the uncertainty in crustal structures.

I found a spectral imbalance between gravity-based and tomographic-derived lithosphere density estimates. This was to be expected, because the data coverage is not homogeneous and therefore regularisation is used to produce the tomographic models (*Cobden et al.*, 2012). Seismic velocity anomalies are elongated along the ray bundles causing the testimated anomalies to be smeared over a larger region (*Foulger et al.*, 2013). The consequence is that a global tomographic model has less signal power in the shorther wavelengths, despite the fact that the observational resolution is sufficient. This will result in density anomalies constructed with typical conversion factors of $\pm$ 35 kg/m^3, instead of the $\pm$ 100 kg/m^3 from the gravity-based solutions (see Figure 4.11). This spectral imbalance between tomographic models and gravity-based lithosphere density estimates needs to be taken into account, because otherwise it is difficult to combine both datasets to produce a joint model of the lithosphere. To counter this imbalance, the gravity-based density models were filtered in Section 4.6 with a Gaussian filter resulting in similar spectral appearances between gravity-based and tomography-derived lithosphere densities. The best filter in this case study was a Gaussian filter with a half width of 200 km. The difference between the density anomalies of the filtered gravity models is smaller than when the unfiltered solutions are compared with seismic-derived estimates. Studying the effect of the regularisation in seismic tomography might be a step forward in combining gravity-based with tomographic-derived lithosphere density results. Further investigation should be made into the filtered solutions and their relative uncertainty.

Finally, the lateral conversion factor explained in Section 4.6 and showed in Figure 4.12 can give insight in compositional and temperature influences in the lithosphere. By

decoupling the thermal from the compositional effects in tomographic models, it is possible to have more realistic 3D rheology models. For example, GIA models that use a 3D rheology need the temperature state of the mantle to compute effective viscosity (*van der Wal et al.*, 2013). Also, mantle convection studies need the rheological parameters of the mantle to compute dynamic topography (*Tosi et al.*, 2009). The lateral conversion factor is of interest, because temperature influences have a negative value for the conversion factor (*Karato*, 2008), whereas compositional influences can produce both positive and negative factors, related to particular rock composition. For example, *Shapiro et al.* (1999) found that a simple temperature-dependent-only conversion between shear wave velocity and density for continental lithosphere is not sufficient and compositional effects need to be taken into account. *Cammarano et al.* (2003) state that the effect that composition has on the conversion of seismic data to viscosity is secondary to the temperature contributions. The density-velocity ratios are most indicative to compositional variations, but they have large uncertainties. Similarly *Trampert and van der Hilst* (2005) find compelling evidence of the influence of compositional anomalies in the seismic wave velocity and identified constraints on mass density to discriminate between thermal and compositional effects. This means that gravity studies will be useful for the compositional state of the mantle. The lateral conversion factor shows a variation of ± 0.5, which indicates significant compositional influences in the lithosphere. A map of the lateral variation of the conversion factor in the lithosphere could help improving rheological 3D modelling for GIA studies and many other studies of the subsurface by distinguishing between thermal and compositional anomalies.

Knowing that the crustal models are the limiting factor, how to continue from here? Gravity gradients are most sensitive to crustal structures (*Martinec*, 2014; *Martinec and Fullea*, 2015). Results from the ESA's GOCE mission emphasised the importance of gravity gradients in geophysical modelling (*Bouman et al.*, 2016). *Ebbing et al.* (2013) show the additional benefits of using gravity gradients in lithospheric modelling. Namely, gravity gradients at satellite altitude are less sensitive to near-surface geological structures with subtle density contrasts than geoid and gravity observations on the ground (*Ebbing et al.*, 2014). The gravity gradients at satellite height focus on the global structure of the area, but are less affected by mass sources outside the area than geoid and gravity anomalies. Also, *Bouman et al.* (2016) discuss that satellite gravity gradients should be used to improve the modelling of lithosphere structures. Satellite gravity gradients are used in the construction of a lithosphere model of the Arabian Peninsula (*Holzrichter and Ebbing*, 2016). Despite this, sub-lithospheric structures, like a subduction slab, can have a significant impact on the estimated lithosphere model derived from gravity gradients (*Fullea et al.*, 2015). Although satellite determined gravity gradients do not solve the problems that occur with conventional gravity models, the final model of the subsurface will be more robust.

6.4   Gravity change and GIA

For the first time, I showed that GRACE gravity change data can also be used to study the ongoing GIA in the Barents Sea. GRACE data has not been used to study GIA in the Barents Sea Region, because the ongoing gravity change in that area was expected

to be too small to be useful to constrain geophysical modelling (*Steffen et al.*, 2008). The potential GIA signal in the Barents Sea is completely removed from the GRACE data when a Gaussian filter with a halfwidth of 400 km is used, a filter that is used for example in Fennoscandia (*Steffen and Wu*, 2011). Therefore, a new approach had to be developed to extract the GIA signal from the GRACE data. I determine similar ice mass losses compared to *Jacob et al.* (2012) for the Barents Sea islands Svalbard (-3.3±1.2 Gton/y), Novaya Zemlya (-4.2±1.0 Gton/y) and Frans Joseph land (-0.9±0.7 Gton/y). The uncertainty estimates of the ice mass changes are smaller than in *Jacob et al.* (2012), but similar to *Schrama et al.* (2014). Furthermore, the correction showed that the resolution up to degree and order 60 of the ice melt mass model introduces positive gravity anomaly in the center of the Barents Sea. When this effect is not taken into account a too large part of the gravity signal could be taken interpreted as GIA response of the LGM ice sheet. Not only this effect will reduce the amount of gravity signal responsible for GIA, also long wavelength signals from Greenland and hydrology are influencing the observed gravity effect and need to be taken into account. Depending on the chosen ice melt correction and filter settings, only a maximal value of 0.23 μGal/yr in the GRACE data can be attributed to GIA response (see Figure 5.2).

The corrected GRACE gravity observations are able to improve constraints of historic ice loading models of the Barents Sea ice sheet after modelling of the current ice melt and filtering of long wavelength signals. The GRACE data is sensitive to the thickness of the ice sheet during LGM. Figure 5.2 shows that the variation of GIA signal due to the range of ice loading models (grey lines) is larger than the uncertainty of the GRACE estimate (solid blue lines with error bars). I constrain the ice mass (in Equivalent Sea Level change) to be 5-6.3 m ESL using the GRACE data. However, global ice loading models ICE-5G and ICE-6G overestimate the ice mass in the Barents Sea region. The study shows that a new ice loading model that is robust should also be able to match the GRACE data, due to its sensitivity to the GIA signal at the center of the Barents Sea Region, and not only the conventional observations, such as RSL curves and GPS uplift velocities.

There is still a debate on the onset of deglaciation of the LGM ice sheet in the Barents Sea (pers. comm. John-Inge Svendsen (2015)). The timing of maximum extension of ice sheets (often called LGM for the last maximum) is not similar for different sections of the ice sheet (*Hughes et al.*, 2016). For example, the ICE-5G model estimates the Barents Sea LGM to be at 26 ka, whereas the regional model of *Tarasov et al.* (2012) estimates it at 17-19 ka. Raised shorelines on Svalbard even indicate that the major ice retreat in the western Barents Sea only commenced after 13 ka (*Lambeck*, 1996). I use two types of ice sheet histories (*Tarasov et al.*, 2012) for the Barents/Kara Sea Region in this study: early-deglaciation (onset around 19 ka) and late-deglaciation (onset around 17 ka), as also depicted in Figure 5.2c and d. These models all explain the geologic and geodetic observations of the GIA response, but still experience significant difference in deglaciation history. In Chapter 5, I show that the GRACE data favours the early-deglaciation models, which results in the possibility of more ice mass at LGM than with late-deglaciation models. There are some late-deglaciation models that still agree with the GRACE data, where these models estimate significant less ice mass than the early-deglaciation models. Furthermore, the early-deglaciation models are more in line with

a new constructed model of the Eurasian ice sheet (*Hughes et al.*, 2016). This model
is reconstructed from a vast collection of geologic-derived dates constraining ice sheet
advance and retreat and other geomorphological observations. It should even be possible
to reduce the current uncertainty of ice loading models in the Barents Sea with more
precise gravity-change data (longer time series), such as the GRACE Follow-On mission
(*Flechtner et al.*, 2014), which is expected to be launched in early 2018.

There is an imbalance between global sea level observations and models of historical
ice mass (*Clark and Tarasov*, 2014). There is an increasing imbalance of the North
American (*Lambert et al.*, 2006; *van der Wal et al.*, 2009; *Argus and Peltier*, 2010;
Tarasov et al., 2012) and Antarctic (*Ivins et al.*, 2013; *Whitehouse et al.*, 2012) ice sheet
models with observed sea level rise. The Barents/Kara Sea Region has been proposed
as a region for missing ice (*Clark and Tarasov*, 2014). In my study the best fitting ice
loading models with GRACE gravity-change observations in the Barents Sea are also
not able to explain the imbalance, consequentially the global ice-loading models used in
GIA studies need revision.

Chapter 5 explored the possibility to study the rheology underneath the Barents
Sea Region using the GRACE data. Figure 5.3 shows that the GRACE observation is
insensitive to lithosphere thickness in the Barents Sea Region. This particular feature of
the data was also seen in Fennoscandia from the results of Chapter 3. This insensitivity
of the GRACE data for lithosphere thickness was also found by *Steffen et al.* (2010). The
remaining uplift is due to the viscous relaxation of the mantle, which is more controlled
by the viscosity of the mantle and not so much the elastic thickness of lithosphere. In
particular for the Barents Sea, the upper mantle viscosity is the driving parameter,
because of the relatively small size of ice caps during LGM in the Barents Sea Region.
One of the constraints I found is that the upper mantle viscosity in the Barents Sea
Region has a lower limit of 4×10^{20} Pa s, a value that is close to global viscosity model
estimates like VM2 and VM5a (see Figure 3.3). A lower viscosity in the upper mantle
cannot explain the observed gravity change due to ongoing GIA in the region. This
conclusion holds for all the different ice loading models used in Chapter 5. Still, higher
viscosity values in the upper mantle can explain the GRACE observations.

This imbalance could also be explained by the use of imperfect Earth-rheology models
in the GIA studies, resulting in incorrect ice-loading estimates. The global ice models
all rely on laterally-homogeneous Earth-rheology models for the interaction with the
solid Earth. The Barents Sea GIA is also affected by 3D rheology. *Kaufmann and Wu*
(1998) show that a lateral varying viscosity has a significant effect on the estimated GIA
signal, and therefore the 3D structure needs to be taken into account when modelling
the GIA in the Barents Sea Region. The observed difference of upper mantle density in
gravity data between Western and Eastern Barents Sea (*Ebbing et al.*, 2007b) suggests
a possible lateral viscosity difference in the area, because the density difference could be
explained by different thermal conditions. Furthermore, a new model of the 3D structure
of the lithosphere beneath the Barents Sea (*Klitzke et al.*, 2015) shows a highly variable
structure that could have impact on the estimated location of the GIA geometry gravity
change signal. Therefore, new studies of GIA in the Barents Sea need to account for
this 3D structure, because the Earth response affects the observed sea level change and
current gravity change.

Epilogue: Changing Perspective on Gravity

> *"In reviewing the history of geodesy three eras can be distinguished, the "spherical," the "ellipsoidal," and the "geoidal.""*

– Heiskanen and Vening Meinesz, *The Earth and its gravity field, (McGraw-Hill Book Company, 1958)*

During my time as a PhD candidate, I have grown great interest in the work of Prof. Vening Meinesz, who is a key figure in physical geodesy and geophysical gravity studies. I was part of a project team that investigated the scientific and cultural heritage of this fascinating professor and his work conceived by the TU Delft Library. To honour this research on Vening Meinesz I decided to write the following epilogue on the historical perception of gravity and the role Vening Meinesz has played in it.

Gravity as a constant

Let us start with the earliest ideas in human history about gravity. In ancient times people were already fascinated by the motion of objects. The archer in the Roman legion needed to know where his arrow would hit. By studying the stars one could better predict the seasons, improving the output of crops. Gravity dominates in both these fields of physics: dynamics and astronomy. Antique literature contains several comments on the idea of gravity. The teachings of Aristoteles (*Ross et al.*, 1908) discussed that the nature of objects was to be at the centre of the world. Therefore, they would fall down, trying to get to this center due to their inner *gravitas* or heaviness.

A particularly interesting and controversial thinker was John Philoponus (c. 490 - c. 570 AC), a theologian, excelling in mathematics (*Chadwick*, 2013) who was condemned by the Church because of his unorthodox views (*Schmitt*, 2013). In his publication, *Commentaria in Aristotelem Graeca*, he criticised Aristoteles' views on space, void, and the explanation of projectile motion with theories that resembled current knowledge. His

work only became available to Western philosophers in the sixteenth century. Before
this time, his theories were far from widespread in the Western countries, despite being
well-known in the Arabic academic circles. Unfortunately, Philoponus was one of only
a few contrasting influences with respect to the teachings of Aristoteles in Europe. The
teachings of Aristoteles would dominate science in the Middle Ages.

During the start of the sixteenth century, a few philosophers started to contradict
his teachings, running the risk of being excommunicated by the church, or worse. As-
tronomers measured the motions of planets and tried to develop theories that explained
the planets' trajectories through the sky. In particular, Copernicus (1473-1543) studied
the work of Ptolemy, work that was well respected in the Roman Church (*Sobel*, 2011),
but found critical errors with respect to his own observations of the motions of the plan-
ets. Copernicus found that if he envisioned the Sun as the centre of the universe, the
motion of the planets could be predicted more accurately than by Ptolemy's theories,
who considerate a geocentric world view. He published his ideas in *On the Revolutions
of the Heavenly Spheres* (1543). Copernicus was not aware of any theory in which the
Earth moves, instead of the Sun. This was already proposed by Aristarchus of Samos in
the third century *B.C.*, but Aristarchus had not yet been available to the Latin-reading
community (*Sobel*, 2011, pp. 181). In Scania (then part of Denmark, now Sweden),
Tycho Brahe (1546-1601) made many astronomical observations that would become a
milestone in the history of science. Brahe did not believe the Copernican system. Nev-
ertheless, his assistant Johannes Kepler (1571-1630) would develop the laws of motion
for the objects around the sun, using many dedicated observations of the sky, sun, and
planets. Kepler adopted the Copernican system and further refined it. The famous laws
of Kepler would prove to be valid for any planet, and could predict their motion through
the night's sky.

Around the same time, an Italian astronomer named Galileo Galilei (1564-1642)
fully adopted the Copernican heliocentric world view and was aware of the teachings
of Philoponus. He defended the heliocentric world view in his publication "Dialogue
Concerning the Two Chief World Systems" (1632). Galileo is famous for his experiment
on top of the Leaning Tower of Pisa. In his publication "Two New Sciences" (1638),
Galileo hinted at the fact that he had dropped proof masses from a tower to disprove
the theorem of Aristoteles. However, many historians argued that the experiment of
Galileo was a thought experiment (*Graney*, 2012). Besides, it was not Pisa but the
city of Delft in the Netherlands that was the setting for this famous experiment. In *De
Beghinselen der Weeghconst* (1586) it is documented that Simon Stevin (1548 - 1620)
performed the famous experiment concerning gravity and falling objects. Simon Stevin
went up the church of Delft together with Jan Cornets de Groot, father of Hugo de
Groot (a famous Dutch writer and lawyer), and dropped two lead balls with different
masses, and concluded that they both fell to the ground within the same time. This
experiment disproved the theory of gravitas by Aristoteles, who stated that objects
with more gravitas (mass) would fall faster. Simon Stevin wrote the following in his
publication:

> Laet nemen (soo den hoochgheleerden H. IAN CORNETS DE GROOT
> vlietichste ondersoucker der Naturens verborghentheden, ende ick ghedaen
> hebben) twee loyen clooten d'een thienmael grooter en swaerder als d'ander,

>die laet t'samen vallen van 30 voeten hooch, op een bart oft yet daer sy merck-
>elick gheluyt tegen gheven, ende sal blijcken, dat de lichste gheen thienmael
>langher op wech en blijft dan de swaerste, maer datse t'samen so ghelijck
>opt bart vallen, dat haer beyde gheluyden een selve clop schijnt te wesen.
>S'ghelijcx bevint hem daetlick oock also, met twee evegroote lichamen in
>thienvoudighe reden der swaerheyt, daerom Aristoteles voornomde evere-
>denheyt is onrecht.[1]

The old Dutch text could be the inspiration for Galileo's work on gravitational attraction.

During the 16th and 17th centuries, scientific debate was among others preoccupied with gravitational acceleration. With the concept of gravity becoming more clear, people started to envision how to measure its 'quantity'. The earliest published results of measuring the numerical value of the gravitational acceleration can be credited to Giovanni Battista Riccioli (1598-1671). Riccioli, in his *Almagestum Novum* (1651) gave a thorough review of the existing ideas about acceleration, and also performed the experiment of dropping proof masses from a tower, trying to disprove Galileo. Riccioli documented the results of his experiment of the motion of an object in free-fall. For his experiment, he dropped an object from the Asinelli Tower (98.37 m) in Bologna (see Figure 6.1), and then timed the fall with his calibrated pendulums (*Graney*, 2012). He documented all the parameters and observations of the experiment, but did not calculate the value of the gravity acceleration, g. Yet, because of his meticulous documentation of all the experimental data, it is possible to deduce a value of g: 29.8 ± 0.7 Rmft/sec, which in modern-day units would be 9.36 ± 0.22 m/s^2, about 5 % off from the true value. This is quite remarkable considering the poor timing instrumentation of Riccioli.

Instead of observing a falling proof mass, one could also measure the local gravity by determining the period and length of a pendulum. This approach would save the experimenter to walk up and down the staircase of the drop tower after each test. The English philosopher and scientist Francis Bacon (1561-1626) is thought by Voltaire to be the first to propose the use of a pendulum clock to measure gravity, and to see if gravity would be different on top of a mountain, compared to the gravity in a deep mine (*Voltaire*, 1733). Unfortunately, no records have been found of him performing this experiment. Christiaan Huygens (1629-1695) published his *Horologium Oscillatorium sive de motu pendulorum* (1673) in which he described his famous theory about the motion of a swinging pendulum, which linked the value of gravity to the period of the pendulum. He determined the value of gravitational acceleration with his pendulum clock, obtaining g = 30'2"/sec, which is 9.2 m/s^2. Coincidentally, at the same time during an expedition to Cayenne to determine Martian parallaxes (1672-1673), the astronomers Jean Richer and Jean-Félix Picard discovered that a one-second pendulum calibrated in Paris needed to be shortened in order to regain oscillations of one second (*Torge*, 1989, pp. 7). E. Halley confirmed this by comparing pendulum measurements in St. Helena

---

[1]English translation: "Let us take (as the highly educated Jan Cornets de Groot, the diligent researcher of the mysteries of Nature, and I have done) two balls of lead, the one ten times bigger and heavier than the other, and let them drop together from 30 feet high, and it will show, that the lightest ball is not ten times longer under way than the heaviest, but they fall together at the same time on the wooden plank (on the ground), because both thuds sound at the same time. Similar results is found for two bodies similar in size yet ten times heavier, which proves that Aristotle is wrong."

Ordo experimentorum	Vibrationes Simplices Perpédiculi alti vnciam I $\frac{1}{10}$.	Tempus primi Mobilis respondens Vibrationibus.		Numeri Quadrati Vibrationum.	Spatia côfecta à Globo argillaceo Vnciarũ 8. in fine temporũ.	Spatia seorsim confecta singulis temporibus.	Proportio Incrementi Velocitatis Grauium in Aëre nostrate.
	Vibr. Simpl.	Secũda	Tertia	Quadrata	Pedes Romani	Pedes Romani	Numeri minimi
	5	0''	50'''	25	10	10	·1
	10	1	40	100	40	30	3
I.	15	2	30	225	90	50	5
	20	3	20	400	160	70	7
	25	4	10	625	250	90	9
	6	1	0	36	15	15	1
	12	2	0	144	60	45	3
II.	18	3	0	324	135	75	5
	24	4	0	576	240	105	7
	26	4	10	676	280	40	8 $\frac{1}{2}$
	6 $\frac{1}{2}$	1	5	42	18	18	1
	13 0	2	10	169	72	54	3
III.	19 $\frac{1}{2}$	3	15	381	162	90	5
	26 0	4	20	676	280	118	6 $\frac{7}{18}$

Figure 6.1: (a) Sketch of the Asinelli Tower by Riccioli. (b) Table of the experiments done by Riccioli. (figures were obtained from *Graney* (2012))

and London (1677-1678). These observations hinted at the fact that the value of gravity at the surface of the Earth was not constant.

Gravity revealed the shape of the Earth

Gravity would become essential in determining the shape of the Earth. Christiaan Huygens did not yet state the variation of the period of the pendulum with latitude in the *Horologium Oscillatorium* (*Bell*, 1941). He found that the observations in Cayenne were "very important and constitutes a remarkable property of our pendulum", but was unclear on any conclusions he could draw from these observations at the time. In a later publication, Huygens calculated the flattening of the poles of 1/576 (*Discourse de la Cause de la Pesanteur*, 1690), half the size of the current estimate. This discovery can be argued to be the start of physical geodesy, as it uses measurements of the gravity field to reveal information about the shape of the Earth.

On the 5th of July 1687, Isaac Newton published his most famous work, the *Philosophiae Naturalis Principia Mathematica*, providing the three laws of motion of an object, but also giving a description of the law of gravity. It would become one of the most influential publications in the history of science. Newton stated his gravitational theory as follows:

> Every point mass attracts every single other point mass by a force pointing
> along the line intersecting both points. The force is proportional to the

product of the two masses and inversely proportional to the square of the distance between them. - Isaac Newton (1687)

With the law of gravity Newton was able to describe the observations made by Copernicus and Kepler of the motion of the planets and prove Kepler's laws. Furthermore, he was able to predict the trajectory of projectiles such as arrows, bullets, and cannonballs. From the law of gravitation, Newton proposed an Earth model of an oblate ellipsoid. He based this prediction on the rotation of the Earth, which would result in outward bulging of the equator and flattening of the poles. Therefore, an observer located at the equator is situated a little further from the centre of mass of the Earth than an observer at the poles. The theory of gravitation of Newton then dictates that the acceleration due to gravity is slightly smaller for the observer on the equator. Of course, there is more at play, because also the acceleration outwards due to the rotation of the Earth plays a role. And moreover, the extra mass in the Earth's mantle and the equatorial bulge of the core due to the rotation of the Earth affects the measured gravity. Newton also thought about this issue and estimated the flattening of the Earth to be 1/230 (*Torge*, 1989).

On the other side of the Channel, the French argued that the Earth was flattened at the equator, having a more egg-like shape. This was mainly due to Cassini's work, who divided Picard's famous measurement arc (1669-1670), which was used to determine the size of the Earth to a reasonable degree of accuracy, in two sections to calculate the flattening of the Earth (*Torge*, 1989). To prove one of the two theories, the French sent out two different expeditions to make geodetic arc-distance measurements: one to Peru (modern Ecuador) (1735-1740) by Bouguer and one to Lapland under the leadership of Maupertuis (1736). Despite their successful measurement campaign, they did not like the result because it proved that the English were correct. The physical (Newton, Huygens) approach to geodesy gave the correct result for the shape of the Earth, instead of the geometrical approach (Cassini).

Nevertheless, geometrical geodesy would dominate the 18th and 19th century, as is stated in *Torge* (1989): "The wider application of this 'gravimetric method' suffered from the lack of accurate and well distributed gravity measurements and from the difficulty of reducing the data to the Earth ellipsoid. Such problems were not overcome until the twentieth century." Synthesis between physical and geodetic evidence about the ellipsoidal shape of the Earth came around 1743 and was made by the Clairaut Theorem (1713-1765). This theorem enabled the computation of the flattening of the Earth from gravity measurements at different locations. It was Laplace (1799) who used the theorem for the first time and computed a flattening of the Earth of about 1/330 using 15 gravity observations (*Torge*, 1989). Most of the respectable geodesists at that time were trying to determine the flattening of the ellipsoid of the Earth. Many gravity expeditions on land were held to determine the shape of the ellipsoid. In the late 1800s, the estimated value of the flattening converged to 1/298.257 223 563 (*NIMA*, 1997). The WGS84 ellipsoidal is currently used as the reference frame for the American Global Positioning System (GPS).

Gravity at sea

As the instrumentation and technology developed with time, the gravity measurements on land became more accurate. Geodesists and mathematicians like Laplace (1802), Gauss (1828), Bessel (1837), and others became aware that the variations they saw in the measurements were not noise but physical features in the gravity field. It became clear that local mass anomalies in the Earth's structure and shape could be studied by making gravity observations at the surface. Instead of determining the ellipsoid more accurately geodesists started to map these undulations and called it the geoid. The geoid is defined as the equipotential surface of the gravitational field that describes the undisturbed sea level surface.

During the beginning of 1900s, the Earth's gravity field had only been measured on land. The classical single-pendulum device, like the one from Huygens, needed a stable platform, which was difficult to achieve on ships. The swell and the shaking of the large engines made it impossible to keep the pendulum stable. Therefore, the value of the Earth's gravity field in the oceans was still unknown to the geodetic community. A young civil engineer from the *Technische Hogeschool* in Delft would change this. After his graduation in 1915, Felix Andries Vening Meinesz (1887-1966), son of the mayor of Rotterdam and Amsterdam (Sjoerd Vening Meinesz), was given the task at the *Rijkscommisie voor Graadmeting* to set up the first gravimetric base station network of the Netherlands. For this project he needed a device that could measure the gravity field with the highest possible accuracy, which in those days was a pendulum instrument. Unfortunately, he found the ground of the Netherlands to be very unstable. The waves of the North Sea, when breaking on the dunes of the Dutch coast, would generate solid waves in the ground that affected the motion of the pendulum observed at Delft.

Vening Meinesz changed his location of research to a small town called de Bilt. In particular, he moved to the Royal Dutch Meteorological Institute (KNMI). There, in the basement of the KNMI building at the Kloosterweg, underneath the office of the director of the institute, E. Van Everdingen, Vening Meinesz commenced his thorough calibrations of the new pendulum instrument (*Memorial book*, 1957). Evidence of his presence can still be found at the old KNMI building, where at the west side of the building a historical plaque is present on the left rail of the concrete stairs, marking the historic gravimetric base station. This location was particularly useful for Vening Meinesz, because the geological subsurface made it a very stable environment for gravity observations. Due to the stable soil, ground motions generated by the waves of the North Sea were dampened and the remote location would decrease the oscillation induced by lorries and inland shipping that were more frequent in Delft. This made it possible for the professor to test and calibrate his equipment, resulting in very accurate ($\approx 1 - 2$ mGal) measurements of the gravity field during the professor's expeditions at sea, which would happen in the years to follow (*Vening Meinesz*, 1932-1948).

Due to the success of his work in removing external accelerations from the measurements in the Netherlands, Vening Meinesz decided to try measuring onboard a surface ship in 1921. Unfortunately, the motion of the waves and the shaking due to the steam engine were too severe and the observations were worthless. Vening Meinesz, slightly disappointed, presented his negative results in Maastricht at the 19th Nederlandse Natuur- en Geneeskundig Congres, April 1923. After his presentation, Ir. F.K.Th. van Iterson
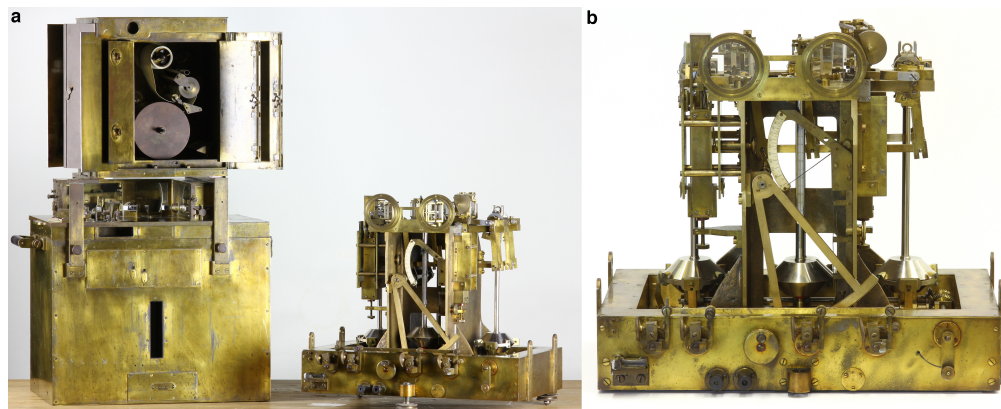
Figure 6.2: The pendulum apparatus of Vening Meinesz, which used the principle of three pendulums to measure the gravity field of the Earth. (a) Disassembled pendulum apparatus with (left) the climate-control and protective casing with the recording apparatus on top and right the pendulum measuring instrument. (b) Front-view of the pendulum instrument. Figures were made by Sander van Dam, TUDelft Library. The submarine crew named Vening Meinesz' pendulum apparatus the "Golden Calf". As the story goes, during the gravity observation all the non-essential personnel had to lie down in their bunk-bed to create a very stable submarine. The Dutch government declared that this was a degradation of personal life and well-being and therefore paid the submarine crew 1 guilder (the currency of the Netherlands at the time) per dive extra wage for compensation. So, when the crew saw the pendulum apparatus carried on board, they cheered because this meant extra wages. Of course, the abundant use of bronze plating will also have influenced the name.

(1877 - 1957), director of the Staatsmijnen, suggested to use submarines instead of surface ships (*van Hengel*, 2014). Wave motion at 30 meters depth would be dampened and submarines use quiet electro-motors when diving. This touch of serendipity would be the start of many submarine gravity expeditions at sea.

In 1921 the gravimetric instrument used in these expeditions was not yet fully developed. Vening Meinesz, being a true engineer, modified the apparatus many times during his numerous submarine voyages, continuously improving the design. During his work on the gravimetric reference network of the Netherlands, he used the Von Sterneck-Stückrath gravimeter (1887), but it proved to be difficult to operate during the long K-II submarine expedition (1923). Vening Meinesz decided to design a new gravimeter, using his experience during this expedition (See Figure 6.2). He "cannibalised" the pendulums of the old Von Sterneck gravimeter (The casing of the old Von Sterneck was still in possession of the KNMI in 2015). Vening Meinesz used the double-pendulum principle of the Von Sterneck gravimeter to acquire high precision. However, his mathematical analyses of the pendulum motion showed that he only needed three pendulums for two independent measurements instead of four (*Vening Meinesz*, 1929). The pendulums were placed in a pair-wise configuration, all swinging in the same direction. Each pair of pendulums would produce an independent gravity observation that allowed Vening Meinesz to determine an average observation and corresponding uncertainty. Vening Meinesz started with the linearised differential equation to describe a pendulum's motion attenuated by

a horizontal acceleration:

$$\ddot{\theta} + \frac{g}{l}\theta + \frac{a_y}{l} = 0$$

The angle of deflection of the pendulum is represented by θ, whereas the length is l and gravity is noted by g. The horizontal acceleration is given by a_y. With one pendulum it is impossible to decouple the value of g from the external accelerations acting on the instrument. Therefore, two pendulums are used, where the difference of their deflection angles is measured. The external acceleration, which is almost the same for both pendulums, is then mitigated since:

$$(\ddot{\theta}_1 - \ddot{\theta}_2) + \frac{g}{l}(\theta_1 - \theta_2) = 0$$

The quantity $\theta_1 - \theta_2$ is observed by an ingenious design of light rays, mirrors and prisms on the top of the pendulum apparatus. This second-order differential equation is easily solved. For small initial amplitudes of the virtual pendulum, this will result in the famous pendulum relation of Christiaan Huygens:

$$T_{1-2} = 2\pi\sqrt{\frac{l}{g}}$$

The period of the virtual pendulum (T_{1-2}) can be determined from the recorded deflections of the pendulums. Light rays were reflected from little mirrors mounted on the pendulum to capture the motion. The recording instrument, a small "dark chamber" with a roll of photographic paper, was situated on top of the pendulum casing. A clockwork-like contraption unrolled the paper during the observations, so that the deflections of the pendulum pair were recorded.

This unrolling of the photographic paper was not accurate enough, so Vening Meinesz designed another approach to accurately determine the time periods of the pendulum. The professor always took state-of-the-art chronometers on board the submarine expeditions. One chronometer, the Nardin 212, was used on almost all of his expeditions and was accurate up to 0.04 sec/day. He asked for alterations to be made to the chronometers, such that they were able to open and close an electrical circuit every 0.5 seconds. This electric pulse was then used to control a shutter in the recording instrument to shortly interrupt the light ray. This resulted in small 0.5 second markings in the final recording sheets, which could be used to determine the time intervals with high accuracy.

During the submarine expeditions, Vening Meinesz kept altering the device to improve its accuracy. The smallest errors to the observations were taken care off. For example, when the submarine dived to 30 meters depth, the pressure of the air inside the enclosed vessel increased, which caused sudden temperature changes of a few degrees. Because the pendulum apparatus was thermally insulated with sheep's wool, the air temperature inside the apparatus did not experience these sudden changes in temperature. However, during the 45 minute long observations, internally the temperature would gradually change. This affected the very sensitive measurements. To mitigate this source of noise, a small electric heater in the bottom of the device was turned on before each dive, heating up the air by a few degrees to simulate the temperature of the air after dive. In this way, there would be no temperature offset between the air in the
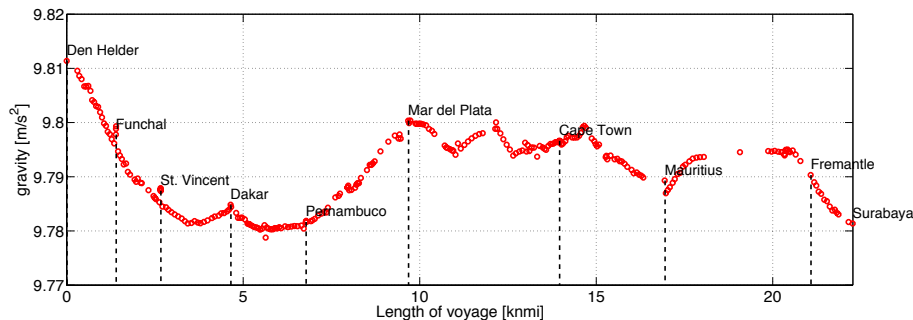
Figure 6.3: The complete collection of gravity measurements done by professor Vening Meinesz during his voyage onboard the submarine K-XVIII from Den Helder to Surabaya. In total 240 observations were gathered along the expedition with his pendulum apparatus.

submarine and inside the pendulum device during the dive. It needed some practice on the side of the operator, but it was effective.
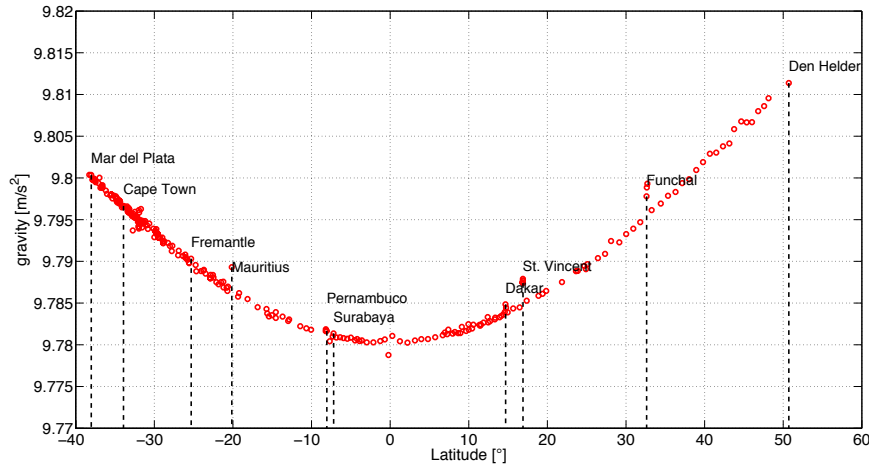
Figure 6.4: The gravity observations of Vening Meinesz aboard the K-XVIII, but now plotted with respect to their position with respect to the equator, or their latitude.

As discussed earlier, the gravity acceleration measured at the Earth's surface is not the same everywhere. This is clear from the measurements done by Vening Meinesz during one of his famous gravity expeditions at sea onboard the submarine Hr. Ms. K-XVIII of the Royal Dutch Navy. During this particular expedition, professor Vening Meinesz obtained 240 measurements of the Earth's gravity field. In Den Helder, the value of g is around 9.81 m/s^2, which is also the value taught in Dutch high-school physics classes. However, the magnitude of the gravity that was observed by Vening Meinesz during his expedition ranges from 9.78 to 9.81 m/s^2. The ellipsoidal shape of the Earth

can be visualised by rearranging the values of the observations. Instead of plotting them chronologically, the observations are plotted with respect to their latitudinal position on Earth in Figure 6.4. The observed parabolic relation in Fig. 6.4 can be attributed to the shape of the Earth, being not perfectly round but flattened at the poles, exactly as many had found before Vening Meinesz (*Torge*, 1989).

Gravity unravelling the subsurface

The gravity observations did show more information about our Earth than solely its ellipsoidal shape. The observations perfectly explained the buoyancy of continents, mountains, and volcanic islands, one of the well-known geophysical theories of Vening Meinesz. Previous researchers hypothesised that these large masses were floating on a liquid mantle, like an iceberg floats in the water. Vening Meinesz envisioned that bending of the solid crust was partially responsible for holding up the mountains. Gravity observations at coastal regions and volcanic islands showed that the crust acted as a plate and experienced elastic bending due to the loading of the extra topography. This theory is now called Vening Meinesz isostasy and is especially successful in explaining the gravity field of volcanic islands in the ocean.

The Golden Calf revealed many secrets of the deep ocean. For example, the gravity signal at the Mid-Atlantic Ridge differs from the gravity anomalies at the famous Vening Meinesz belts (now known as subduction zones). Vening Meinesz found strong negative and positive gravity anomalies situated parallel to the volcanic arc in the East Indies (Indonesia), which could not be explained by isostasy. This indicated a dynamic process along the southwest shore of the East Indies. Similar gravity anomalies were found in the West Indies, where Harry Hess, a young American scientist, was responsible for most of the gravity surveys. Harry Hess is mostly known as the founding father of the geophysical model for the spreading ridge (*Hess*, 1962). Hess' model on the divergent plate boundary can be seen as the first step towards accepting the theory of plate tectonics. Observations on both subsurface structures -the subduction zone and spreading ridge- showed volcanic geology and seismic activity, but because of the different gravity anomalies Vening Meinesz and Harry Hess knew that different geological processes were at play. After their common expedition on the submarine U.S.S. S-48 (1932) (*van Hengel*, 2014), both Vening Meinesz and Hess kept corresponding and became good friends. Vening Meinesz with the Golden Calf was the first to make gravity measurements of a transform fault: the Romanche Trench (at the time theorised to be volcanic craton). Also, the gravitational signatures of subsurface structures like the Walvis Ridge and the Rio Grandes Rise were observed during the submarine expeditions (*Vening Meinesz*, 1932-1948). Up until 1950, the Golden Calf was the only instrument that could measure the gravity field with the highest precision. One of the last scientific expeditions with the instrument was made in 1960 (*Talwani*, 1962), to measure the gravity field in the South Atlantic and Indian Ocean. The instrument was succeeded by the Graf-Askania gravimeter, which was a spring gravimeter on a stable platform (*Graf*, 1958). Overall, the Golden Calf was used in ocean gravimetry for 37 years.

We have come a long way since the theories of the Greek philosopher Aristotle concerning our perception of gravity. Gravity and the advancement in instrumentation

has always gone hand in hand; from the drop tower of Riccioli and pendulum experiments of Huygens to the GRACE and GOCE satellite missions. Vening Meinesz saw the importance of accurate instrumentation in gravity research. With his pendulum device, he opened a fascinating field of research. His precise instrumentation led to new theories about our home planet. One can only dream about the new scientific discoveries that will come from the precise gravimetric instrumentation of the future.

Bibliography

Abramowitz, M. and I. Stegun, editors (1972). *Handbook of Mathematical Functions: with Formulas, Graphs, and Mathematical Tables*, New York, Dover.

Afonso, J.C., M. Fernàndez, G. Ranalli, W.L. Griffin, and J.A.D. Connolly (2008), Integrated geophysical-petrological modeling of the lithosphere and sublithospheric upper mantle: Methodology and applications, *Geochemistry Geophysics Geochemistry*, 9(5), 1–36.

Afonso, J.C., J. Fullea, W.L. Griffin, Y. Yang, A.G. Jones, J.A.D. Connolly, and S.Y. O'Reilly (2013a), 3-D multiobservable probabilistic inversion for the compositional and thermal structure of the lithosphere and upper mantle. I: a priori petrological information and geophysical observables, *Journal of Geophysical Research: Solid Earth*, 118, 2586–2617.

Afonso, J.C., J. Fullea, Y. Yang, J.A.D. Connolly, and A.G. Jones (2013b), 3-D multi-observable probabilistic inversion for the compositional and thermal structure of the lithosphere and upper mantle. II: General methodology and resolution analysis, *Journal of Geophysical Research: Solid Earth*, 118, 1650–1676.

Afonso, J.C., M. Moorkamp, and J. Fullea (2016a), Imaging the lithosphere and upper mantle: Where we are at and where we are going, *Integrated Imaging of the Earth: Theory and Applications, Geophysical Monograph 218*, First Edition.

Afonso, J.C., N. Rawlinson, Y. Yang, D.L. Schutt, A.G. Jones, J. Fullea, and W.L. Griffin (2016b), 3-D multiobservable probabilistic inversion for the compositional and thermal structure of the lithosphere and upper mantle: III. Thermochemical tomography in the Western-Central U.S., *Journal of Geophysical Research: Solid Earth*, 121, 1–34.

Airy, G.B. (1855), On the computation of the effect of attraction, *Philosophical transactions of the Royal Society of London*, 145, 101–104.

Al-Kindi, S., N. White, M. Sinha, R. England and R. Tiley (2003), Crustal trace of a hot convective sheet, *Geology*, 31(3), 207-210.

Amante, C. and B.W. Eakins (2009), ETOPO1 1 Arc-Minute Global Relief Model: Procedures, Data Sources and Analysis. NOAA Technical Memorandum NESDIS NGDC-24. *National Geophysical Data Center*, NOAA.

Amelung, F. and D. Wolf (1994), The incremental gravitational force in models of glacial isostasy, *Geophysical Journal International*, 117(3), 864–879.

Anderson, A. J. (1984), Geophysical interpretation of features in the marine geoid of Fennoscandia, *Marine Geophysical Researches*, 7, 191–203.

Argus, D.F., W.R. Peltier, R. Drummond, and A.W. Moore (2014), The Antarctica component of postglacial rebound model ICE-6G_C (VM5a) based upon GPS positioning, exposure age dating of ice thicknesses, and relative sea level histories, *Geophysical Journal International*, 198(1), 537–563.

Argus, D.F. and Peltier, W.R. (2010), Constraining models of postglacial rebound using space geodesy: a detailed assessment of model ICE-5G (VM2) and its relatives, *Geophysical Journal International*, 181, 697–723.

Aristotle, W.D. Ross, and J.A. Smith(1908), The works of Aristotle: Translated into English under the editorship of W.D. Ross, *Oxford Clarendon Press*, 9, 1–290.

Artemieva, I. (2001), *The Lithosphere: an Interdisciplinary Approach*, *421* pp., Cambridge Univ. Press.

Artemieva, I., and H. Thybo (2013), EUNAseis: A seismic model for Moho and crustal structure of Europe, Greenland, and the North Atlantic region, *Tectonophysics*, *609*, 97–153.

Artemjev, M.E. and M.K. Kaban (1994), Density inhomogeneities, isostasy and flexural rigidity of the lithosphere in the Transcaspian region. *Tectonophysics*, 240, 281–297.

Astakhov, V. (1998), The last ice sheet of the Kara Sea: terrestrial constraints on its age, *Quaternary International*, 45/46, 19–28.

Auriac, A., P.L. Whitehouse, M.J. Bentley, H. Patton, J.M. Lloyd, and A. Hubbard (2016), Glacial isostatic adjustment associated with the Barents sea ice sheet: A modelling intercomparison, *Quaternary Science Reviews*, 147, 122–135.

Austermann, J., J.X. Mitrovica, K. Latychev, and G.A. Milne (2013), Barbados-based estimate of ice volume at last glacial maximum affected by subducted plate, *Nature Geoscience*, 6, 553–557.

Balling, N. (1980), The land uplift in Fennoscandia, gravity field anomalies and isostasy, in *Earth rheology, Isostasy and Eustasy*, ed. Morner, N., 297–321, Wiley, New York.

Balmino, G., K. Lambeck, and W.M. Kaula (1973), A spherical harmonic analysis of the Earth's topography, *Journal of Geophysical Research*, 78(2), 478–481.

Balmino, G. (1994), Gravitational potential harmonics from the shape of a homogeneous body, *Celestial Mechanics and Dynamical Astronomy*, 60, 331–364.

Bassin, C., G. Laske, and G. Masters (2000), The current limits of resolution for surface wave tomography in North America, *EOS Trans AGU*, *81*(F897).

Bell, A.E. (1941), The "Horologium Oscillatorium" of Christian Huygens, *Nature*, 148, 245–248.

Bettadpur, S. (2003), Level-2 gravity field product user handbook, *The GRACE project*, (Jet Propulsion Laboratory).

Bjerhammar, A., S. Stocki, and L. Svensson (1980), A geodetic determination of viscosity, *The Royal Institute of Technology*, Stockholm.

Bock, G. et al. (2001), Seismic probing of Fennoscandian lithosphere, *EOS*, 82(50), 621–636.

Bouman, J., J. Ebbing, M. Fuchs, J. Sebera, V. Lieb, W. Szwillus, R. Haagmans, and P. Novák (2016), Satellite gravity gradient grids for geophysics, *Scientific Reports*, 6(21050), 1–11.

Bowin, C. (2000), Mass Anomalies and the Structure of the Earth, *Physics and Chemistry of the Earth (A)*, 25(4), 343–353.

Bowin, C. (1991), The Earth's gravity field and plate tectonics, *Tectonophysics*, 187, 69–89.

Briggs, R., D. Pollard and L. Tarasov (2014). A data-constrained large ensemble analysis of Antarctica evolution since the Emian *Quaternary Science Reviews*, 103, 91-115.

Brocher, T.M. (2005), Empirical Relations between Elastic Wavespeeds and Density in the Earth's Crust, *Bulletin of the Seismological Society of America*, 95(6), 2081–2092.

Čadek, O., and L. Fleitout (2005), Effect of lateral viscosity variations in the core-mantle boundary region on predictions of the long-wavelength geoid, *Stud. Geophys. Geod.*, 50, 217–232.

Cammarano, F., S. Goes, P. Vacher, and D. Giardini (2003), Inferring upper mantle temperatures from seismic velocities, *Physics of the Earth and Planetary Interiors*, 139, 197–222.

Cammarano, F., P. Tackley, and L. Boschi (2011), Seismic, petrological and geodynamical constraints on thermal and compositional structure of the upper mantle: global thermochemical models, *Geophysical Journal International*, 187, 1301–1318.

Cathles, L.M. (1975), The Viscosity of the Earth's Mantle, *Princeton University Press*, Princeton, NJ.

Chadwick, H. (2013), Chapter 2 - Philoponus The Christian Theologian *Bulletin of the Institute of Classical Studies*, Suppl. no. S103 Vol. 56, Philoponus and the Rejection of Aristotelian Science.

Cheng, M., B.D. Tapley and J.C. Ries (2013), Deceleration in the Earth's oblateness, *Journal of Geophysical Research: Solid Earth*, 118, 740–747.

Christensen, N.I. and W.D. Mooney (1995), Seismic velocity structure and composition of the continental crust: A global view. *Journal of Geophysical Research*, 100, 9761–9788.

Claessens, S.J. and C. Hirt (2013), Ellipsoidal topographic potential: New solutions for spectral forward gravity modeling of topography with respect to a reference ellipsoid, *Journal of Geophysical Research*, 118, 5991–6002.

Clark, J.A., W.E. Farrell, and W.R. Peltier (1978), Global changes in post-glacial sea-level - A numerical calculation, *Quaternary Research*, 9(3), 265–287.

Clark, P. U. and L. Tarasov (2014), Closing the sea level budget at the Last Glacial Maximum, *PNAS Commentary*, 111, 15861–15862.

Cobden, L., I. Mosca, J. Trampert, and J. Ritsema (2012), On the likelihood of post-perovskite near the core-mantle boundary: a statistical interpretation of seismic observations, *Physics of the Earth and Planetary Interiors*, 210-211, 21–35.

Davis, J.L., J.X. Mitrovica, H.-G. Scherneck, and H. Fan (1999), Investigations of Fennoscandian glacial isostatic adjustment using modern sea level records, *Journal of Geophysical Research*, 104(B2), 2733–2747.

Debayle, E. and Y. Ricard (2012), A global shear velocity model of the upper mantle from fundamental and higher Rayleigh mode measurements. *Journal of Geophysical Research*, 117, B10308.

Deschamps, F., R. Snieder, and J. Trampert (2001), The relative density-to-shear velocity scaling in the uppermost mantle, *Physics of the Earth and Planetary Interiors*, 124, 193–211.

Doin, M.-P., L. Fleitout, and D. McKenzie (1996), Geoid anomalies and the structure of continental and oceanic lithosphere, *Journal of Geophysical Research*, 101(B7), 16,119–16,135.

Drinkwater, M.R., R. Floberghagen, R. Haagmans, D. Muzi, and A. Popescu (2003), GOCE: ESA's first Earth Explorer Core mission. In Beutler, G.B., M.R. Drinkwater, R. Rummel, and R. von Steiger (Eds.), *Earth Gravity Field from Space - from Sensors to Earth Sciences*, In the Space Sciences Series of ISSI, Vol. 18, 419–432, Kluwer Academic Publishers, Dordrecht.

Durrheim, R.J. and W.D. Mooney (1994), Evolution of the Precambrian lithosphere: seismological and geochemical constraints, *Journal of Geophysical Research*, 99(B8), 15,359–15,374.

D'Urso, M. G. (2014), Analytical computation of gravity effects for polyhedral bodies, *Journal of Geodesy*, 88(1), 13–29.

Ebbing, J. (2007a), Isostatic density modeling explains the missing root of the Scandes, *Norwegian Journal of Geology*, *87*, 13–20.

Ebbing, J., C. Braitenberg, and S. Wienecke (2007b), Insights into the lithospheric structure and tectonic setting of the Barents Sea region from isostatic considerations, *Geophysical Journal International*, 171, 1390–1403.

Ebbing, J., R. W. England, T. Korja, T. Leuritsen, O. Olesen, W. Straford and C. Weidle (2012), Structure of the Scandes lithosphere from surface to depth, *Tectonophysics*, 536-537, 1–24.

Ebbing, J., J. Bouman, M. Huchs, V. Lieb, R. Haagmans, J.A.C. Meekes, and R.A. Fattah (2013), Advancements in satellite gravity gradient data for crustal studies, *The Leading Edge*, 900–906.

Ebbing, J., J. Bouman, M. Fuchs, S. Gradmann, and R. Haagmans (2014) Sensitivity of GOCE gravity gradients to crustal thickness and density variations: case study for the Northeast Atlantic Region, *Gravity, Geoid, and Height Systems*, U. Martin (Ed.), International Association of Geodesy Symposia, 141.

Eshagh, M. (2009), The effect of polar gabs on the solution of gradiometric boundary value problems, *Artificial Satellites*, 43(3), 97–108.

Farrell, W. E. and Clark, J. A. (1976), Postglacial sea-level, *Geophysical Journal of the Royal Astronomical Society*, 46(3), 647–667.

Fecher, T., R. Pail, and T. Gruber (2015), Global gravity field modeling based on GOCE and complementary gravity data, *International Journal of Applied Earth Observation and Geoinformation*, 35, 120–127.

Flechtner, F., P. Morton, M. Watkins, F. Webb, and U. Marti (2014), Status of the GRACE Follow-On mission, In: Marti U. (eds) *Gravity, Geoid, and Height Systems*, International Association of Geodesy Symposia, 141, 117–121.

Forsberg, R. (1984), A study of terrain reductions, density anomalies and geophysical inversion methods in gravity field modelling, Report 355, 13 pp., Department of Geodetic Science and Surveying, The Ohio State University, Columbus, USA.

Forsberg, R. and S. Kenyon (2004), *Gravity and Geoid in the Arctic Region - The northern polar gab now filled*, 6 pp., Proceedings of the GOCE Workshop, ESA-ESRIN, March 2004.

Forsberg, R., A.V. Olesen, H. Yildiz, and C.C. Tscherning (2011), *Polar gravity fields from GOCE and airborne gravity*, Proceedings of the 4th International GOCE User Workshop, Munich, Germany, ESA SP-696.

Forte, A.M (2007), Constraints on seismic models from other disciplines - Implications for mantle dynamics and composition, in *Treatise of Geophysics*, 1, 805–857, Elsevier.

Forte, A.M and J.X. Mitrovica (2001), Deep-mantle high-viscosity flow and thermochemical structure inferred from seismic and geodynamic data, *Nature*, 410, 1049–1056.

Forte, A.M., W.R. Peltier, A.M. Dziewonski, and R.L. Woodward (1993), Dynamic surface topography: a new interpretation based upon mantle flow models derived from seismic tomography, *Geophysical Research Letters*, 20(3), 226–228.

Forte, A.M., R.L. Woodward, and A.M. Dziewonski (1994), Joint inversion of seismic and geodynamic data for models of three-dimensional mantle heterogeneity, *Journal of Geophysical Research*, 99(B11), 21,857–21,877.

Foulger, G.R., G.F. Panza, I.M. Artemieva, I.D. Bastow, F. Cammarano, J.R. Evans, W.B. Hamilton, B.R. Julian, M. Lustrino, H. Thybo, and T.B. Yanovskaya (2013), Caveats on tomographic images, *Terra Nova*, 0, 1–23.

Fullea, J., M.R. Muller, A.G. Jones, and J.C. Afonso (2014), The lithosphere-asthenosphere system beneath Ireland from integrated geophysical-petrological modeling II: 3D thermal and compositional structure, *Lithos*, *189*, 49–64.

Fullea, J., J. Rodríguez-González, M. Charco, Z. Martinec, A. Negredo, and A. Villaseñor (2015), Perturbing effects of sub-lithospheric mass anomalies in GOCE gravity gradient and other gravity data modelling: Application to the Atlanttic-Mediterranean transition zone, *International Journal of Applied Earth Observation and Geoinformation*, 35, 54–69.

Gardner, G.H.F., L.W. Gardner, and A.R. Gregory (1974), Formation Velocity and Density - The Diagnostic Basics for Stratigraphic Traps, *Geophysics*, 39(6), 770–780.

DeGiorgio, R. (2012), A new 3D velocity model of Scandinavia from seismic data, *Master Thesis*, University of Leicester.

Grad, M., T. Tiira, and Working Group ESC (2009), The Moho depth map of the European plate, *Geophysical Journal International*, 176, 279–292.

Gradmann, S., J. Ebbing, and J. Fullea (2013), Integrated geophysical modelling of a lateral transition zone in the lithospheric mantle under Norway and Sweden, *Geophysical Journal International*, 194, 1358–1373.

Graf, A. (1958), Das Seegravimeter, *Zeitschrift fur Instrumentenkunde*, 60, 151–162.

Graney, C.M. (2012), Anatomy of a fall: Giovanni Battista Riccioli and the story of g, *Physics Today*, 65(9), 36–40.

Greff-Lefftz, M., L. Métivier, and J. Besse (2010), Dynamic mantle density heterogenities and global geodetic observables. *Geophysical Journal International*, 180, 1080–1094.

Griffin, W.L., S.Y. O'Reilly, J.C. Afonso, and G.C. Begg (2009), The composition and evolution of lithospheric mantle: a re-evaluation an its tectonic implications, *Journal of Petrology*, 50(7), 1185–1204.

Grombein, T., X. Luo, K. Seitz, and B. Heck (2014), A wavelet-based assessment of topographic-isostatic reductions for GOCE gravity gradients, *(*Surveys in Geophysics), 35, 959–982.

Grosswald, M.G. (1980), Late Weichselian Ice Sheet of Northern Eurasia, *Quaternary Research*, 13, 1–32.

Grosswald, M. G. (1998), Late-Weichselian ice sheet in Arctic and Pacific Siberia, *Quaternary International*, 45/46, 3–18.

Grosswald, M.G. and T.J. Hughes (2002), The Russian component of an Arctic Ice Sheet during the Last Glacial Maximum, *Quaternary Science Reviews*, 21, 121–146.

Hager, B. H. (1984), Subducted slabs and the geoid: constraints on mantle rheology and flow, *Journal of Geophysical Research*, 89(B7), 6003–6015.

Hager, B.H., R.W. Clayton, M.A. Richards, R.P. Comer, and A.M. Dziewonski (1985), Lower mantle heterogeneity, dynamic topography and the geoid, *Nature*, 313(6003), 541–545.

Hamza, V.M. and F.P. Vieira (2012), Global distribution of the lithosphere-asthenosphere boundary: a new look, *Solid Earth*, 3, 199–212.

Haskell, N.A. (1937), The viscosity of the asthenosphere, *American Journal of Science*, 33(5), 22–28.

Hasterok, D. and D.S. Chapman (2007), Continental thermal isostasy: 1. Methods and sensitivity, *Journal of Geophysical Research*, 112, B06414, 1–15.

Heck, B. and K. Seitz (2007), A comparison of the tesseroid, prism and point-mass approaches for mass reductions in gravity field modelling, *Journal of Geodesy*, 81, 121–136.

Heiskanen, W.A., F.A. Vening Meinesz (1958), *The Earth and its Gravity Field*, McGraw-Hill, New York.

Heiskanen, W.A. and H. Moritz (1984). *Physical Geodesy*, Reprint, Institute of Physical Geodesy, Technical University Graz, Austria.

Herceg, M., I.M. Artemieva, and H. Thybo (2016), Sensitivity analysis of crustal correction for calculation of lithospheric mantle density from gravity data, *Geophysical Journal International*, 204, 687–696.

Hess, H. (1962), History of Oceanic Basins, In A.E.J. Engel, H.L. James, and B.F. Leonard, *Petrologic studies: a volume in honor of A.F. Buddington*, Boulder, CO: Geologic Society of America, 599–620.

Hirose, K., N. Takafuji, N. Sata, and Y. Ohishi (2005), Phase transition and density of subducted MORB crust in the lower mantle, *Earth and Planetary Science Letters*, 237, 239–251.

Hirt, C. and M. Kuhn (2012), Evaluation of high-degree series expansions of the topographic potential to higher-order powers, *Journal of Geophysical Research*, 117, B12407.

Hirt, C. and M. Kuhn (2014), Band-limited topographic mass distribution generates full-spectrum gravity field: Gravity forward modeling in the spectral and spatial domains revisited, *Journal of Geophysical Research Solid Earth*, 119, 3646–3661.

Holzrichter, N. and J. Ebbing (2016), A regional background model for the Arabian Peninsula from modeling satellite gravity gradients and their invariants, *Tectonophysics*, 692, 86–94.

Honkasolo, T. (1964), On the use of gravity measurements for investigation of the land upheaval in Fennoscandia, *Fennia*, 89, 21–23.

Hughes, A.L.C., J. Mangerud, R. Gyllencreutz, J.I. Svendsen, Ø.S. Lohne (2014). Evolution of the Eurasian Ice Sheets during the last deglaciation (25-10 kyr). American Geophysical Union Fall Meeting, San Francisco, 13-19 December.

Hughes, A. L. C., R. Gyllencreutz, Ø.S. Lohne, J. Mangerud, J.I. Svendsen (2016), The last Eurasian ice sheets – a chronological database and time-slice reconstruction, DATED-1, *Boreas*, 45(1), 1–45.

Ivins, E., T.S. James, J. Wahr, E.J.O Schrama, F.W. Landerer, and K.M. Simon (2013), Antarctic contribution to sea level rise observed by GRACE with improved GIA correction, *Journal of Geophysical Research: Solid Earth*, 118, 3126–3141.

Jacob, T., J. Wahr, W.T. Pfeffer, and S. Swenson (2012), Recent contributions of glaciers and ice caps to sea level rise, *Nature*, 482, 514–518.

Jekeli, C. (1981), Alternative methods to smooth the Earth's gravity field, *Rep. 327*, Dep. of Geod. Sci. and Surv., Ohio State Univ., Columbus.

Johnston, P., K. Lambeck (1999), Postglacial rebound and sea level contributions to changes in the geoid and the Earth's rotation axis, *Geophysical Journal International*, 136, 537–558.

Jones, A.G., J.C. Afonso, J. Fullea, and F. Sala-jegheh (2014), The llithosphere-asthenosphere system beneath Ireland from integrated geophysical-petrological modeling I:; Observations, 1D and 2D hypothesis testing and modeling, *Lithos*, 189, 28–48.

Jordan, T.H. (1975), Composition and development of the continental tectosphere, *Nature*, 274, 544–548.

Jordan, T.H. (1978), Lateral heterogeneity and mantle dynamics, *Nature*, 257, 745–750.

Jordan, T.H. (1979), The Deep Structure of the Continents, *Scientific American*, 240(1), 92–107.

Kaban, M.K. (2001), A gravity model of the North Eurasia crust and upper mantle: 1. Mantle and isostatic residual gravity anomalies, *Russian Journal of Earth Sciences*, 3(2), 125–144.

Kaban, M.K. and W.D. Mooney (2001), Density structure of the lithosphere in the southwestern United States and its tectonic significance, *Journal of Geophysical Research*, 106, 721–740.

Kaban, M.K., P. Schwintzer, and S.A. Tikhotsky (1999), A global isostatic gravity model of the Earth, *Geophysical Journal International*, 136, 519–536.

Kaban, M.K., O.G. Flovenz, and G. Palmason (2002), Nature of the crust-mantle transition zone and the thermal state of the upper mantle beneath Iceland from gravity modelling, *Geophysical Journal International*, 149, 281–299.

Kaban, M.K., P. Schwintzer, I.M. Artemieva, and W.D. Mooney (2003), Density of the continental roots: compositional and thermal contributions, *Earth and Planetary Science Letters*, 209, 53–69.

Kaban, M.K., P. Schwintzer, and Ch. Reigber (2004), A new isostatic model of the lithosphere and gravity field, *Journal of Geodesy*, 78, 368–385.

Kaban, M.K., Tesauro, M., and Cloetingh, S. (2010), An integrated gravity model for Europe's crust and upper mantle, *Earth and Planetary Science Letters*, 296, 195–206.

Kaban, M.K., M. Tesauro, W.D. mooney, and S. Cloetingh (2014), Density, temperature, and composition of the North American lithosphere – New insights from a joint analysis of seismic

gravity, and mineral physics data: 1. Density structure of the crust and upper mantle, *Geochemistry, Geophysics, Geosystems*, 15, 4781–4807.

Kaban, M.K., W. Stolk, M. Tesauro, S. El Khrepy, N. Al-Arifi, F. Beekman, and S. A.P.L. Cloetingh (2016), 3D density model of the upper mantle of Asia based on inversion of gravity and seismic tomography data, *Geochemistry, Geophysics, Geosystems*, 17, 1–21.

Kakkuri, J., and Z. Wang (1998), Structural effects of the crust on the geoid modeled using deep seismic sounding interpretations, *Geophysical Journal International*, 135, 495–504.

Karato, S. (2008), *Deformation of Earth Materials: An Introduction to the Rheology of Solid Earth*, 377 pp., Cambridge Univ. Press.

Kaufmann, G. (1997), The onset of Pleistocene glaciation in the Barents Sea: implications for Glacial Isostatic Adjustment, *Geophysical Journal International*, 131, 281–292.

Kaufmann, G. and Wu, P. (1998), Lateral asthenospheric viscosity variations and postglacial rebound: a case study for the Barents Sea, *Geophysical Research Letters*, 25(11), 1963–1966.

Kaufmann, G., P. Wu (2002), Glacial isostatic adjustment in Fennoscandia with a three-dimensional viscosity structure as an inverse problem, *Earth and Planetary Science Letters*, 197, 1–10.

Kaufmann, G., P. Wu, and G. Li (2002), Glacial isostatic adjustment in Fennoscandia for a laterally heterogeneous earth, *Geophysical Journal International*, 143, 262–273.

Kelly, A., R.W. England, and P.K.H. Maguire (2007), A crustal seismic velocity model for the UK, Ireland and surrounding seas, *Geophysical Journal International*, 171, 1172–1184.

Kendall, J.-M. and P.M. Shearer (1994), Lateral variations in D" thickness from long-period shear wave data, *Journal of Geophysical Research*, 99(B6), 11575–11590.

Kendall, R. A., J.X. Mitrovica, and G.A. Milne (2005), On post-glacial sea level – ii. numerical formulation and comparative results on spherically symmetric models, *Geophysical Journal International*, 161(3), 679–706.

Khan, A., S. Koch, T.J. Shankland, A. Zunino, and J.A.D. Connolly (2015), Relationships between seismic wave-speed, density, and electrical conductivity beneath Australia from seismology, mineralogy, and laboratory-based conductivity profiles, *The Earth's Heterogeneous Mantle: Chapter 5*, A. Khan and F. Deschamps (eds.), Springer International Publishing, Switzerland

Kierulf, H. P., H. Steffen, M.J.R. Simpson, M. Lidberg, P. Wu, and H. Wang (2014), A GPS velocity field for Fennoscandia and a consistent comparison to glacial isostatic adjustment models, *Journal of Geophysical Research*, 119(8), 66134–6629.

Kinck, J.J., E.S. Husebye and F.R. Larsson (1993), The Moho depth distribution in Fennoscandia and the regional tectonic evolution from Archean to Permian times, *Precambrian Research*, 64, 23–51.

Klitzke, P., J.I. Faleide, M. Scheck-Wenderoth, and J. Sippel (2015), A lithosphere-scale structural model of the Barents Sea and Kara Sea region, *Solid Earth*, 6, 153–172.

Koninklijk Nederlandsch Geologisch-Mijnbouwkundig Genootschap, Verhandelingen van het (1957), Gedenkboek F.A. Vening Meinesz, *Geologische Serie deel XVIII*, V/H Mouton and Co, 's-Gravenhage.

Korsman, K., T. Korja, M. Pajunen, P. Virransalo, and GGT/SVEKA Working Group (1999), The GGT/SVEKA Transect: Structure and evolution of the continental crust in the Paleoproterozoic Svecofennian Orogen in Finland, *International Geology Review*, 41, 287–333.

Kozlovskaya, E., T. Janik, J. Yliniemi, G. Karatayev and M. Grad (2004), Density-velocity relationship in the upper lithosphere obtained from P- and S-wave velocity models along the EUROBRIDGE-97 seismic profile and gravity data, *Acta Geophysica Polonica*, 52(4), 397–424.

Kuhn, M., W.E. Featherstone, and J.F. Kirby (2009), Complete spherical Bouguer gravity anomalies over Australia, *Australian Journal of Earth Sciences*, 56, 213–223.

Kuskov, O.L., V.A. Kronrod, A.A. Prokofyev, and N.I. Pavlenkova (2014), Thermo-chemical structure of the lithospheric mantle underneath the Siberian craton inferred from long-range seismic profiles, *Tectonophysics*, 615-616, 154–166.

Lachapelle, G. (1976), A Spherical Harmonic Expansion of the Isostatic Reduction Potential, *Bollettino di Geodesia E Scienze Affini*, nr. 3.

Lachenbruch, A.H. and P. Morgan (1990), Continental extension, magmatism and elevation: formal relations and rules of thumb, *Tectonophysics*, 174, 39–62.

Lambeck, K. (1990), Glacial rebound, sea level change and mantle viscosity, *Quarterly Journal R. astr. Soc*, 31, 1–30.

Lambeck, K. (1995), Constraints on the Late Wechselian ice sheet over the Barents Sea from observations of raised shorelines, *Quaternary Science Reviews*, 14, 1–16.

Lambeck, K. (1996), Limits on the areal extent of the Barents Sea ice sheet in late Weichselian time, *Global and Planetary Change*, 12, 41–51.

Lambeck, K., Y. Yokoyama, P. Johnston, and A. Purcell (2000), Global ice volumes at the Last Glacial Maximum and early Lateglacial, *Earth and Planetary Science Letters*, 181, 513–527.

Lambeck, K., A. Purcell, J. Zhao, and N-.O. Svensson (2010), The Scandinavian Ice Sheet: from MIS 4 to the end of the last glacial maximum, *Boreas*, 39, 410–435.

Lambert, A., N. Coutier, and T. James (2006). Long-term monitoring by absolute gravimetry: Tides to postglacial rebound, *Journal of Geodynamics*, 41, 307–317.

Landes, M., J.R.R. Ritter, and P.W. Readman (2007), Proto-Iceland plume caused thinning of Irish lithosphere, *Earth and Planetary Science Letters*, 255, 32–40.

Larsen, E., S. Funder, and J. Thiede (1999), Late Quaternary history of northern Russia and adjacent shelves - a synopsis, *Boreas*, 28, 6–11.

Laske, G., G. Masters, Z. Ma, and M. Pasyanos (2013), Update on CRUST1.0 - A 1-degree Global Model of Earth's Crust, *Geophys. Res. Abstracts*, (15), Abstract submitted to EGU2013-2658.

Lay, T. (1989), Structure of the core-mantle transition zone: a chemical and thermal boundary later, *Eos*, 70(4), 49–59.

Lay, T., Q. Williams, and E.J. Garnero (1998), The core-mantle boundary layer and deep Earth dynamics, *Nature*, 392, 461–468.

Lay, T., J. Hernlund, E.J. Garnero, and M.S. Thorne (2006), A post-perovskite lens and D" heat flux beneath the Central Pacific, *Science*, 314, 1272–1276.

Lekić, V. and B. Romanowicz (2011), Inferring upper-mantle structure by full waveform tomography with the spectral element method, *Geophysical Journal international*, 185, 799–831.

Lidberg, M., J. M. Johansson, H.-G. Scherneck, and J. L. Davis (2007), An improved and extended GPS-derived 3D velocity field of the glacial isostatic adjustment (GIA) in Fennoscandia, *Journal of Geodesy*, 81, 213–230.

Lidberg, M., J. M. Johansson, H.-G. Scherneck, and G. A. Milne (2010), Recent results based on continuous GPS observations of the GIA process in Fennoscandia from BIFROST, *Journal of Geodynamics*, 50, 8–18.

Ludwig, W.J., J.E. Nafe, and C.L. Drake (1970), Seismic refraction, in: *The Sea*, A.E. Maxwell (Editor), Vol. 4, Wiley-Interscience, New York, 53–84.

Lundquist, C.A. and G. Veis (Eds.) (1966), *Geodetic parameters for a 1966 Smithsonian Institution Standard Earth*, vol. 1, Smithsonian Astrophysical Observatory, Cambridge, Mass.

Maguire, P., R. England, and A. Hardwick (2011), LISPB DELTA, a lithospheric seismic profile in Britain: analysis and interpretation of the Wales and southern England section, *Journal of the Geological Society*, 168, 61–82.

Mangerud, J., J.I. Svendsen, and V.I. Astakhov (1999), Age and extend of the Barents and Kara ice sheets in Northern Russia, *Boreas*, 28, 46–80.

Mangerud, J., V.I. Astakhov, and J.I. Svendsen (2002), The extent of the Barents-Kara ice sheet during the last glacial maximum, *Quaternary Science Reviews*, 21, 111–119.

Mao, W.L., H. Mao, W. Sturhahn, J. Zhao, V.B. Prakapenka, Y. Meng, J. Shu, Y. Fei, and R.J. Hemley (2006), Iron-rich post-perovskite and the origin of ultralow-velocity zones, *Science*, 312, 564–565.

Martinec, Z. (1991), On the accuracy of the method of condensation of the Earth's topography, *Manuscripta Geodaetica*, 16, 288–294.

Martinec, Z. (2014), Mass-density Green's functions for the gravitational gradient tensor at different heights, *Geophysical Journal International*, 196, 1455–1465.

Martinec, Z. and J. Fullea (2015), A refined model of sedimentary rock cover in the southeastern part of the Congo basin from GOCE gravity and vertical gravity gradient observations, *International Journal of applied Earth Observation and Geoinformation*, 35, 70–87.

Martinec, Z., K. Pec, and M. Bursa (1989), The Phobos gravitational field modeled on the basis of its topography. *Earth, Moon, and Planets*, 45, 219–235.

Marquart, G. (1989), Isostatic topography and crustal depth corrections for the Fennoscandian geoid, *Tectonophysics*, 169, 67–77.

Mayer-Grr T., A. Eicker, E. Kurtenbach, K.-H. Ilk, F. Flechtner, T. Gruber, A. Gntner, M. Mandea, M. Rothacher, T. Schne and J. Wickert (2010), ITG-GRACE: Global static and temporal gravity field models from GRACE data, *System Earth via Geodetic-Geophysical Space Techniques*, Springer-Verlag, Berlin, Heidelberg, 159–168.

Mayer-Gürr, T., D. Rieser, E. Höck, J. Brockmann, W.-D. Schuh, I. Krasbutter, J. Kusche, A. Maier, S. Krausse, W. Hausleitner, O. Baur, A. Jäggi, U. Meyer, L. Prange, R. Pail, T. Fecher, and T. Gruber (2011), *The new combined satellite only model GOCO03s*, Abstract submitted to GGHS2012, Venice (Poster).

Maupin, V., A. Agostini, I. Artemieva, N. Balling, F. Beekman, J. Ebbing, R.W. England, A. Frassetto, S. Gradmann, B.H. Jacobsen, A. Köhler, T. Kvarven, A.B. Medhus, R. Mjelde, J. Ritter, D. Sokoutis, W. Stratford, H. Thybo, B. Wawerzinek, and C. Weidle (2013), The deep structure of the Scandes and its relation to tectonic history and present-day topography, *Tectonophysics*, 602, 15–37.

McKenzie, D. (2010), The influence of dynamically supported topography on estimates of T_e, *Earth and Planetary Science Letters*, 295, 127–138.

Métivier, L., L. Caron, M., Greff-Lefftz, G. Pajot-Métivier, L. Fleitout, and H. Rouby (2016), Evidence for postglacial signatures in gravity gradients: A clue in lower mantle viscosity, *Earth and Planetary Science Letters*, 452, 146–156.

Milne, G.A., J. L. Davis., J. X. Mitrovica, H.-G. Scherneck, J. M. Johansson, M. Vermeer and H. Koivula (2001), Space-Geodetic Constraints on Glacial Isostatic Adjustment in Fennoscandia, *Science*, 291, 2381.

Mitrovica, J. (1996), Haskell [1935] revisited, *Journal of Geophysical Research*, 101(B1), 555–596.

Mitrovica, J., and W. Peltier (1989), Pleistocene deglaciation and the global gravity field, *Journal of Geophysical Research*, 94(B10), 13,651–13,671.

Mitrovica, J., and W. Peltier (1991), On postglacial geoid subsidence over the equatorial oceans, *Journal of Geophysical Research*, 96(B12), 20,053–20,071.

Moholdt, G., C. Nuth, J.O. Hagen, and J. Kohler (2010), Recent elevation changes of Svalbard glaciers derived from ICESat laser altimetry, *Remote Sensing of Environment*, 114, 2756–2767.

Moholdt, G., B. Wouters, and A.S. Gardner (2012), Recent mass changes of glaciers in the Russian High Arctic, *Geophysical Research Letters*, 39, L10502.

Molinari, I. and A. Morelli (2011), EPcrust: a reference crustal model for the European Plate, *Geophysical Journal International*, 185(1), 352–364.

Mooney, W.D. and J.E. Vidale (2003), Thermal and chemical variations in subcrustal cratonic lithosphere: evidence from crustal isostasy, *Lithos*, 71, 185–193.

Mooney, W.D. and M.K. Kaban (2010), The North American Upper Mantle: Density, Composition, and Evolution, *Journal of Geophysical Research*, 115, B12424.

Mooney, W.D., G. Laske and G. Masters (1998), CRUST 5.1: A global crustal model at 5°x5°, *Journal of Geophysical Research*, 103, 727–747.

Murakami, M., K. Hirose, K. Kwamura, N. Sata, and Y. Ohishi (2004), Post-perovskite phase transition in mgSiO$_3$, *Science*, 304(5672), 855–858.

Nagy, D., G. Papp, and J. Benedek (2000), The gravitational potential and its derivatives for the prism, *Journal of Geodesy*, 74(7), 552–560.

Nakagawa, T. and P.J. Tackley (2005), The interaction between the post-perovskite phase change and a thermo-chemical boundary layer near the core-mantle boundary, *Earth and Planetary Science Letters*, 238, 204–216.

Nataf, H.-C. and Y. Ricard (1996), 3SMAC: an a priori tomographic model of the upper mantle based on geophysical modeling, *Physics of the Earth and Planetary Interiors*, 95, 101–122.

Nerem, R.S., F.J. Lerch, J.A. Marshall, E.C. Pavlis, B.H. Putney, B.D. Tapley, R.J. Eanes, J.C. Ries, B.E. Schutz, C.K. Shum, M.M. Watkins, S.M. Klosko, J.C. Chan, S.B. Luthcke, G.B. Patel, N.K. Pavlis, R.G. Williamson, R.H. Rapp, R. Biancale, and F. Nouel (1994), Gravity model development for TOPEX/POSEIDON: Joint gravity models 1 and 2, *Journal of Geophysical Research*, 99(C12), 24,421–24,447.

NIMA (1997), Department of Defense World Geodetic System 1984, Its Definition and Relationships With Local Geodetic Systems, *NIMA Technical Report TR8350.2*, Third Edition.

Novák, P (2000), Evaluation of gravity data for the Stokes-Helmert solution to the geodetic boundary-value problem, *Technical Report 207*, University of New Brunswick, Fredericton.

Novák, P. and Grafarend, E. (2006), The effect of topographical and atmospheric masses on space borne gravimetric and gradiometric data, *Studia Geophysica et Geodaetica*, 78(11), 691–706.

Nuth, C., G. Moholdt, J. Kohler, J.O. Hagen, and A. Kääb (2010), Svalbard glacier elevation changes and contribution to sea level rise, *Journal of Geophysical Research*, 115, F01008.

Pail, R., H. Goiginger, W.-D. Schuh, E. Höck, J.M. Brockmann, T. Fecher, T. Gruber, T. Mayer-Gürr, J. Kusche, A. Jäggi, and D. Rieser (2010), Combined satellite gravity field model *GOCO01S* derived from GOCE and GRACE, *Geophysical Research Letters*, 37, L020314.

Pail, R., S. Bruinsma, F. Migliaccio, C. Förste, H. Goiginger, W.-D. Schuh, E. Höck, M. Reguzzoni, J.M. Brockmann, O. Abrikosov, M. Veicherts, T. Fecher, R. Mayrhofer, I. Krasbutter, F. Sansó, ad C.C. Tscherning (2011), First GOCE gravity field models deriver by three different approaches, *Journal of Geodesy*, 85, 819–843.

Panet, I., G. Pajot-Métivier, M. Greff-Lefftz, L. Métivier, M. Diament, and M. Mandea (2014), Mapping the mass distribution of Earth's mantle using satellite-derived gravity gradients, *Nature Geoscience*, 7, 131–135.

Panasyuk, S.V. (1998), The effect of compressibility, phase trans- formations, and assumed density structure on mantle viscosity inferred from Earth's gravity field, *PhD Thesis*, MIT.

Panasyuk, S.V. and B.H. Hager (2000), Models of isostatic and dynamic topography, geoid anomalies, and their uncertainties, *Journal of Geophysical Research*, 105(B12), 28,199–28,209.

Paulson, A., S. Zhong, and J. Wahr (2007), Limitations on the inversion for mantle viscosity from postglacial rebound, *Geophysical Journal International*, 168, 1195–1209.

Pavlis, N.K. and R.H. Rapp (1990), The development of an isostatic gravitational model to degree 360 and its use in global gravity modelling, *Geophysical Journal International*, 100, 369–378.

Pavlis, N.K., S.A. Holmes, S.C. Kenyon, and J.K. Factor (2012), The development and evaluation of the Earth Gravitational Model 2009 (EGM2008), *Journal of Geophysical Research*, 117(B4), B04406.

Peltier, W.R. (1974), Impulse response of a Maxwell Earth, *Reviews of Geophysics*, 12(4), 649–669.

Peltier, W. (1996), Mantle viscosity and ice-age ice-sheet topography, *Science*, 273, 1359–1364.

Peltier, W. (2004), Global Glacial Isostasy and the Surface of the Ice-Age Earth: The ICE-5G (VM2) Model and GRACE, *Annual Review of Earth and Planetary Sciences*, 32, 111–149.

Peltier, W.R. (2007), Mantle Dynamics and the D" Layer: Impacts of the PostPerovskite Phase, *Post-Perovskite: The Last Mantle Phase Transition*, Geophysical Monograph Series, 174, 217–227.

Peltier, W and P. Wu (1982), Mantle phase transitions and the free-air gravity anomalies over Fennoscandia and Laurentia, *Geophysical Research Letters*, 9(7), 731–734.

Peltier, W. and R. Fairbanks (2006), Global glacial ice volume and last glacial maximum duration from an extended Barbados sea level record, *Quaternary Science Reviews*, 25, 3322–3337.

Peltier, W.R. and R. Drummond (2008), Rheological stratification of the lithosphere: A direct inference based upon the geodetically observed pattern of the g; axial isostatic adjustment of the North American continent, *Geophysical Research Letters*, 35, L16314.

Peltier, W.R., D.F. Argus, and R. Drummond (2015), Space geodesy constraints ice age terminal deglaciation: The global ICE-6G_C (VM5a) model, *Journal of Geophysical Research: Solid Earth*, 120, 450–487.

Penaud, A., F. Eynaud, J.L. Turon, S. Zaragosi, F. Marret, and J.F. Bourillet (2008), Interglacial variability (MIS 5 and MIS 7) and dinoflagellate cyst assemblages in the Bay of Biscay (North Atlantic), *Marine Micropaleontolgy*, 68, 136–155.

Press, W., S. Teukolsky, W. Vetterling, and B. Flannery (1992), *Numerical recipes in FORTRAN. The art of scientific computing.*, 2nd ed., Cambridge University Press.

Rapp, R.H. (1982), Degree variances of the Earth's potential, topography and its isostatic compensation, *Bulletin Geodesique*, 56, 84–94.

Rapp, R. H., Y. M. Wang, and N. K. Pavlis (1991), The Ohio State 1991 Geopotential and Sea Surface Topography Harmonic Coefficient Models, *Report No.410*, Department of Geodetic Science and Surveying, The Ohio State University, Columbus, Ohio.

Reston, T.J., J. Pennell, A. Stubenrauch, I. Walker, and M. Perez-Gussinye (2001), Detachment faulting, mantle serpentinization, and serpentinite-mud volcanism beneath the Porcupine Basin, Southwest of Ireland, *Geology*, 29(7), 587–590.

Ricard, Y., C. Froidevaux, and L. Fleitout (1988), Global plate motion and the geoid: a physical model, *Geophysical Journal International*, 93(3), 477–484.

Richardson, K.R., J.R. Smallwood, R.S. White, D.B. Snyder, and P.K.H. Maguire (1998), Crustal structure beneath the Faroe Islands and the Faroe-Iceland Ridge, *Tectonophysics*, 300, 159–180.

Ritsema, J., A. Deuss, H.J. van Heijst, and J.H. Woodhouse (2011), S40RTS: a degree-40 shear-velocity model for the mantle from new Rayleigh wave dispersion, teleseismic traveltime

and normal-mode splitting function measurements, *Geophysical Journal International*, 184, 1223–1236.

Riva, R.E.M., B.C. Gunter, T.J. Urban, L.L.A. Vermeersen, R.C. Lindenbergh, M.M. Helsen, J.L. Bamber, R.S.W. van der Wal, M.R. van den Broeke, and B.E. Schutz (2009), Glacial Isostatic Adjustment over Antarctica from combined ICESat and GRACE satellite data, *Earth and Planetary Science Letters*, 288, 516–523.

Rodell, M., P. Houser, U. Jambor, J. Gottschalck, K. Mitchell, C.J. Meng, K. Arsenault, B. Cosgrove, J. Radakovich, M. Bosilovich, J.K. Entin, J.P. Walker, D. Lohmann, and D. Toll (2004), The global land data assimilation system, *Bulletin American Meteorological Society*, 85, 381–394.

Root, B.C., P. Novák, J. Ebbing, W. van der Wal, and L.L.A. Vermeersen (2015), Glacial Isostatic Adjustment in the static gravity field of Fennoscandia, *Journal of Geophysical Research: Solid Earth*, 120, 503–518

Root, B.C., P. Novák, D, Dirkx, M.K. Kaban, W. van der Wal, and L.L.A. Vermeersen (2016), On a spectral method for forward gravity field modelling, *Journal of Geodynamics*, 97, 22–30.

Roy, M., J.K. MacCarthy, and J. Selverstone (2005), Upper mantle structure beneath the eastern Colorado Plateau and Rio Grande rift revealed by Bouguer gravity, seismic velocities, and xenolith data, *Geochemistry, Geophysics, and Geosystems*, 6(10), 1–19.

Rudolph, S., J. Kusche, and K.-H. Ilk (2002), Investigations on the polar gab problem in ESA's gravity field and steady-state ocean circulation explorer mission (GOCE), *Journal of Geodynamics*, 33, 65–74.

Rummel, R., R. H. Rapp, H. Sunkel, and C.C. Tscherning (1988), Comparison of global topographic/isostatic models to the Earth's observed gravity field, *Technical Report Report No. 388*, Department of Geodetic Science and Surveying, The Ohio State University Columbus, Ohio.

Sabadini, R., D.A. Yuen, and E. Boschi (1982), Polar wandering and the forced responses of a rotating, multilayered, viscoelastic planet, *Journal of Geophysical Research*, 87, 2885–2903.

Schaeffer, A. J. and S. Lebedev (2013), Global shear speed structure of the upper mantle and transition zone, *Geophysical Journal International*, 194(1), 417-449.

Schivardi, R. and A. Morelli (2011), EPmantle: a 3-D transversely isotropic model of the upper mantle under the European Plate, *Geophysical Journal International*, 185, 469–484.

Schmidt, P., B. Lund, J-O. Näslund, and J. Fastook (2014), Comparing a thermo-mechanical Weichselian Ice Sheet reconstruction to reconstructions based on the sea level equation: aspects of ice configurations and glacial isostatic adjustment, *Solid Earth*, 5, 371–388.

Schrama, E. J. O., B. Wouters, and R. Rietbroek (2014), A mascon approach to assess ice sheet and glacier mass balances and their uncertainties from GRACE data, *Journal of Geophysical Research: Solid Earth*, 119, 6048–6066.

Shahraki, M., H. Schmeling, M.K. Kaban, and A.G. Petrunin (2015), Effects of the postperovskite phase change on the observed geoid, *Geophysical Research Letters*, 42, 1–9.

Shako, R., C. Förste, O. Abrykosov, S. Bruinsma, J.-C. Marty, J.-M. Lemoine, F. Flechtnner, K.-H. Neumayer, and C. Dahle (2014), EIGEN-6C: A high-resolution global gravity combination model including GOCE data, In: Flechtner, F., Sneeuw, N., Schuh, W.-D. (Eds.), *Observation of the System Earth from Space - CHAMP, GRACE, GOCE and future missions*, (GEOTECHNOLOGIEN Science Report: No. 20; Advanced Technologies in Earth Sciences), Berlin, Springer, 155–161.

Shapiro, S.S., B.H. Hager, and T.H. Jordan (1999), The continental tectosphere and Earth's long-wavelength gravity field, *Lithos*, 48, 135–152.

Simmons, N.A., A.M. Forte, L. Boschi, and S.P. Grand (2010), GyPSuM: A joint tomographic model of mantle density and seismic wave speeds, *Journal of Geophysical Research*, *115*, B12310.

Sjöberg, L., H. Fan, and T. Nord (1994), Further studies on the Fennoscandian gravity field versus the Moho depth and land uplift, *Bulletin Geodesique*, 69, 32–42.

Sjöberg, L. E., and M. Bagherbandi (2013), A study on the Fennoscandian post-glacial rebound as observed by present-day uplift rates and gravity field model GOCO02S, *Acta Geod Geophys*, 48, 317–331.

Schmitt, C. (2013), Chapter 12 - Philoponus commentary on Aristotle's Physics in the Sixteenth century, *Bulletin of the Institute of Classical Studies*, Suppl. no. S103 Vol. 56, Philoponus and the Rejection of Aristotelian Science.

Sclater, J.G. and J. Francheteau (1970), The implications of terrestrial heat flow observations on current tectonic and geochemical models of the crust and upper mantle of the Earth, *Geophysical Journal of the Royal Astronomical Society*, 20, 509–542.

Shurbet, G.L. and J.L. Worzei (1956), Gravity observations at sea in USS Diablo, *Bulletin Géodésique*, 42(1), 51–60.

Simons, M. and B.H. Hager (1997), Localization of the gravity field and the signature of glacial rebound, *Nature*, 390, 500–504.

Sneeuw, N. (1994), Global spherical harmonic analysis by least-squares and numerical quadrature methods in historical perspective, *Geophysical Journal International*, 118, 707–716.

Sobel, D. (2011), A More Perfect Heaven: How Copernicus Revolutionised the Cosmos, *Bloomsbury Publishing*, 50 Bedford Square, London.

Spasojevic, S., M. Gurnis, and R. Sutherland (2010), Mantle upwellings above slab graveyards linked to the global geoid lows, *Nature Geoscience*, 3, 435–438.

Steffen, H., and G. Kaufmann (2005), Glacial isostatic adjustment of Scandinavia and northwestern Europe and the radial viscosity structure of the Earth's mantle, *Geophysical Journal International*, 163, 801–812.

Steffen, H., and P. Wu (2011), Glacial isostatic adjustment in Fennoscandia - a review of data and modeling, *Journal of Geodynamics*, 52, 169–204.

Steffen, H., H. Denker, and J. Muller (2008), Glacial isostatic adjustment in Fennoscandia from GRACE data and comparison with geodynamical models, *Journal of Geodynamics*, 46, 155–164.

Steffen, H., P. Wu and H. Wang (2010), Determination of the Earth's structure in Fennoscandia from GRACE and implications for the optimal post-processing of GRACE data, *Geophysical Journal International*, 182, 1295–1310.

Steffen, H., G. Kaufmann, and R. Lampe (2014), Lithosphere and upper-mantle structure of the southern Baltic Sea estimated from modelling relative sea-level data with glacial isostatic adjustment, *Solid Earth*, 5, 447–459.

Steinberger, B. (2016), Topography caused by mantle density variations: observations-based estimates and models derived from tomography and lithosphere thickness, *Geophysical Journal International*, 205, 604–621.

Strakhov, V.N., T.V. Romaniuk, and N.K. Frolova (1989). Method of direct gravity problem solution for modeling of global and regional gravity anomalies (in Russian), In: Strakhov, V. (Ed.) *New Methods of the Gravity and Magnetic Anomaly Interpretation*, Inst. Whys. of the Earth, Moscow, 118–235.

Stratford, W., H. Thybo, J.I. Faleide, O. Olesen, and A. Tryggvason (2009), New Moho Map for onshore southern Norway, *Geophysical Journal International*, 178(3), 1755–1765.

Svendsen, J.L. et al. (1999), Maximum extend of the Eurasian ice sheets in the Barents and Kara Sea region during the Weichselian, *Boreas*, 28, 234–242.

Svendsen, et al.(2004a), Late quaternary ice sheet history of northern Eurasia, *Quaternary Science Reviews*, 23(11–13), 1229–1271.

Svendsen, J. I., V. Gataullin, J. Mangerud, and L. Polyak (2004b), The glacial history of the Barents and Kara sea region, in *Quaternary Glaciations: Extent and Chronology*, Part 1: Europe, Dev. Quat. Sci., vol. 2, edited by J. Ehlers and P. Gibbard, 369–378, Elsevier, Amsterdam.

Talwani, M. (1962), Gravity measurements on HMS Acheron in South Atlantic and Indian Ocean, *Geological Society of American Bulletin*, 73, 1171–1182.

Tamisiea, M., J.X. Mitrovica, and J. Davis (2007), GRACE gravity data constrain ancient ice geometries and continental dynamics over Laurentia, *Science*, 316, 881–883.

Trampert, J. and R.D. van der Hilst (2005), Towards a quantitative interpretation of global seismic tomography, *In: Earth's Deep Interior: Structure, Composition, and Evolution*, van der Hilst, R.D., Bass, J.D., Matas, J., and Trampert, J. (Eds.), Geophysical Monograph 160, 47–62.

Tapley, B.D., S. Bettadpur, M. Watkins, and C. Reigber (2004), The gravity recovery and climate experiment: Mission overview and early results, *Geophysical Research Letters*, 31(9), L09607.

Tarasov, L., A.S. Dyke, M.N. Radford, and W.R. Peltier (2012), A data-calibrated distribution of deglacial chronologies for the North American ice complex from glaciological modeling, *Earth and Planetary Science Letters*, 315-316, 30–40.

Tesauro, M., M.K. Kaban, and S.A.P.L. Cloetingh (2008), EuCRUST-07: A new reference model for the European crust, *Geophysical Research Letters*, 35, L05313.

Tesauro, M., M.K. Kaban, and S.A.P.L Cloetingh (2009), A new thermal and rheological model of the European lithosphere, *Tectonophysics*, 476, 478–495.

Tesauro, M., M.K. Kaban, W.D. Mooney, and S. Cloetingh (2014), NACr14: A 3D model for the crustal structure of the North American Continent, *Tectonophysics*, 631, 65–856.

Torge, W. (1989), *Gravimetry*, Book , Berlin New York, Walter de Gruyter, ISBN 2-11-010702-3.

Tosi, N., O. Čadek, Z. Martinec, D.A. Yuen, and G. Kaufmann (2009), Is the long-wavelength geoid sensitive to the presence of postperovskite above the core-mantle boundary?, *Geophysical Research Letters*, 36, L05303.

Tosi, N. (2007), Numerical modeling of present-day mantle convection, Ph.D. thesis, Charles University, Prague, Czech Republic.

Tromp, J., and J.X. Mitrovica (1999), Surface loading of a viscoelastic earth - I. General theory, *Geophysical Journal International*, 137(3), 847–855.

Tscherning, C.C., R. Forsberg, A. Albertella, F. Migliaccio, and F. Sansó (2000), The polar gab problem: space-wise approaches to gravity field determination in polar areas, In: Sünkel, H. (Ed.), From Eötvös to mGal, Final Report, ESA-ESTEC.

Turcotte, D.L. and G. Schubert (1982), Geodynamics, 450 pp., *John Wiley*, New York.

Turcotte, D.L., and G. Schubert (2014), *Geodynamics*, Cambridge University Press, Cambridge, UK.

Tushingham, A., and W. Peltier (1992), Validation of the ICE-3G Model of Würm-Wisconsin deglaciation using a global data base of relative sea level histories, *Journal of Geophysical Research*, 97(B3), 3285–3304.

Uieda, L., V.C. Oliveira Jr, and V.C.F. Barbosa (2013), Modeling the Earth with Fatiando a Terra, *Proceedings of the 12th Python in Science Conference*, pp. 91 - 98.

van der Wal, W., P. Wu, M.G. Sideris, and C.K. Shum (2008), Use of GRACE determined secular gravity rates for glacial isostatic adjustment studies in North-America, *Journal of Geodynamics*, 46(3-5), 144–154.

van der Wal, W., A. Braun, P. Wu, and M. G. Sideris (2009), Prediction of decadal slope changes in Canada by glacial isostatic adjustment modelling, *Canadian Journal Earth Sciences*, 46, 587–595.

van der Wal, P. Wu, H. Wang, and M. G. Sideris (2010), Sea levels and uplift rate from composite rheology in glacial isostatic adjustment modeling, *Journal of Geodynamics*, 50, 38–48.

van der Wal, W., E. Kurtenbach, J. Kusche, and B. Vermeersen (2011), Radial and tangential gravity rates from GRACE in areas of glacial isostatic adjustment, *Geophysical Journal International*, 187, 797–812.

van der Wal, W., A. Branhoorn, P. Stocchi, S. Gradmann, P. Wu, M. Drury and B. Vermeersen (2013), Glacial isostatic adjustment model with composite 3-D Earth rheology for Fennoscandia, *Geophysical Journal International*, 194, 61–77.

Vaníček, P., M. Najafi, Z. Martinec, L. Harrie, and L. E. Sjöberg (1995), Higher-degree reference field in the generalized Stokes-Helmert scheme for geoid computation, *Journal of Geodesy*, 70(1), 176–182.

van Hengel, T.J.C. (2014), The Diving Dutchman: het marien-gravimetrisch onderzoek van F.A. Vening Meinesz (1887-1966), PhD Thesis, *University of Leiden*, Leiden.

Vening Meinesz F.A. (1929), Theory and practise of pendulum observations at sea, *publication of the Dutch Geodetic Commitee*, Drukkerij Waltman, Delft.

Vening Meinesz F.A. (1931), Une nouvelle mthode pour la rduction isostatique rgionale de lintensit de la pesanteur, *Bulletin Géodésique*, 29, 33–51 (in French).

Vening Meinesz, F. A. (1937), The determination of the earth's plasticity from post- glacial uplift of Scandinavia: Isostatic adjustment, *Proceedings of the Koninklijke Nederlandse Akademie van Wetenschappen*, 40, 654–662.

Vening Meinesz F.A. (1932-1948), Gravity expeditions at sea between 1923-1938 Vol I-IV, *Drukkerij Waltman*, Delft.

Vening Meinesz F.A. (1948-1958), Gravity expeditions 1948-1958 Vol V, ed. G.J. Bruins, *W.D. Meinema*, Delft.

Vermeersen, L., and R. Sabadini (1997), A new class of stratified viscoelastic models by analytical techniques, *Geophysical Journal International*, 129, 531–570.

Vieira, F.P. and V.M. Hamza (2010), Global Heat Loss: New Estimates Using Digital Geophysical Maps and GIS Techniques., Proceedings of the IV Symposium of the Brazilian Geophysical Society, 14-17 November, 1-6.

Voltaire (1733), The works of Voltaire, Vol. XIX (*Philosophical Letters*), *On Chanchellor Bacon*, Translator William F. Fleming, New York: E.R. DuMont, 1901.

Wang, H., P. Wu, and W. van der Wal (2008), Using postglacial sea level, crustal velocities and gravity-rate-of-change to constrain the influence of thermal effects on mantle lateral heterogeneity, *Journal of Geodynamics*, 46, 104–117.

Wahr, J., M. Molenaar, and F. Bryan (1998), Time variability of the Earth's gravity field: Hydrological and oceanic effects and their possible detection using GRACE, *Journal of Geophysical Research: Solid Earth*, 103(B12), 30205–30229.

Wahr, J., S. Swenson, V. Zlotnicki, and I. Velicogna (2004), Time-variable gravity from GRACE: First results, *Geophysical Research Letters*, 31, L11501.

Watts, A. B. (2001), *Isostasy and Flexure of the Lithosphere*, Cambridge University Press.

Werner, R.A. and D.J. Scheeres (1996), Exterior gravitation of a polyhedron derived and compared with harmonic and mascon gravitation representations of asteroid 4769 Castalia, *Celestial Mechanics and Dynamical Astronomy*, 65, 313–344.

Whitehouse, P. (2009), Glacial isostatic adjustment and sea-level change, Technical Report TR-09-11, Swedish Nuclear Fuel and Waste Management Co., Box 250, SE-101 24 Stockholm.

Whitehouse, P. L., M.J.Bentley, and A.M.L. Brocq (2012), A deglacial model for Antarctica: geological constraints and glaciological modelling as a basis for a new model of Antarctic glacial isostatic adjustment, *Quaternary Science Reviews*, 32, 1–24.

Wolf, D. (1984), The relaxation of spherical and flat Maxwell Earth models and effects due to the presence of the lithosphere, *Journal of Geophysics*, 56(1), 24–33.

Worzel, J.L. and M. Ewing (1950), Gravity measurements at sea, 1947, *EOS*, 31(6), 917–923.

Wu, P. (1978) The response of a Maxwell Earth to applied surface mass loads: Glacial isostatic adjustment. MSc Thesis. University of Toronto, Toronto.

Wu, P. and W.R. Peltier (1982), Viscous gravitational relaxation, *Geophysical Journal of the Royal Astronomical Society*, 70, 435–486.

Wu, P., and W.R. Peltier (1983), Glacial isostatic adjustment and the free air gravity anomaly as a constraint on deep mantle viscosity, *Geophys. J. R. astr. Soc.*, 74, 377–449.

Yegorova, T. P. and V.I. Starostenko (1999), Large-scale three-dimensional gravity analysis of the lithosphere below the transition zone from Western Europe to the East European Platform, *Tectonophysics*, 314, 83–100.

Yokoyama, Y., K. Lambeck, P. de Deckker, P. Johnston, and L.K. Fifield (2000), Timing of the Last Glacial Maximum from observed sea-level minima, *Nature*, 406, 713–716.

Zeeberg, J., D.J. Lubinski, and S.L. Forman (2000), Holocene relative sea-level history of Novaya Zemlya, Russia, and implications for Late-Weichselian ice-sheet loading, *Quaternary Research*, 56(2), 28–230.

Zoback, M.L. and W.D. Mooney (2003), Lithospheric Buoyancy and Continental Intraplate Stresses, *International Geology Review*, 45, 95–118.

Curriculum Vitae

Bart Root was born in Goes, the Netherlands on the 21st of November 1985. He attended secondary school at the *Erasmus College* in Zoetermeer with courses on science and technology. He graduated in 2004 and went on a sabbatical year traveling Australia. Afterwards, in 2005 he enlisted to the *Delft University of Technology* at the faculty of Aerospace Engineering, where he obtained his BSc. degree in 2010 and followed by his MSc. degree in 2012. His MSc. thesis was entitled *Validating and improving the orbit determination of Cryosat-2*. During his MSc. studies, he worked at EADS Astrium in Friedrichshafen, Germany for 5 months, where he was involved in the simulator and post-processing software of ESA's SWARM mission.

For his PhD research in 2012, he joined the Astrodynamics and Space Missions group at the Aerospace Engineering faculty, working on a NWO-funded research proposal entitled: *Lithospheric and Upper Mantle Structures in Northwestern Europe derived by Satellite Gravimetry*. The main goal of this project was to combine gravimetric data with seismic observations in GIA-related modelling studies. This work is described by the dissertation. During the PhD research period, he had close cooperation with researchers from NGU and later University of Kiel, enabling him to make several work visits. The research resulted in a software package that is able to model global density structures and perform spectral analysis to the gravity solutions. For the TU Delft, he has also developed a satellite tracking station called DopTrack, that produces range-rate observables using the principle of Doppler. The ground station is now being used in the curriculum of the BSc. and MSc. of the faculty of Aerospace Engineering. Also, he has worked on a technological and historical heritage project envisioned by the TU Delft Library as project scientist, describing the work of prof. Vening Meinesz onboard the submarine K-XVIII.

List of Publications

Peer-reviewed publications

- Root, B.C., van der Wal, W., Novák, P., Ebbing, J., and Vermeersen, L.L.A. (2014), Glacial Isostatic Adjustment in the Static Gravity Field of Fennoscandia, *Journal of Geophysical Research: Solid Earth*, 120 (1), 503-518.

- Root, B.C., Tarasov, L., and van der Wal, W. (2015), GRACE constrained Weichselian ice models in the Barents Sea, *Geophysical Research Letters*, 42 (9), 3313-3320.

- Root, B.C., Novák, P., Dirkx, D., Kaban, M., van der Wal, W., and Vermeersen, L.L.A. (2016), On a spectral method for forward gravity field modelling, *Journal of Geodynamics*, 97, 22-30.

- Root, B.C., van der Wal, W., Ebbing, J., England, R.W., and Vermeersen, L.L.A (2017), Comparing gravity-based to tomography-derived lithosphere densities: a case study of the British Isles and surrounding areas, *Geophysical Journal International*, 208(3), 1796–1810.

Submitted manuscripts

- Dirkx, D., E. Mooij, and B.C. Root (under review), Propagation and estimation of the dynamical behaviour of gravitationally interacting rigid bodies, *Celestial Mechanics and Dynamical Astronomy*.

Non peer-review publications

- Root, B.C., R. Vlijm, and S. Fauconnier (2014), Expeditie Wikipedia: Professor Vening Meinesz, *Dutch Foundation for Academic Heritag*, project website: http://www.expeditiewikipedia.nl/#vening-meinesz.

- Root, B.C. (2015), Teaching Hands-On Satellite Tracking and Communication to Delft University of Technology Undergraduates, *Mathworks: Technical Articles and Newsletters*, published by Mathworks.

- Root, B.C. (2017), Het Gouden Kalf: het zwaartekrachtsinstrument van professor Vening Meinesz, Hoofdstuk in *175 jaar TU Delft: Erfgoed in 33 verhalen*, Ed. van Woerkom, Histechnica.